Universidade de Aveiro Departamento de Física
2019

Susana Cristina Ribeiro Novais

Sensores de fibra ótica para meios desafiantes

Optical fiber sensors for challenging media

Universidade de Aveiro Departamento de Física
2019

Susana Cristina Ribeiro Novais

Sensores de fibra ótica para meios desafiantes

Optical fiber sensors for challenging media

Tese apresentada à Universidade de Aveiro para cumprimento dos requisitos necessários à obtenção do grau de Doutor em Engenharia Física, sob a orientação científica do Professor Doutor João de Lemos Pinto (Professor Catedrático do Departamento de Física da Universidade de Aveiro), e da Doutora Marta Sofia dos Anjos Ferreira (Investigadora de Pós-Doutoramento do I3N e do Departamento de Física da Universidade de Aveiro).

This work was funded by the Project Pest-C/CTM/LA 25/2013: "I3N", by FEDER funds through the COMPETE 2020 Programme and National Funds through FCT, for research grants BI/UI96/6643/2013 and BI/UI96/6643/2016.

It was also funded by the European Project SIRBATT: Stable Interfaces for Rechargeable Batteries (FP7-ENERGY-2013, grant agreement No. 608502) and by the Project POCI-01-0145-FEDER-016414 PAC: FIBR3D, cofinanced by POCI and Programa Operacional Regional de Lisboa, through the COMPETE 2020 Programme and National Funds through FCT, for the research fellowships BI/UI96/6643/2014 and BI/UI96/6643/2018, respectively.

Ao Nuno

Aos meus pais e irmãos

“A satisfação reside no esforço, não apenas no resultado obtido.
O esforço total é a plena vitória.” (Mahatma Gandhi)

o júri

presidente

Prof. Doutor Aníbal Guimarães da Costa
professor catedrático da Universidade de Aveiro

Prof. Doutor Orlando José dos Reis Frazão
professor auxiliar convidado da Universidade do Porto- Faculdade de Ciências

Prof. Doutor Manuel Filipe Pereira da Cunha Martins Costa
professor auxiliar da Universidade do Minho

Prof. Doutor José Carlos Antunes Marques
professor associado da Universidade da Madeira

Prof. Doutora Margarida Maria Resende Vieira Facão
professora auxiliar da Universidade de Aveiro

Prof. Doutor João de Lemos Pinto
professor catedrático da Universidade de Aveiro

agradecimentos

Como autora deste trabalho, sinto que este não é apenas meu, mas de todos aqueles que me ajudaram e apoiaram neste percurso. Começo por agradecer aos meus orientadores.

Ao Professor João Lemos Pinto pela oportunidade de poder realizar este trabalho, incentivando-me sempre a dar o meu melhor. À Doutora Marta Ferreira, um especial agradecimento pela inspiração, por teres sido um pilar neste percurso académico e por me abrires portas a tantos caminhos novos. A tua ajuda, o teu conhecimento e discernimento foram decisivos para o desenvolvimento deste trabalho. Obrigada pelo apoio, pelos ensinamentos e também pelo carinho.

Ao Instituto de Nanoestruturas, Nanomodelação e Nanofabricação, Departamento de Física e Instituto de Telecomunicações pelas condições de acolhimento proporcionadas no desenvolvimento do trabalho apresentado nesta Tese.

À equipa de investigação do Instituto Helmholtz de Ulm, na Alemanha e da Empresa Jonhson Mattey Battery Systems, na Escócia, quero expressar o meu agradecimento pela forma como fui recebida, e pelo apoio prestado durante o período de testes experimentais.

Aos meus colegas e amigos do Departamento de Física, Micael, Tiago, Cátia e Luís pelo apoio, pelas conversas diárias e pela constante boa disposição.

A todos aqueles que de alguma forma se foram cruzando comigo no laboratório, no dia-a-dia e de alguma forma tornaram os meus dias mais alegres.

Um especial agradecimento ao Paulo Antunes, à Cátia Leitão, à Nélia Alberto, à Fátima Domingues e à Catarina Ferreira pela presente atenção, apoio, disponibilidade e carinho.

A todos os meus amigos que sempre me apoiaram nas horas mais complicadas, que sempre acreditaram em mim e que contribuíram para o meu crescimento pessoal, particularmente ao Mário, à Cata e ao Jorge.

Um agradecimento especial e de coração aos meus pais e irmãos, pelos valores que sempre incutiram ao longo da vida, pelo apoio diário, paciência e amor incondicional. Sem vocês, teria sido mais difícil.

Por último, mas de todo menos importante, ao Nuno, meu amigo, marido e companheiro de uma vida, muito obrigada, pelo apoio, paciência, por estares lá, nem que fosse apenas em silêncio, pelo positivismo que transmitiste e pela serenidade que me proporcionaste durante a execução deste trabalho.

O meu sincero obrigado a todos vocês.

palavras-chave

Sensores de fibra ótica, Fabry-Perot, interferometria, pós-processamento, ataque químico, baterias de lítio, sensores químicos, funcionalização.

resumo

Com o presente trabalho pretendeu-se explorar soluções de sensores em fibra ótica para a aplicação em meios desafiantes. Novas estruturas sensoras baseadas em pós-processamento de fibra ótica foram abordadas, tendo em consideração a sua sensibilidade a variações do meio externo.

Numa primeira etapa, foram embebidas redes de Bragg no interior de baterias de lítio, para monitorizar variações de temperatura *in situ* e *operando*. Devido ao complexo meio químico da bateria, os sensores em fibra ótica revelaram ser uma alternativa mais vantajosa em relação aos sensores elétricos, não só pela sensibilidade e rápida resposta, mas também pelo fato de não afetarem o desempenho da bateria. Além disso, os sensores usados revelaram ser pouco invasivos e quimicamente estáveis.

Ainda no âmbito deste tema, e com o objetivo de monitorizar possíveis deformações e variações de pressão no interior da bateria de lítio, foram desenvolvidos novos sensores baseados em cavidades de Fabry-Perot do tipo *in-line*. Esses sensores foram caraterizados em pressão lateral, deformação e temperatura.

Numa fase posterior, o estudo centrou-se no desenvolvimento de configurações que permitissem a obtenção de sensores com elevada resolução e/ou sensibilidade. Uma das configurações consistiu na formação de uma microesfera oca na ponta de uma fibra ótica. Esse sensor foi utilizado para detetar variações de concentração e índice de refração de misturas de glicerina e água. A influência do tamanho do diafragma na resposta do sensor também foi estudada, assim como a resposta em temperatura.

Em seguida, desenvolveram-se novos sensores baseados em interferência multimodo, utilizando para tal uma ponta de fibra de sílica sem núcleo. Numa primeira abordagem analisou-se a influência de diferentes parâmetros, como o comprimento e o diâmetro dos sensores. Os sensores foram expostos a diferentes soluções de glucose e água. Verificou-se que o diâmetro do sensor é um fator decisivo para a obtenção de dispositivos mais sensíveis ao índice de refração e, consequentemente, à concentração.

Foi também desenvolvido um sensor baseado em interferência multimodo que permitiu determinar o coeficiente termo-ótico de misturas de etanol e água.

Por fim, procedeu-se à funcionalização de um sensor baseado em interferência multimodo através da deposição de agarose ao longo da estrutura, permitindo assim otimizar a sua resposta a variações do meio externo.

keywords

Optical fiber sensors, Fabry-Perot, interferometry, post-processing, etching, lithium batteries, chemical sensors, functionalization.

abstract

With the present work, the development of fiber optic sensor solutions for the application in challenging media was intended. New sensor structures based on the post-processing of optical fibers were addressed, taking into account their sensitivity to variations in the external environment.

In a first stage, fiber Bragg gratings were embedded in lithium batteries, to monitor temperature *in situ* and *operando*. Due to the harsh chemical environment of the battery, fiber optic sensors revealed to be the most advantageous alternative, when comparing to the electronic sensors. Fiber sensors exhibited good sensitivities and fast responses, besides being less invasive, thus they did not compromise the battery response. Furthermore, they were chemically stable.

Still in the framework of this theme, and with the objective of monitoring possible strain and pressure variations inside the batteries, new sensors based on in-line Fabry-Perot cavities have been proposed. These sensors were characterized in lateral load, strain, and temperature.

In a later stage, the study focused on the development of configurations that allowed to obtain high-resolution and/or sensitivity sensors. One of such configurations was obtained by creating a hollow microsphere at the fiber tip. The sensor was used to detected concentration variations and refractive index of glycerin and water mixtures. The influence of the diaphragm size in the sensor response was also studied, as well as the temperature response.

New sensors based on multimode interference have also been characterized, using a coreless silica fiber tip. First, the influence of different parameters, such as length and diameters were analyzed. The sensors were tested in different solutions of glucose and water. It was observed that the sensor diameter is a decisive factor in obtaining devices that are more sensitive to refractive index and, consequently, to concentration.

The determination of the thermo-optic coefficient of water/ethanol mixtures was also addressed using a multimode fiber interferometer sensor.

Finally, a multimode interferometer sensor was functionalized by depositing agarose throughout the structure, allowing to optimize the response of the sensors to the external environment.

ACRONYMS

CC	Constant Current
CCCV	Constant Current Constant Voltage
CSF	Coreless Silica Fiber
DAQ	Data Acquisition System
EC	External Center
FBG	Fiber Bragg Grating
FP	Fabry-Perot
FSR	Free Spectral Range
GIF	Graded Index Fiber
HC PCF	Hollow Core Photonic Crystal Fiber
HF	Hydrofluoric Acid
IC	Internal Center
LFP	Lithium Iron Phosphate
MMF	Multimode Fiber
MMI	Multimode Interference
OCV	Open Circuit Voltage
OSA	Optical Spectrum Analyzer
PE	Polyethylene
RH	Relative Humidity
RI	Refractive Index
RIU	Refractive Index Units
SMF	Single Mode Fiber
SMS	Single-Mode-Multimode-Single-Mode

TC	Thermocouples
TFBG	Tilted Fiber Bragg Grating
TOC	Thermo-Optic Coefficient

TABLE OF CONTENTS

LIST OF FIGURES

LIST OF TABLES

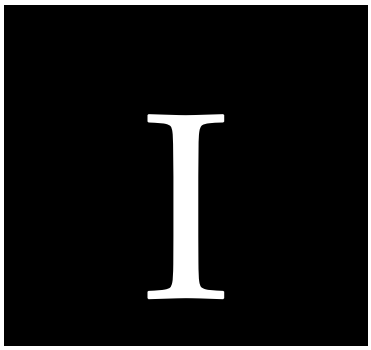

Introduction

1. Optical fiber sensors – a brief overview

The request for detection of environmental changes, through physical, chemical or biological parameters, has grown rapidly over the last decades. There is a great interest, not only in the scientific community, but also in industry, to develop new sensing devices based on optical fibers, to exploit their intrinsic characteristics, and to find new application fields. In order to compete with conventional sensors, these sensors need to be trustworthy, robust, highly sensitive, and economical.

In response to the increasing need to create non-destructive techniques that can monitor specific parameters in harsh environments, or in areas of difficult access, various techniques are being developed, and some of the most promising are based on the use of optical fiber sensors. The ability to have small devices in direct physical contact with the *challenging media* to be sensed brings new opportunities to observe and act on the world, for example, in chemical, biological or pharmaceutical applications, both in lab scale and in industry.

There are several advantages of using optical fiber sensors, such as, small dimensions, capability of multiplexing, possibility for simultaneously measurement of different parameters with a single fiber, chemical inertness, and immunity to electromagnetic fields. Furthermore, this kind of sensors usually presents good linearity, rapid response for real time monitoring, high sensitivity to external perturbations, and ability to be embedded into materials [1]. Due to all these characteristics, optical fiber sensors present several features that make them extremely attractive to be used in a wide variety of applications, namely in the medical, aerospace, and wind energy industries. They have also been applied in the oil and gas industry, taking advantage of distributed sensing capability, and in several fields such electrical engineering, materials science, biology, chemistry, physics, and optics [2]. There is no doubt that depending on the application, the parameter or the configuration for which the sensors are developed, the possibilities are extremely vast [3, 4]. Currently, the fiber sensing field is immense, and there is a wide variety of methods for classifying the sensors, according to:

- **The application:** temperature, strain, displacement, current, magnetic fields, pressure, torsion, bending, vibration, humidity, lateral load, refractive index, detection of bio-molecules or chemical species [2];
- **The measurable spatial scope**: point sensors, quasi-distributed sensors, and fully distributed sensors [4];
- **The modulation process:** intensity, phase, state of polarization, and wavelength (frequency) [2];
- **The working principle**: optical fiber gratings (fiber Bragg grating (FBG), chirped fiber Bragg grating, tilted fiber Bragg grating (TFBG) and long period grating), interferometry (Fabry-Perot (FP), Mach-Zehnder, Michelson, Sagnac, high birefringence fiber loop mirror sensors, and multimode interferometer) [5-8], distributed sensors (Raman scattering, Rayleigh scattering and Brillouin scattering) [6], or polarization-optical time domain reflectometry sensors [9, 10].

Given the variety of technologies available today, only those related and used in the context of this Thesis will be addressed in the following Sections.

1.1. Fiber Bragg gratings

In 1978, the physicist Kenneth O. Hill reported the first work on FBGs and their applications both in optical communications and optical sensor systems [11]. Since then, this type of sensors has been widely applied in the measurement of different parameters, such as physical, chemical, biomedical and electrical ones. They are simple, intrinsic sensing elements, which can be photo-inscribed into silica fiber and they have all the advantages associated with fiber optic sensors. Typically, a FBG sensor can be seen as a selective photo-induced modulation of the optical fiber core refractive index. The FBG resonant wavelength (Bragg wavelength), λ_B, is related to the effective refractive index of the core mode (n_{eff}) and to the grating period (Λ), according to Eq. 1 [12]:

$$\lambda_B = 2n_{eff}\Lambda \,, \tag{1}$$

When the grating is illuminated with a broadband optical source, the reflected spectrum presents a sharp peak, which is caused by the interference of light reflected on the planes of the grating. Any perturbation on the grating (e.g., external strain or temperature variation) results in a shift in the Bragg wavelength, which can be detected either in the reflected or in the transmitted spectra [4].

As already mentioned, optical fiber sensors can be easily embedded in different materials. One of the works reported in this Thesis consists on the integration of FBGs in lithium-ion pouch cells to monitor temperature *in-situ* and *operando*. Temperature is one of the parameters with higher impact on the performance, safety, and cycle lifetime of lithium-ion batteries. The operating temperature of batteries must be well controlled, due to the high local current densities that can result in a massive heat release, decomposition of the electrolyte, gas evolution or even explosion of the battery cell. However, the corrosive chemical environment in the batteries is a challenge to monitor internal variations of this measurand [13-16]. The insertion of FBGs has proven to be a good method for measurement due to the aforementioned advantages [17]. It is important to note that when fiber sensors are embedded, their sensitivities to temperature and strain change due to the mechanical stresses produced by the surrounding material, so a new internal calibration is always required [18]. Over the last four years, most of the works reported in the literature were focused on monitoring external temperature using thermocouples attached to the surface of batteries, in strategic locations [19-25] or internally, however, not in direct contact with the chemical medium [26-29]. Recent works proposed the use of FBG sensors to perform this kind of measurements in different types of batteries and considering different locations [17, 30-35].

1.2. Fabry-Perot interferometer sensors

Interferometric optical fiber sensors are based on the principle of optical interference for the measurement of chemical or physical properties. These sensors can be a great solution for sensing because they can exhibit great sensitivity, a wide dynamic range, multiplexing capacity and low losses [36].

One of the first works reporting a fiber optic sensor based on FP interferometry was published in 1982, by Yoshino *et al.* [37]. Since then, a great and rapid evolution occurred in this field. The FP interferometers are normally constituted by two parallel reflecting surfaces, with reflectance R_1 and R_2, separated by a determined distance, L, as exemplified in Figure I.1 [38]. The FP interferometer can be developed by intentionally building up reflectors externally to the fibers (Figure I.1 a), or internally (Figure I.1 b), being classified into two categories: extrinsic and intrinsic sensors [39, 40].

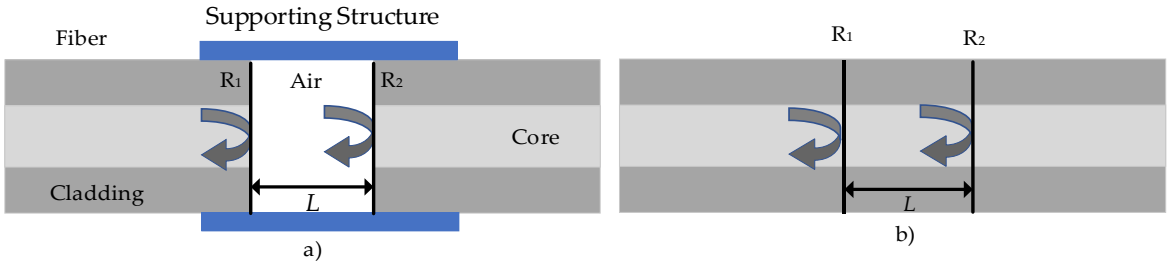

Figure I.1. a) Extrinsic and b) intrinsic FP interferometer sensor, with reflectance R_1 and R_2, separated by a determined distance (L) (adapted from [38]).

In the case of extrinsic sensors, the air cavity can be formed through a supporting structure, such as the one shown in Figure I.1a). These sensors are advantageous for obtaining high finesse interference signals [41], bearing in mind that high reflecting mirrors may be used and yet the manufacturing process is simple and no expensive equipment is needed. However, they have reduced coupling efficiency and careful and precise alignment is required [42].

The intrinsic FP interferometer fiber sensor has reflecting components within the fiber itself. There are several ways to form this type of sensors, such as micro machining [43-46], by using two FBGs in series [47, 48], through chemical etching [49, 50], by thin film deposition [51, 52], by using special fibers [53] or even creating an air bubble in fibers [54]. In the simplest form, when the cavity has low-reflectivity mirrors, it can be approximated to a two-wave interferometer. In such case, the reflection spectrum is essentially determined by the phase difference, δ_{FP}, between the waves generated in the two reflections [55], which is described by:

$$\delta_{FP} = \frac{4\pi n_{eff} L_{FP}}{\lambda} \quad (2)$$

where n_{eff}, L_{FP} and the λ are the effective refractive index of cavity material, the physical length of the cavity and the wavelength of incident light, respectively. When there is an external perturbation, such as variation of strain, temperature or other parameter detectable by the sensors, both the cavity length and effective refractive index can change, translating into a shift of the phase difference. This shift can be easily monitored, by using a suitable interrogation system [38, 55]. Table I.1 presents the main characteristics of the different intrinsic FP sensors reported in the literature in the period between 2014 and 2018.

Table I.1. Different configurations of the intrinsic FP sensors reported from 2014 to 2018.

Year	Configuration	Length (μm)	Measurand	Range	Sensitivity	Ref
2014	Air cavity between 2 single mode fibers (SMFs)	46	Strain Temperature	0 - 1100 με 100 - 600 °C	6.0 pm/με 1.1 pm/°C	[56]
2014	Air bubble and liquid in hollow core fiber, with taper plug	31	Temperature	25 - 39 °C	-6.71 nm/°C	[57]
2014	SMF + etched P-doped fiber + coreless multimode fiber (MMF) and focused ion beam post-processing	172	Temperature	100 - 300 °C	11.5 pm/K	[58]
2014	SMF + microfiber + SMF	21	Strain	0.05 - 0.35 N	~200 pm/ με	[59]
2014	Silica & spheroidal cavities, both formed in a hollow annular core fiber	392	Strain Temperature	0 - 1500 με 23 - 500 °C	1.1 pm/με 13 pm/°C	[60]
2015	SMF + dual hollow core fibers	33.84	Temperature in liquids	20 - 60 °C	-0.4810 nm/°C	[61]
2015	Polymer capped on the end face of SMF	35.1	Pressure Temperature	0 - 2.8 MPa 40 - 90 °C	1.13 nm/MPa 0.249 nm/°C	[62]
2015	Rectangular air	~61	Strain	0 - 500 με	43 pm/με	[63]

	bubble between SMFs		Temperature	25 - 100 °C	2.0 pm/°C	
2015	SMF + silicon pillar	200	Temperature	20 - 100 °C	84.6 pm/°C	[64]
2015	MMF + Pyrex glass + silicon diaphragm	~32	Temperature	-50 - 100 °C	6.07 nm/°C	[65]
2016	Air bubbles with capillary fiber between 2 SMFs	~25-200	Strain Temperature	0 - 1200 με 50 - 400 °C	max: 9.5 pm/με 0.8 pm/°C	[66]
2016	SMF + 2 capillary tubes with different inner diameters	~75-308	RI	1.00054 - 1.00217 RIU	1127.5 nm/RIU	[67]
2016	SMF + hollow-core photonic crystal	75	Temperature	17 - 900 °C	0.94 pm/°C	[53]
2016	SMF + hollow-core photonic crystal fiber	94	Temperature	20 - 90 °C	9.17 pm/°C	[68]
2017	SMF+ MMF (GIF 625)	161	Strain	0 - 1000 με	9.12 pm/με	[69]
2017	FP between a FBG and the fiber end-face		RI	1.3380 - 1.4765 RIU	-1.94 RIU^{-1}	[70]
2017	Etched MMF filled with UV adhesive	37.7	Temperature RI	55 - 85°C 1.332 - 1.372 RIU	213 pm/°C -73.54 nm/RIU	[71]
2017	SMF+ MMF (GIF 625)	161	Lateral load	0 - 4N	2.11 nm/N	[72]
2018	Tapered fiber tip into the capillary + SMF	100	Strain	0 - 2000 με	2.1 pm/με	[73]
2018	SMF + Hollow core tube + SMF	~100	Temperature Strain	50 - 450 °C 0 - 1000 με	0.902 pm/°C 2.97 pm/με	[74]
2018	Fiber core near the end of a standard SMF	60	Temperature	500 - 1000 °C	18.6 pm/°C	[75]
2018	Air bubble tip SMF+ MMF (GIF 625)	29	RI	1.3154 - 1.4571 RIU	-5.49 nm/RIU	[76]
2018	SMF +capillary + nafion film	200	Temperature	-30 - 85 °C	2.71 nm/°C	[77]

1.3. Multimode fiber interferometer sensors

A scheme of a typical multimode fiber interferometer (MMI) sensor is presented in Figure I.2, where a section of mutimode fiber (MMF) is sandwiched between two single-mode fibers (SMFs) [78]. This is the so-called single-mode-multimode-single mode (SMS) fiber structure; however, MMIs can also be obtained using a single-mode-multimode fiber configuration. It has a series of advantages that allows it to be used as sensor, such as simple structure, low cost, small size, and high stability. Some of the parameters that have been monitored with this kind of sensors are strain and temperature [79], displacement [80], refractive index [81], and microbend [82].

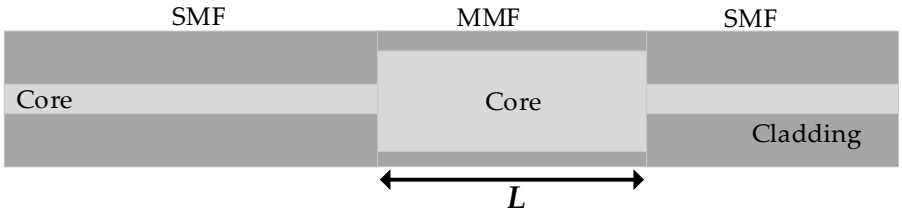

Figure I.2. Schematic configuration of the single-mode-multimode-single-mode fiber structure (adapted from [78]).

The subjacent operating principle of this kind of sensors is the interference of the excited modes in the MMF section, which can be influenced by external perturbations [83, 84], i.e, the fundamental mode that propagates along the SMF will couple into the MMF, exciting many modes, each of which has a different propagation constant [4]. After passing through the MMF section, they reconnect to the SMF. Since each mode has already experienced a different phase shift, the modes interfere.

The main configurations of the MMI structures are simple and enable the detection of a change in the refractive index of the surrounding medium, due to the high interaction of the evanescent field with the external environment. The manufacture of new concepts of MMIs can be greatly enhanced through the combination of fiber optics with the nano-structure technology and the use of sensitive thin films [85]. The sensors based on MMI, allied with the functionalization with thin films as sensitive elements, could open new fields for optical fiber sensor applications. Functional materials can be deposited on the

side- or end-face of fiber with different techniques, such as, spin-coating, dip-coating, thermal evaporation or sputtering [86]. The use of polymeric sensitive materials in optical fiber sensors has the advantage of enhancing the response time with a better sensitivity and selectivity [4, 87]. Table I.2 collects the main configurations and parameters reported over the last 4 years using MMI sensors.

Table I.2. Multimode interference sensors reported in the literature since 2014 until 2018.

Year	Configuration	Length (mm)	Measurand	Range	Sensitivity	Ref
2014	SMF + MMF (40 μm core diameter) + SMF	27	RI	1.3300 - 1.3775 RIU	286.2 nm/RIU	[88]
2014	SMF + offset SMF+ MMF + offset SMF	25	Temperature Liquid- level	25 - 60 °C 10 - 20 mm	0.0815 nm/°C 0.29 nm/mm	[89]
2014	SMF + MMF (40 μm core diameter) + SMF	30	Temperature	25 - 80 °C	358 pm/°C	[90]
2014	SMF + offset MMF + SMF	1	Temperature	39.8 - 83.0 °C	-64.889 nm/RIU	[91]
2015	SMF + MMF + no core fiber + SMF	58.3	RI Strain	1.3370 - 1.3645 RIU 0 - 1600 με	131.71 nm/RIU -1.21 pm/με	[92]
2015	SMF + no core fiber (diameter of 96 μm) + SMF	34.43	Temperature	-30 - 100 °C	38.7 pm/°C	[93]
2015	SMF + offset SMF + SMF	46	Temperature	30 - 270 °C	0.0449 nm/°C	[94]
2015	SMF + no core fiber + SMF	40	Temperature	10 - 100 °C	5.15 nm/°C	[95]
2016	SMF + 4.5 μm offset coreless fiber + SMF	6.3	Liquid- level	21 - 33 mm	681 pm/mm/ RIU	[96]
2016	SMF + coreless fiber (25 mm) + SMF + coreless fiber (30 mm) + SMF	25	RI	1.3288 - 1.3666 RIU	148.60 nm/RIU	[97]

2016	SMF + no core fiber (diameter of 125 μm) + SMF	15	Liquid - level	0 - 500 mm	108.8 pm/mm	[98]
2016	SMF + MMF (core of 105 μm) + SMF	80	Compressive strain	42 - 44 kN	-1411.2 nm/(mm/mm)	[99]
2017	SMF + MMF (core of 105 μm) + SMF	44	Strain Temperature	0 - 1200 με 15 - 75 °C	42.5 pm/με 29.33 pm/°C	[100]
2017	SMF + tapered multicore fiber + SMF	170	RI	1.345 - 1.377	171 nm/RIU	[101]
2018	SMF + MMF (core of 105 μm) + SMF	68	Compressive strain	0 - 31 kN	0.014 nm/kN	[102]
2018	SMF + no core fiber (with alcohol solution within a silica capillary tube) + SMF	40	Temperature	20 - 45 °C	0.49 dB/°C	[103]
2018	SMF + triple cladding quartz specialty fiber + SMF	35	RI	1.3466 - 1.3350 RIU	543.7527 nm/RIU	[104]
2018	SMF + Coreless (diameters between 65.15 - 27.73 μm) + SMF	60	pH	4 - 6	15 nm/pH	[105]
2018	SMF + etched coreless (diameters between 24-125 μm)	24	RI	1.364 - 1.397 RIU	1467.59 nm/RIU	[106]
2018	SMF + coreless (diameter 125 μm)	~30	Relative humidity	20.0 - 98.5%	44.2 pm/%RH	[107]
2018	SMF + etched coreless (diameter 24.4 μm)	5.1	RI	1.315 - 1.365 RIU	627.9 nm/RIU	[108]

2. Motivation and objectives

The motivation for the work developed in the framework of the PhD programme relied on the development and characterization of optical fiber sensors for application in challenging media. Optical sensors offer a versatile solution for detection purposes due to the wide range of independent parameters that can be accessed. Through the interaction between the light and the surrounding liquid medium, it is possible to infer the variation of certain parameters, and the feasibility of performing accurate and non-invasive measurements makes the development of new sensing techniques one of the great motivations of this work.

New sensing structures based on the post processing of optical fibers were developed and as the research progressed and different challenges and obstacles emerged, there was an increase in the motivation to learn new concepts and provide solutions to those obstacles. In addition, there was also the desire to contribute with new approaches to configurations and studies of physical and chemical parameters, and therefore, to contribute to the development of the optical fiber sensing field.

The main objectives were based on:

- the study of integration and monitorization of optical fiber sensors in Li-ion batteries;
- the manufacturing and characterization of interferometric structures based on microspheres for high sensitivity lateral load and strain measurements;
- the development of optical fiber Fabry-Perot tip sensor for detection of water-glycerine mixtures;
- the improvement of an optical fiber sensor tip based in multimode interference and the respective characterization;
- the study and determination of the thermo-optic coefficient of ethanol-water mixtures;

- the post-processing of optical fibers through the deposition of materials through the technique of dip-coating, thus obtaining the functionalization of the fiber and allowing the detection of relative humidity.

3. Thesis organization

This document is divided in eight Chapters describing the process of development and characterization of the fiber optic solutions developed for application in challenging media, accordingly to the proposed PhD work plan.

Chapter I describes an overview of the concepts and sensing elements explored in this Thesis. It also contains the main scientific contributions, finalizing the list of works published during the PhD.

Chapter II proposes the integration of fiber Bragg grating sensors in lithium-ion cells for *in-situ* and *operando* temperature monitoring. This Chapter intends to contribute for the detection of a temperature gradient in real time inside a cell, which can determine possible damage in the battery performance when it operates under normal and abnormal operating conditions, as well as to demonstrate the technical feasibility of the integration of fiber sensors inside Li-ion pouch cells.

Chapter III presents a Fabry-Perot air bubble microcavity fabricated between a section of SMF and a MMF using a fusion splicer. The study of the microcavities growth with the number of applied arcs is performed. The sensors are used for the measurement of lateral load and temperature. Further information about the sensors response to strain in also given.

In Chapter IV, a fiber sensor based on a Fabry-Perot cavity is reported for measuring mixtures of water and glycerin. The sensor is fabricated by producing an air bubble near the end face of a multimode fiber section and reshaping the tip in order to produce a thin silica diaphragm.

Chapter V is dedicated to the measurement of refractive index variations in glucose aqueous solutions. The sensor is fabricated by splicing a short section of coreless silica fiber to standard single mode fiber and influence of the coreless fiber dimensions on the sensor performance is analysed. In this Chapter, the conversion of the refractive index values for water-glucose mixtures to the 1550 nm using a fiber sensor was done for the first time, to the best of our knowledge.

In Chapter VI, the thermo-optic coefficient of ethanol-water mixtures, through refractive index and temperature measurements, is determined using an etched optical fiber tip based on a multimode interferometer. The proposed probe is fabricated by fusion-splicing a 5.2 mm long coreless fiber section to single mode fiber. To reduce the sensor dimensions and improve its sensitivity towards external medium variations, the fiber tip is subjected to wet chemical etching using a solution of 40% hydrofluoric acid.

The Chapter VII is dedicated to the measurement of relative humidity. The sensor is based on a structure with multimode interference and a hydrophilic agarose gel is coated on the sensor, using the dip coating technique. The proposed sensor has a great potential in real time relative humidity monitoring, exhibiting a large range of operation with good stability, and can be of interest for applications where a control of high levels of relative humidity is required.

The Chapter VIII presents some lines summarizing the main results achieved during the PhD and describes the opportunities of future work that this investigation has created.

4. Main contributions and publications

From the works presented in this Thesis, it is my opinion that three of them stand out as main contributions to the field. Due the corrosive chemical environment in the batteries, it is a challenge to monitor internal parameters in real time. However, an accurate monitoring can prevent possible damage in the battery, and the proposed sensors can have a large impact in this field. The second most relevant work was the one based on manufacturing and characterization of interferometric structures based on tip

microspheres. The third was the determination of thermo-optic coefficient of ethanol-water mixtures with optical fiber tip sensor. To my knowledge, this was the first time that this coefficient was determined for solutions with different concentrations of ethanol in water using a fiber sensor.

From the activity developed in the framework of this PhD, a total of 6 articles were published as first author in scientific journals. Besides, still within the scope of this Thesis, one Book Chapter was also published and one paper was published as co-author. A total of 8 communications in international conferences were published, being 4 of them oral presentations. The list of published works is presented below.

Book Chapter

Susana Novais, Micael Nascimento, Marta S. Ferreira, M. Fátima Domingues, Stephan Koch, Gang Yang, Stefano Passerini and João L. Pinto, *Lithium batteries monitoring with fiber Bragg gratings*, Advances in Sensors: Reviews' Book Series, Vol. 5, 2018.

Papers in International Journals

Susana Novais, Marta. S. Ferreira and João L. Pinto, *Relative humidity fiber sensor based on multimode interferometer coated with agarose-gel*, Coatings, Vol. 8, no. 453, 2018.

Susana Novais, Catarina I. A. Ferreira, Marta S. Ferreira and João L. Pinto, *Optical fiber tip sensor for the measurement of glucose aqueous solutions*, Photonics Journal, Vol. 10, no. 5, 2018.

Susana Novais, Marta S. Ferreira and João L. Pinto, *Determination of thermo-optic coefficient of ethanol-water mixtures with optical fiber tip sensor*, Optical Fiber Technology, Vol. 45, pp. 276-279, 2018.

Susana Novais, Marta S. Ferreira and João L. Pinto, *Optical fiber Fabry Perot tip sensor for detection of water-glycerin mixtures*, Journal of Lightwave Technology, Vol. 36, no. 9, pp. 1576-1582, 2018.

Micael Nascimento, Susana Novais, Markus S. Ding, Marta S. Ferreira, Stephan Koch, Stefano Passerini, João L. Pinto, *Internal strain and temperature discrimination with optical fiber hybrid sensors in Li-ion batteries*, Journal Power Sources, Vol. 410-411, pp. 1-9, 2019.

Susana Novais, Marta S. Ferreira and João L. Pinto, *Lateral load sensing with an optical fiber inline microcavity*, Photonics Technology Letters, Vol. 29, no. 17, pp. 1502-1505, 2017.

Susana Novais, Micael Nascimento, Lorenzo Grande, M. Fátima Domingues, Paulo Antunes, Nélia Alberto, Cátia Leitão, Ricardo Oliveira, Stephan Koch, Guk Tae Kim, Stefano Passerini and João Pinto, *Internal and external temperature monitoring of a Li-ion battery with fiber Bragg grating sensors*, Sensors, Vol. 16, no.1394, pp. 1-9, 2016.

Communications in International Conferences

Susana Novais, Catarina I. A. Ferreira, Marta S. Ferreira, João L. Pinto, *Glucose Measurements with Optical Fiber Sensor based on Coreless Silica Fiber*, 26th International Conference on Optical Fibre Sensors, OFS-26, 24-28 September, Lausanne, Switzerland, 2018.

Marta S. Ferreira, Susana Novais, Catarina I. A. Ferreira, João L. Pinto, *Optical fiber tip sensor for determining the thermo-optic coefficient of ethanol-water mixtures,* 26th International Conference on Optical Fibre Sensors, OFS-26, 24-28 September, Lausanne, Switzerland, 2018.

Susana Novais, Marta S. Ferreira, João L. Pinto, *Fabry-Perot cavity based on air bubble in multimode fiber for sensing applications,* Proc. SPIE 10680, Optical Sensing and Detection V, 106801C, SPIE Photonics Europe, 9 May, Strasbourg, France, 2018.

Cátia J. Leitão, M. Fátima Domingues, Susana Novais, Cátia Tavares, João L. Pinto, Paulo André, Carlos Marques, Paulo Antunes, *Arterial pulses assessed with FBG based films: a smart skin approach*, Proc. SPIE 10685, Biophotonics: Photonic Solutions for Better Health Care VI; 106852S, SPIE Photonics Europe, 17 May, Strasbourg, France, 2018.

Susana Novais, Marta S. Ferreira and João L. Pinto, *Fabry-Perot cavity based on air bubble for high sensitivity lateral load and strain measurements*, III International Conference on Applications of Optics and Photonics, 104532V, 22 August, Faro, Portugal, 2017.

Susana Novais, Micael Nascimento, Marta S. Ferreira, Lorenzo Grande, Stephan L. Koch, M. Ding, Stefano Passerini, Vallentina Gentilic, John Forgie, João L. Pinto, *Bragg sensors operating within Li-ion pouch cells*, SIRBATT Workshop "Controlling Lithium Battery Interfaces" in Orlando, Florida, USA, May, 2016.

Micael Nascimento, Susana Novais, Cátia Leitão, M. Fátima Domingues, Nélia Alberto, Paulo Antunes, João L. Pinto, *Lithium batteries temperature and strain fiber monitoring*, Proc. SPIE 9634, 24th International Conference on Optical Fibre Sensors, vol. 96347, 28 September, Curitiba, pp. 9634V-1-9634V-4, 2015.

Susana Novais, *Cell diagnosis and prognosis of lithium ion batteries through optical fiber sensors*, SIRBATT Workshop "Understanding Lithium Battery Interfaces" in Bilbao, Spain, September, 2015.

References

1. A. Othonos, K. Kalli, *Fiber Bragg gratings: Fundamentals and applications in telecommunications and sensing*, Artech House: New York, NY, USA, 1999.

2. K. Fidanboylu, H. S. Efendioglu, *Fiber opic sensors and their applications*, 5th International Advanced Technologies Symposium, Karabuk , 2009.

3. A. D. Kersey, *A review of recent developments in fiber optic sensor Technology*. Optical Fiber Technology, Vol. 2, pp. 291-317, 1996.

4. H. E. Joe, H. Yun, S. H. Jo, M. B. G. Jun, B. K. Min, *Review on optical fiber sensors for environmental monitoring*, International Journal of Precision Engineering and Manufacturing-Green Technology, Vol. 5, pp. 173-191, 2018.

5. C. E. Lee, H. F. Taylor, A. M. Markus, E. Udd, *Optical-fiber Fabry-Perot embedded sensor*. Optics Letters, Vol. 14, pp. 1225-1227, 1989.

6. D. S. Raffaella, *Fibre optic sensors for structural health monitoring of aircraft composite structures: recent advances and applications*, Sensors, Vol. 15, pp. 18666-18713, 2015.

7. O. Frazão, J. M. Baptista, J. L. Santos, *Recent advances in high-birefringence fiber loop mirror sensors*, Sensors, Vol. 7, pp. 2970-2983, 2007.

8. B. Dong, L. Wei, D. P. Zhou, *Miniature high-sensitivity high-temperature fiber sensor with a dispersion compensation fiber-based interferometer*. Applied Optics, Vol. 48, pp. 6466-6469, 2009.

9. J. C. Juarez, H. F. Taylor, *Polarization discrimination in a phase-sensitive optical time-domain reflectometer intrusion-sensor system*, Optics Letters, Vol. 30, pp. 3284-3286, 2005.

10. J. C. Juarez, H. F. Taylor, *Field test of a distributed fiber-optic intrusion sensor system for long perimeters,* Applied Optics, Vol. 46, pp. 1968-1971, 2007.

11. K. O. Hill, Y. Fuji, D. C Johnson, B. S. Kawasaki. *Photosensitivity in optical fiber waveguides: Application to reflection filter fabrication*. Applied Physics Letters, Vol. 32, pp. 647-649, 1978.

12. Y. J. Rao, *In-fiber Bragg grating sensors*, Measurement Science and Technology, Vol. 8, pp. 355-375, 1997.

13. S. Abada, G. Marlair, A. Lecocq, M. Petit, V. Sauvant-Moynot, F. Huet, *Safety focused modeling of lithium-ion batteries: A review,* Journal of Power Sources, Vol. 306, pp. 178-192, 2016.

14. S. J. Harris, A. Timmons, W. J. Pitz, *A combustion chemistry analysis of carbonate solvents used in Li-ion batteries,* Journal of Power Sources, Vol. 193, pp. 855-858, 2009.

15. A. A. Pesaran, *Battery thermal management in EVs and HEVs: issues and solutions*, in Advanced Automotive Battery Conference, Las Vegas, NV, 2001.

16. L. Fan, J. M. Khodadadi, A. A. Pesaran, *A parametric study on thermal management of an air-cooled lithium-ion battery module for plug-in hybrid electric vehicles*, Journal of Power Sources, Vol. 238, pp. 301-312, 2013.

17. L. W. Sommer, A. Raghavan, P. Kiesel, B. Saha, T. Staudt, A. Lochbaum, A. Ganguli, C. J. Bae, M. Alamgir, *Embedded fiber optic sensing for accurate state estimation in advanced battery management systems*, Symposium Q-Materials, Technologies and Sensor Concepts for Advanced Battery Management Systems, Vol. 1681, 2014.

18. A. K. Singh, S. Berggren, Y. Zhu, M. Han, H. Huang, *Simultaneous strain and temperature measurement using a single fiber Bragg grating embedded in a composite laminate*, Smart Mater. Struc. Vol. 26, pp. 1-9, 2017.

19. S. Panchal, M. Mathew, I. Dincer, M. A. Chaab, M. Fowler, *Thermal modeling and validation of temperature distributions in a prismatic lithium-ion battery at different discharge rates and varying boundary conditions*, Applied Thermal Engineering, Vol. 96, pp. 190-199, 2016.

20. S. Panchal, I. Dincer, M. A. Chaab, R. Fraser, M. Fowler, *Experimental temperature distributions in a prismatic lithium-ion battery at varying conditions*, International Communications in Heat and Mass Transfer, Vol. 7, pp. 35-43, 2016.

21. M. Yildiz, H. Karakoc, I. Dincer, *Modeling and validation of temperature changes in a pouch lithium-ion battery at various discharge rates,* International Communications in Heat and Mass Transfer, Vol. 75, pp. 311-314, 2016.

22. S. Panchal, I. Dincer, M. A. Chaab, M. Fowler, R. Fraser, *Uneven temperature and voltage distributions due to rapid discharge rates and different boundary conditions for series-connect $LiFePO_4$ batteries*, International Communications in Heat and Mass Transfer, Vol. 81, pp. 210-217, 2017.

23. J. Jiang, H. Ruan, B. Sun, L. Wang, W. Gao, W. Zhang, *A low-temperature internal heating strategy without lifetime reduction for large-size automotive lithium-ion battery pack*, Applied Energy Vol. 230, pp. 257- 266, 2018.

24. D. Ren, X. Liu, X. Feng, L. Lu, M. Ouyang, J. Lia, X. He, *Model-based thermal runaway prediction of lithium-ion batteries from kinetics analysis of cell components*, Applied Energy, Vol. 228, pp. 633-644, 2018.

25. S. Zheng, L. Wang, X. Feng, X. He, *Probing the heat sources during thermal runaway process by thermal analysis of different battery chemistries*, Journal of Power Sources, Vol. 378, pp. 527-536, 2018.

26. T. Wang, K. J. Tseng, J. Zhao, Z. Wei, *Thermal investigation of lithium-ion battery module with different cell arrangement structures and force air-cooling strategies*, Applied Energy, Vol. 134, pp. 229-238, 2014.

27. M. S. K. Mutyala, J. Zhao, J. Li, H. Pan, C. Yuan, X. Li, *In-situ temperature measurement in lithium ion battery by transferable flexible thin film thermocouples*, Journal of Power Sources, Vol. 260, pp. 43-49, 2014.

28. J. Sun, G. Wei, L. Pei, R. Lu, K. Song, C. Wu, C. Zhu, *Online internal temperature estimation for lithium-ion batteries based on Kalman filter*, Energies, Vol. 8, pp. 4400-4415, 2015.

29. D. J. Noelle, M. Wang, A. V. Le, Y. Shi, Yu Qiao, *Internal resistance and polarization dynamics of lithium-ion batteries upon internal shorting*, Applied Energy, Vol. 212, pp. 796-808, 2018.

30. L. W. Sommer, P. Kiesel, A. Ganguli, A. Lochbaum, B. Saha, J. Schwartz, C. J. Bae, M. Alamgir, A. Raghavan, *Fast and slow ion diffusion processes in lithium ion pouch cells during cycling observed with fiber optic strain sensors*, Journal of Power Sources, Vol. 296, pp. 46-52, 2015.

31. S. Novais, M. Nascimento, L. Grande, M. F. Domingues, P. Antunes, N. Alberto, C. Leitão, R. Oliveira, S. Koch, G. T. Kim, S. Passerini, J. Pinto, *Internal and external temperature monitoring of a Li-ion battery with fiber Bragg grating sensors*, Sensors Vol. 16, pp. 1-9, 2016.

32. A. Raghavan, P. Kiesel, L. W. Sommer, J. Schwartz, A. Lochbaum, A. Hegyi, A. Schuh, K. Arakak, B. Saha, A. Ganguli, K. H. Kim, C. Kim , H. J. Hah, S. Kim, G. Hwang, G. C. Chung, B. Choi, M. Alamgir, *Embedded fiber-optic sensing for accurate internal monitoring of cell state in advanced battery management systems. Part 1: Cell embedding method and performance*, Journal of Power Sources, Vol. 341, pp. 466-473, 2016.

33. A. Ganguli, B. Saha, A. Raghavan, P. Kiesel, K. Arakaki, A. Schuh, J. Schwartz, A. Hegyi, L. W. Sommer, A. Lochbaum, S. Sahu, M. Alamgir, *Embedded fiber-optic sensing for accurate internal monitoring of cell state in advanced battery management systems. Part 2: Internal cell signals and utility for state estimation*, Journal of Power Sources, Vol. 341, pp. 474-482, 2016.

34. M. Nascimento, M. S. Ferreira, J. L. Pinto, *Simultaneous sensing of temperature and bi-directional strain in a prismatic Li-ion battery*, Batteries, Vol. 4, pp. 1-9, 2018.

35. M. Nascimento, M. S. Ferreira, J. L. Pinto, *Real time thermal monitoring of lithium batteries with fiber sensors and thermocouples: a comparative study*, Measurement, Vol. 11, pp. 260-263, 2017.

36. C. E. Lee, H. F. Taylor, *Sensors for smart structures based upon the Fabry-Perot interferometer*. In Fiber Optic Smart Structures, pp. 249-269, New York, 1995.

37. T. Yoshino, K. Kurosawa, K. Itoh, T. Ose, *Fiber-optic Fabry-Perot interferometer and its sensor applications*, IEEE Trans. Microwave Theory Technology, Vol. 30, pp. 1612-1621, 1982.

38. B. H. Lee, Y. H. Kim, K. S. Park, J. B. Eom, M. J. Kim, B. S. Rho, H. Y. Choi, *Interferometric fiber optic sensors*, Sensors, Vol. 12, pp. 2467-2486, 2012.

39. W. H Tsai, C. J. Lin, *A novel structure for the intrinsic Fabry-Perot fiber-optic temperature sensor*, Journal of Lightwave Technology, Vol. 19, pp. 682-686, 2001.

40. S. H. Kim, J. J. Lee, D. C. Lee, I. B. Kwon, *A study on the development of transmission-type extrinsic Fabry-Perot interferometric optical fiber sensor*. Journal of Lightwave Technology, Vol. 17, pp. 1869-1874, 1999.

41. Y. J. Rao, *Recent progress in fiber-optic extrinsic Fabry Perot interferometric sensors*, Optical Fiber Technology Vol. 12, pp. 227-237, 2006.

42. D. Hunger, T. Steinmetz, Y. Colombe, C. Deutsch, T. W. Hansch, J. Reichel, *A fiber Fabry-Perot cavity with high finesse,* New Journal of Physics, Vol. 12, pp. 1-24, 2010.

43. J. Ran, Y. Rao, J. Zhang, Z. Liu, B. Xu, *A miniature fiber-optic refractive-index sensor based on laser-machined Fabry-Perot interferometer tip*, Journal of Lightwave Technology, Vol. 27, pp. 5426-5429, 2009.

44. Y. J. Rao, M. Deng, D. W. Duan, X. C. Yang, T. Zhu, C. H. Cheng, *Micro Fabry-Perot interferometers in silica fibers machined by femtosecond laser*, Optics Express, Vol. 5, pp. 14123-14128, 2007.

45. Z. L. Ran, Y. J. Rao, W. J. Liu, X. Liao, K. S. Chiang, *Laser-micromachined Fabry-Perot optical fiber tip sensor for high-resolution temperature-independent measurement of refractive index*, Optics Express, Vol. 16, pp. 2252-2263, 2008.

46. T. Wei, Y. Han, H. L. Tsai, H. Xiao, *Miniaturized fiber inline Fabry-Perot interferometer fabricated with a femtosecond laser*, Optics Letters, Vol. 33, pp. 536-538, 2008.

47. X. Wan, H. F. Taylor, *Intrinsic fiber Fabry-Perot temperature sensor with fiber Bragg grating mirrors,* Optics Letters, Vol. 27, pp. 1388-1390, 2002.

48. Z. Wang, F. Shen, L. Song, X. Wang, A. Wang, *Multiplexed fiber Fabry-Pérot interferometer sensors based on ultrashort Bragg gratings*. IEEE Photonics Technology Letters, Vol. 19, pp. 622-624, 2007.

49. Y. Zhang, X. Chen, Y. Wang, K. L. Cooper, A. Wang, *Microgap multicavity Fabry-Pérot biosensor*, Journal of Lightwave Technology, Vol. 25, pp. 1797-1804, 2007.

50. V. R. Machavaram, R. A. Badcock, G. F. Fernando, *Fabrication of intrinsic fibre Fabry-Perot sensors in silica using hydrofluoric acid etching*, Sensors and Actuators A, Vol. 138, pp. 248-260, 2007.

51. J. R. Zhao, X. G. Huang, W. X. He, J. H. Chen, *High-resolution and temperature-insensitive fiber optic refractive index sensor based on Fresnel reflection modulated by Fabry-Perot interference*, Journal of Lightwave Technology, Vol. 28, pp. 2799-2803, 2010.

52. P. Morris, A. Hurrell, A. Shaw, E. Zhang, P. Beard, *A Fabry-Perot fiber-optic ultrasonic hydrophone for the simultaneous measurement of temperature and acoustic pressure*, Journal Acoustical Society of America, Vol. 125, pp. 3611-3622, 2009.

53. H. Liu, H. Z. Yanga, X. Qiao, M. Hu, Z. Feng, R. Wang, Q. Rong, D. S. Gunawarden, K. S. Lim, H. Ahmad, Strain measurement at high temperature environment based on Fabry-Perot interferometer cascaded fiber regeneration grating, Sensors and Actuators A, Vol. 248, pp. 199-205, 2016.

54. C. L. Lee, H. J. Chang, Y. W. You, G. H. Chen, J. M. Hsu, J. S. Horng, *Fiber Fabry-Perot interferometers based on air-bubbles/liquid in hollow core fibers*, IEEE Photonics Technology Letters, Vol. 26, pp. 749-752, 2014.

55. L. Jin, B. O. Guan, H. F. Wei, *Sensitivity characteristics of Fabry-Perot pressure sensors based on hollow-core microstructured fibers*, Journal of Lightwave Technology, Vol. 3, pp. 2526-2532, 2013.

56. K. P. Koo, M. L. LeBlanc, T. E. Tsai, S. T. Vohra, *Fiber-chirped grating Fabry-Perot sensor with multiple-wavelength-addressable free-spectral ranges*, IEEE Photonics Technology Letters, Vol. 10, pp. 1006-1008, 1998.

57. S. Liu, Y. P. Wang, C. R. Liao, G. J. Wang, Z. Y. Li, Q. Wang, J. T. Zhou, K. M. Yang, X. Y. Zhong, J. Zhao, J. Tang, *High-sensitivity strain sensor based on in-fiber improved Fabry-Perot interferometer*, Optics Letters, Vol. 39, pp. 2121-2124, 2014.

58. R. M. Andre, S. Pevec, M. Becker, J. Dellith, M. Rothhardt, M. B. Marques, D. Donlagic, H. Bartelt, O. Frazão, *Focused ion beam post-processing of optical fiber Fabry-Perot cavities for sensing applications*, Optics Express, Vol. 22, pp. 13102-13108, 2014.

59. S. C. Gao, W. G. Zhang, Z. Y. Bai, H. Zhang, W. Lin, L. Wang, J. L. Li, *Microfiber-enabled in-line Fabry-Perot interferometer for high-sensitive force and refractive index sensing*, Journal Lightwave Technology, Vol. 32, pp. 1682-1688, 2014.

60. A. Zhou, B. Y. Qin, Z. Zhu, Y. X. Zhang, Z. H. Liu, J. Yang, L. B. Yuan, *Hybrid structured fiber-optic Fabry-Perot interferometer for simultaneous measurement of strain and temperature*, Optics Letters, Vol. 39, pp. 5267-5270, 2014.

61. C. L. Lee, H. Y. Ho, J. H. Gu, T.Y. Yeh, C. H. Tseng, *Dual hollow core fiber-based Fabry–Perot interferometer for measuring the thermo-optic coefficients of liquids*, Optics Letters, Vol. 40, pp. 459-462, 2015.

62. B. Sun, Y. Wang, J. Qu, C. Liao, G. Yin, J. He, J. Zhou, J. Tang, S. Liu, Z. Li, Y. Liu, *Simultaneous measurement of pressure and temperature by employing Fabry-Perot interferometer based on pendant polymer droplet*, Optics Express, Vol. 23, pp. 1906-1911, 2015.

63. S. Liu, K. M. Yang, Y. P. Wang, J. L. Qu, C. R. Liao, J. He, Z. Y. Li, G. L. Yin, B. Sun, J. T. Zhou, G. J. Wang, J. Tang, J. Zhao, *High-sensitivity strain sensor based on in-fiber rectangular air bubble*, Scientific Reports, Vol. 5, pp. 1-7, 2015.

64. G. G. Liu, M. Han, W. L. Hou, *High-resolution and fast-response fiber-optic temperature sensor using silicon Fabry-Perot cavity*, Optics Express, Vol. 23, pp. 7237-7247, 2015.

65. T. G. Liu, J. D. Yin, J. F. Jiang, K. Liu, S. Wang, S. L. Zou, *Differential-pressure-based fiber-optic temperature sensor using Fabry-Perot interferometry*, Optics Letters, Vol. 40, pp. 1049-1052, 2015.

66. G. K. B. Costa, P.M. P. Gouvêa, L. M. B. Soares, J. M. B. Pereira, F. Favero, A. M. B. Braga, P. P. Muhoray, A. C. Bruno, I. C. S. Carvalho, *In-fiber Fabry-Perot interferometer for strain and magnetic field sensing*, Optics Express, Vol. 24, pp. 14690-14696, 2016.

67. R. Wang, Z. Liu, X. Qiao, *Fringe visibility enhanced Fabry-Perot interferometer and its application as gas refractometer*, Sensors and Actuators B, Vol. 234, pp. 498-502, 2016.

68. X. Liu, M. Jiang, Q. Sui, F. Song, *Temperature sensitivity characteristics of HCPCF-based Fabry–Perot interferometer*, Optics Communications Vol. 359, pp. 322-328, 2016.

69. S. Novais, M. S. Ferreira, J. L. Pinto, *Fabry-Perot cavity based on air bubble for high sensitivity lateral load and strain measurements*, Proc. SPIE 10453, III International Conference on Applications of Optics and Photonics, 104532V, 22 August, Faro, Portugal, 2017.

70. M. F. S. Ferreira, G. S. Barabach, D. Kowal, P. Mergo, W. Urbanczykb, O. Frazão, *Fabry-Perot cavity based on polymer FBG as refractive index sensor*, Optics Communications Vol. 394, pp. 37-40, 2017.

71. W. P. Chen, D. N. Wang, Ben Xu, C. L. Zhao, H. F. Chen, *Multimode fiber tip Fabry-Perot cavity for highly sensitive pressure Measurement*, Scientific Reports, Vol. 368, pp. 1-6, 2017.

72. Novais, M. S. Ferreira, J. L. Pinto, *Lateral load sensing with an optical fiber inline microcavity*, IEEE Photonics Technology Letters, Vol. 29, pp. 1502-1505, 2017.

73. X. Zhang, W. Peng, L.Y. Shao, W. Pan, L. Yan, *Strain and temperature discrimination by using temperature-independent FPI and FBG*, Sensors and Actuators A, Vol. 272, pp. 134-138, 2018.

74. J. Tian, Y. Jiao, S. Ji, X. Dong, Y. Yao, *Cascaded-cavity Fabry-Perot interferometer for simultaneous measurement of temperature and strain with cross-sensitivity compensation*, Optics Communications Vol. 412, pp. 121-126, 2018.

75. P. Chen, X. Shu, *Refractive-index-modified-dot Fabry-Perot fiber probe fabricated by femtosecond laser for high-temperature sensing*, Optics Express, Vol. 26, pp. 5292-5299, 2018.

76. S. Novais, M. S. Ferreira, J. L. Pinto, *Optical fiber Fabry-Perot tip sensor for detection of water-glycerin mixtures*, Journal of Lightwave Technology, Vol. 36, pp. 1576-1582, 2018.

77. S. Liu, Y. Ji, J. Yang, W. Sun, H. Li, *Nafion film temperature/humidity sensing based on optical fiber Fabry-Perot interference*, Sensors and Actuators A,Vol. 269, pp. 313-321, 2018.

78. Y. Zhao, Y. Jin, H. Liang, *Investigation on single-mode-multimode-single-mode fiber structure*, Symposium on Photonics and Optoelectronics, 16-18 May, Wuhan, China, 2011.

79. S. M. Tripathi, A. Kumar, R. K. Varshney, B. P. Kumar, E. Marin, J. P. Meunier, *Strain and temperature sensing characteristics of singlemode- multimode-single-mode structures*, Journal of Lightwave Technology, Vol. 27 , pp. 2348-2356, 2009.

80. A. Mehta, W. Mohammed, E. G. Johnson, *Multimode interference based fiber-optic displacement sensor*, IEEE Photonics Technology Letters, Vol. 15, pp. 1129-1131, 2003.

81. Q. Wang, G. Farrell, *All-fiber multimode-interference-based refractometer sensor: proposal and design*, Optics Letters, Vol. 31, pp. 317-319, 2006.

82. A. Kumar, R. K. Varshney, R. Kumar, *SMS fiber optic microbend sensor structures: Effect of the modal interference*, Optics Communications, Vol. 232, pp. 239-244, 2004.

83. L. B. Soldano, E. C. M. Penning, *Optical multi-mode interference devices based on self-imaging: principles and applications*, Journal of Lightwave Technology, Vol. 13, pp. 615-627, 1995.

84. X. Zhou, K. Chen, X. Mao, W. Peng, Q. Yu, *A reflective fiber-optic refractive index sensor based on multimode interference in a coreless silica fiber*, Optics Communications, Vol. 340, pp. 50-55, 2015.

85. C. Elousa, F. J. arregui, I. D. Villar C. R. Zamarreno, J. M. Corres, C, Bariain, J. Goicoechea, M. Hernaez, P. J. Rivero, A. B. Socorro, *Micro and nanostructured materials for the development of optical fibre sensors*, Sensors, Vol. 17, pp. 1-38, 2017.

86. M. Yang, J. Dai, *Review on optical fiber sensors with sensitive thin films*, Photonic Sensors, Vol. 2, pp. 14-28, 2012.

87. I. Del Villar, M. Partridge, W. E. Rodriguez, O. Fuentes, A. B. Socorro, S. Diaz, J. M. Corres, S. W. James, R. P. Tatam, *Sensitivity enhancement in low cutoff wavelength long-period fiber gratings by cladding diameter reduction*, Sensors, Vol. 17, pp. 2094, 2017.

88. Y. Zhao, L. Cai, X. G. Li, F. C. Meng, Z. Zhao, *Investigation of the high sensitivity RI sensor based on SMS fiber structure*, Sensors and Actuators A, Vol. 205, pp. 186-190, 2014.

89. W. Han, Z. Tong, Y. Cao, *Simultaneous measurement of temperature and liquid level base on core-offset singlemode–multimode–singlemode interferometer*, Optics Communications, Vol. 321, pp. 134-137, 2014.

90. H. Sun, M. Hu, Qi. Rong, Y. Du, H. Yang, X. Qiao, *High sensitivity optical fiber temperature sensor based on the temperature cross-sensitivity feature of RI-sensitive device*, Optics Communications, Vol. 323, pp. 28-31, 2014.

91. J. Fan, J. Zhang, P. Lu, M. Tian, J. Xu, D. Liu, *A single-mode fiber sensor based on core-offset inter-modal interferometer*, Optics Communications Vol. 320, pp. 33-37, 2014.

92. Luo, L. Xia, C. Yu, W. Li, Q. Sun, Y. Wang, D. Liu, *Multi-parameter optical fiber sensor based on enhanced multimode interference*, Optics Communications, Vol. 344, pp. 120-124, 2015.

93. L. Ma, Z. Kang, Y. Qi, S. Jian, *Fiber-optic temperature sensor based on a thinner no-core fiber*, Optik, Vol. 126, pp. 1044–1046, 2015.

94. X. Hao, Z. Tong, W. Zhang, Y. Cao, *A fiber laser temperature sensor based on SMF core-offset structure,* Optics Communications, Vol. 335, pp. 78-81, 2015.

95. P. Hu, Z. Chen, M. Yang, J. Yang, C. Zhong, *Highly sensitive liquid-sealed multimode fiber interferometric temperature sensor,* Sensors and Actuators A, Vol. 223, pp. 114-118, 2015.

96. Z. Wang, Z. Tan, R. Xing, L. Liang, Y. Qi, S. Jian, *Liquid level sensor based on fiber ring laser with single-mode-offset coreless-single-mode fiber structure*, Optics & Laser Technology, Vol. 84, pp. 59-63, 2016.

97. X. Liu, X. Zhang, Y. Liu, Z. Liu, W. Peng, *Multi-point fiber-optic refractive index sensor by using coreless fibers*, Optics Communications, Vol. 365, pp. 168-172, 2016.

98. Y. Ran, L. Xia D. Niu, Y. Wen, C. Yu, D. Liu, *Design and demonstration of a liquid level fiber sensor based on self-imaging effect*, Sensors and Actuators A, Vol. 237, pp. 41-46, 2016.

99. S. E. F. Masnan, A. Z. Zulkifli, N. M. Azmi, S. M. Akib, H. A. Razak, H. Arof, S. W. Harun, *Steel beam compressive strain sensor using single-mode-multimode-single-mode fiber structure*, IEEE Photonics Journal, Vol. 8, pp. 1-7, 2016.

100. Y. Sun, D. Liu, P. Lu, Q. Sun, W. Yang, S. Wang, L. Liu, W. Ni, *High sensitivity optical fiber strain sensor using twisted multimode fiber based on SMS structure*, Optics Communications, Vol. 405, pp. 416-420, 2017.

101. C. Zhang, T. Ning, J. Li, L. Pei, C. Li, H. Lin, *Refractive index sensor based on tapered multicore fiber*, Optical Fiber Technology, Vol. 33, pp. 71-76, 2017.

102. S. P. Chew, A. Z. Zulkifli, H. Hamad, S. W. Harun, L. Y. Lee, H. A. Razak, F. R. M. Adikan, *Singlemode-multimode-singlemode fiber structure as compressive strain sensor on a reinforced concrete beam*, Optik, Vol. 154, pp. 705-710, 2018.

103. K. Tian, G. Farrell, X. Wang, Y. Xin, Y. Du, W. Yang, H. Liang, E. Lewis, P. Wang, *High sensitivity temperature sensor based on singlemode-no-core-singlemode fibre structure and alcohol*, Sensors and Actuators: A. Physical, pp. 1-8, 2018.

104. X, Fu, F. Liu, Y. Zhang, J. Wen, D. Wang, H. Xie, G. Fu, W. Bi, *A refractive-index sensitivity-enhanced sensor by core-offset splicing the triple cladding quartz specialty fiber*, Optical Fiber Technology, Vol. 46, pp. 63-67, 2018.

105. W. E. R. Rodríguez, I. D. Villar, C. R. Zamarreno, I. R. Matias, F. J. Arregui, A. J. R. Rodríguez, R. F. D. Cruz, *Sensitivity enhancement experimental demonstration using a low cutoff wavelength SMS modified structure coated with a pH sensitive film*, Sensors and Actuators B, Vol. 262, pp. 696-702, 2018.

106. Susana Novais, Catarina I. A. Ferreira, Marta S. Ferreira, João L. Pinto, *Optical fiber tip sensor for the measurement of glucose aqueous solutions*, IEEE, Photonics Journal, Vol. 10, pp. 1-9, 2018.

107. Susana Novais, Marta S. Ferreira, João L. Pinto, *Relative humidity fiber sensor based on multimode interferometer coated with agarose gel*, submitted to Coatings, 2018.

108. Susana Novais, Marta S. Ferreira, João L. Pinto, *Determination of thermo-optic coefficient of ethanol-water mixtures with optical fiber tip*, Optical Fiber Technology, Vol. 45, pp. 276-279, 2018.

II

Internal and external temperature monitoring of a Li-ion battery with fiber Bragg grating sensors

Published in Sensors, Vol. 16, no. 1394, August 30, 2016

DOI: 10.3390/s16091394

Internal and external temperature monitoring of a Li-ion battery with fiber Bragg grating sensors

Susana Novais, Micael Nascimento, Lorenzo Grande, M. Fátima Domingues, Paulo Antunes, Nélia Alberto, Cátia Leitão, Ricardo Oliveira, Stephan Koch, Guk Tae Kim, Stefano Passerini and João Pinto

Abstract: The integration of fiber Bragg grating (FBG) sensors in lithium-ion cells for *in-situ* and *operando* temperature monitoring is presented herein. The measuring of internal and external temperature variations was performed through four FBG sensors during galvanostatic cycling at C-rates ranging from 1 C to 8 C. The FBG sensors were placed both outside and inside the cell, located in the center of the electrochemically active area and at the tab-electrode connection. The internal sensors recorded temperature variations of 4.0 ± 0.1 °C at 5 C and 4.7 ± 0.1 °C at 8 C at the center of the active area, and 3.9 ± 0.1 °C at 5 C and 4.0 ± 0.1 °C at 8 C at the tab-electrode connection, respectively. This study is intended to contribute to detection of a temperature gradient in real time inside a cell, which can determine possible damage in the battery performance when it operates under normal and abnormal operating conditions, as well as to demonstrate the technical feasibility of the integration of *operando* microsensors inside Li-ion cells.

Keywords: Embedded sensors; Li-ion batteries; temperature monitoring; performance; safety.

1. Introduction

Lithium-ion batteries have a widespread use as power sources in portable electronics, as well as in hybrid and pure electric vehicles, due to their high specific energy, long life cycle and low self-discharge [1, 2]. The first and utmost challenge in designing a Li-ion battery system is to ensure its inherent safety under both normal and abuse operating conditions. To this goal, knowledge of the internal thermal behavior is therefore critical [3–5]. The main underlying concern is related to the significant temperature variation under high charge/discharge rates [2]. The excess heat generated during over-charge/discharge or in the presence of short circuits may cause irreversible damage in cells and eventually lead to explosion or combustion [6,7].

It is known from the literature that the temperature near the positive electrode is higher than that near the negative one, due to the lower electrical conductivity of most cathode active materials [4]. In order to develop a satisfactory thermal management strategy and to increase the performance and lifetime of Li-ion batteries, it is essential to monitor and manage both the internal and external temperature [8, 9]. Normally, the thermal monitoring of batteries is performed on their surface through the use of thermocouples or electro-mechanical sensors [10, 11].

Internal monitoring, however, is challenging due to the chemically aggressive and electrically noisy environment, for which sensors with low invasiveness, mechanical robustness, immunity to electromagnetic radiation, and resistance to corrosion are required. Sensors based on fiber Bragg gratings (FBG) are an effective method to perform both static and dynamic measurements of temperature, pressure, refractive index, strain, and bending [12]. FBG-based sensors have the advantages of being very small, flexible, immune to electromagnetic interference and electrostatic discharge and also present multiplexing capabilities. All these features make them a suitable solution for the monitoring of lithium batteries and fuel cells, as previously explored in [5, 13–16]. FBG sensors have also been used to monitor the strain evolution of electrodes in lithium-ion batteries [17].

In this study, the *operando* monitoring of a Li-ion cell's internal and external temperature variations, using FBG sensors, is presented. The analysis of the internal temperature evolution during galvanostatic cycling at different C-rates provides a step forward in the understanding and safety improvement of future Li-ion battery systems.

2. Experimental setup and testing

2.1. Silica fiber stability test

To test the silica fibers chemical stability[1] when immersed in conventional Li-ion battery electrolytes, some 2-3 cm long fiber samples were stored in polyethylene (PE) vials

[1] Please see the Additional Information Section at the end of this Chapter for more details.

together with a solution of $LiPF_6$ in 50:50 wt. % EC: DMC (LP30, Sigma Aldrich, Munich, Germany). The $LiPF_6$ salt contained in the electrolyte is known to react with water impurities and form hydrofluoric acid (HF), which has both a detrimental effect on the battery performance and poses a hazard risk. Given the reactivity of HF towards silicon oxide, which the FBG sensors are constituted of, small amounts of water were added to probe the sensors' chemical reactivity and their degree of dissolution into the cell environment. Deionized water (Milli-Q, Merck Millipore) was added in ppm (100, 500 and 1000) amounts to simulate different levels of electrolyte contamination. The amount of dissolved Si was determined by means of ICP-OES (5100, Agilent Technologies, Santa Clara - California, USA).

2.2. Fiber Bragg grating sensors

The FBG sensors were inscribed on commercially available photosensitive optical fiber (Fibercore PS1250/1500) by the phase mask method[2]. The UV radiation system used was a pulsed excimer laser (KrF) (Industrial BraggStar, Coherent), emitting at a wavelength of 248 nm, 4 mJ/pulse (20 ns duration) and 500 Hz repetition rate. Two different fiber cables were prepared, each with two 0.3 cm length FBGs, spaced by 2 cm. The Bragg wavelength variations were monitored using an interrogation system (sm 125-500, Micron Optics Inc., Atlanta, USA) with a sample rate of 2 Hz and a wavelength accuracy of 1 pm.

2.3. Li-ion cell assembly and microsensor integration

Li-ion pouch cells were assembled using a commercial lithium iron phosphate (LFP, Clariant) cathode (91:4:5 LFP:Super C65:JSR, 12 $mg \cdot cm^{-2}$ active mass loading) and a graphite anode (92:3:5 SBG-1:Super C65:CMC, supplied by SGL Carbon, 5.6 $mg \cdot cm^{-2}$ active mass loading) with an active area of 16 cm^2, following a procedure already described in literature [18]. Aluminum and nickel tabs were used as cathode and anode current collectors, respectively. The Li-ion pouch cell assembly was carried out inside the

[2] More information regarding the FBG inscription method is given in the Additional Information Section at the end of this Chapter.

dry room (relative humidity < 0.1 % at 20 °C), where all materials were stored prior to usage. Two sheets of a single layer polyolefin membrane (Hipore SV718, 10 μm, Asahi Kasei, Tokyo, Japan) drenched in a 1 M solution of LP30 were used as separator[3]. The cells showed a capacity at 1 C of 20 ± 1 mAh.

The internal FBG sensors were placed between the two separators layers, at the center of the electrochemically active area and near the tab-electrode connection, and named IC (Internal Center) and IT (Internal Tab-electrode), respectively. The Li-ion pouch cells were heat-sealed under vacuum.

The external sensors were laid down in direct contact with the surface of the pouch cell, parallel to the above mentioned internal ones and named EC (External Center) and ET (External Tab-electrode), as presented in Figure II.1. To increase both the contact area and the thermal conductivity, a thermal paste (Amasan Heat transfer compounds, T12) was used to attach them to the pouch cells. It should be noted that, as the cells' thickness is very small (~1 mm), any possible strain variations were considered null, with temperature variations being the only source of the Bragg wavelength oscillations. The tests were repeated on two different cells and similar results were obtained.

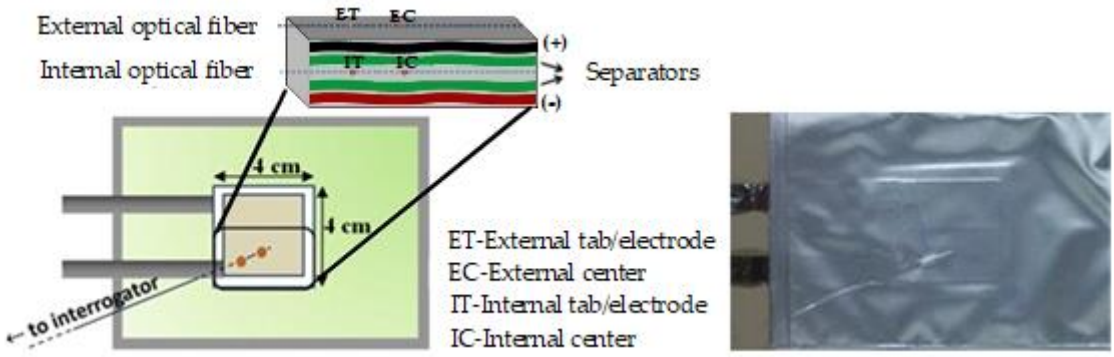

Figure II.1. Schematic diagram of internal and external FBG sensors positions. Photograph of a pouch cell with the embedded sensors.

[3] Please see the Additional Information Section at the end of this Chapter for more details.

2.4. Thermal calibration of FBG sensors

The FBG sensors were calibrated on a thermal chamber (Model 340, Challenge Angelantoni Industry) between 10 °C and 35 °C, in 5 °C steps. Sensitivities of 8.55 ± 0.12 pm/°C (r^2 = 0.999) and 8.25 ± 0.12 pm/°C (r^2 = 0.994), for ET and EC, respectively, were obtained for the external FBG sensors. To the internal FBG sensors, sensitivities of 10.24 ± 0.10 pm/°C (r^2 = 0.992) and 10.27 ± 0.10 pm/°C (r^2 = 0.983) were determined for IT and IC, respectively.

2.5. Electrochemical testing

The cycling tests were performed using a potentiostat/galvanostat (SP-150, Bio-Logic) at different C rates (1 C, 2 C, 5 C and 8 C)[4]. The influence of the room temperature variations was reduced using a Peltier plate connected to a temperature controller (5305 TEC Source), thus maintaining the battery at the selected temperature 20.0 ± 0.5 °C. The corresponding experimental setup is illustrated in Figure II.2.

The subsequent step was the identification of the FBG sensors response to different electrochemical inputs. For this reason, the assembled cells were subjected to a cycling protocol involving a series of differing galvanostatic/potentiostatic and open circuit voltage steps, presented in Table II.1.

Table II.1. Electrochemical test protocol.

(1)	Constant Current Constant Voltage (CCCV) charge
(2)	Two cycles each composed of Constant Current (CC) discharge followed by CCCV charge
(3)	Open Circuit Voltage (OCV)
(4)	CC discharge

[4] More information regarding the electrochemical testing in the Additional Information Section at the end of this Chapter.

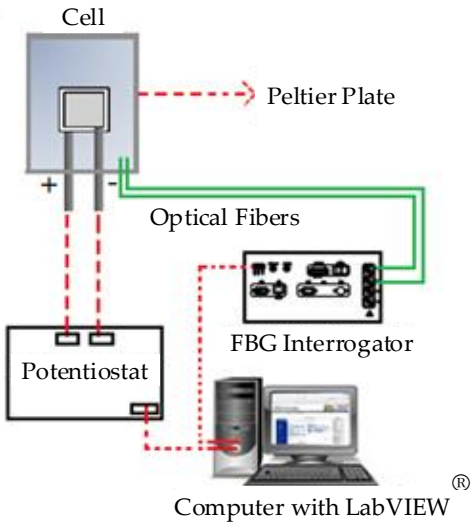

Figure II.2. Experimental setup diagram.

3. Results and discussion

3.1. Silica fiber chemical inertness study

Four polyethylene vials containing differing amounts of deionized water (0, 100, 500 and 1000 ppm) were analyzed[5] . By the amount of Si dissolved from the fiber into the LP30 electrolyte after two weeks of storage, only small Si amounts were detected through ICP-OES (0.5–1.1 wt. %). Assuming uniform fiber dissolution, this only corresponds to the removal of a few atomic layers from the fiber surface. The optical fibers were also inspected under the microscope and no changes were observed. Taking this into consideration, the FBG sensor sensitivity and response is not expected to be altered, since the Bragg grating itself is recorded at the fiber core. A possible small attack of the cladding would not influence the FBG signal; hence, the findings confirm the suitability of glass fiber–based sensors to be used in a Li-ion pouch cell environment.

[5] More information regarding silica fiber chemical inertness study, in the Additional Information Section at the end of this Chapter.

3.2. Analysis of the FBG sensors response under different operating conditions

The typical response of FBG sensors during constant current (CC) discharge and constant current constant voltage (CCCV) charge half-cycles is shown in Figure II.3. It is clear that the temperature rises steadily during CC charge as well as CC discharge. It is also worth noting the presence of at least two shoulders in the peak related to the CC discharge, possibly related to the different staging levels of graphite during intercalation. As soon as the applied current is lowered during the subsequent open circuit voltage (OCV) and constant voltage (CV) charge step, the temperature returns to the initial value. The baseline of the sensor signal was experimentally found to vary by ± 0.1 °C in all experiments. The origin of those slight fluctuations is not very clear, but is assumed to be correlated with external temperature variations (imperfect temperature conditioning due to the Peltier element only) and strain signals, which are neglected in this study.

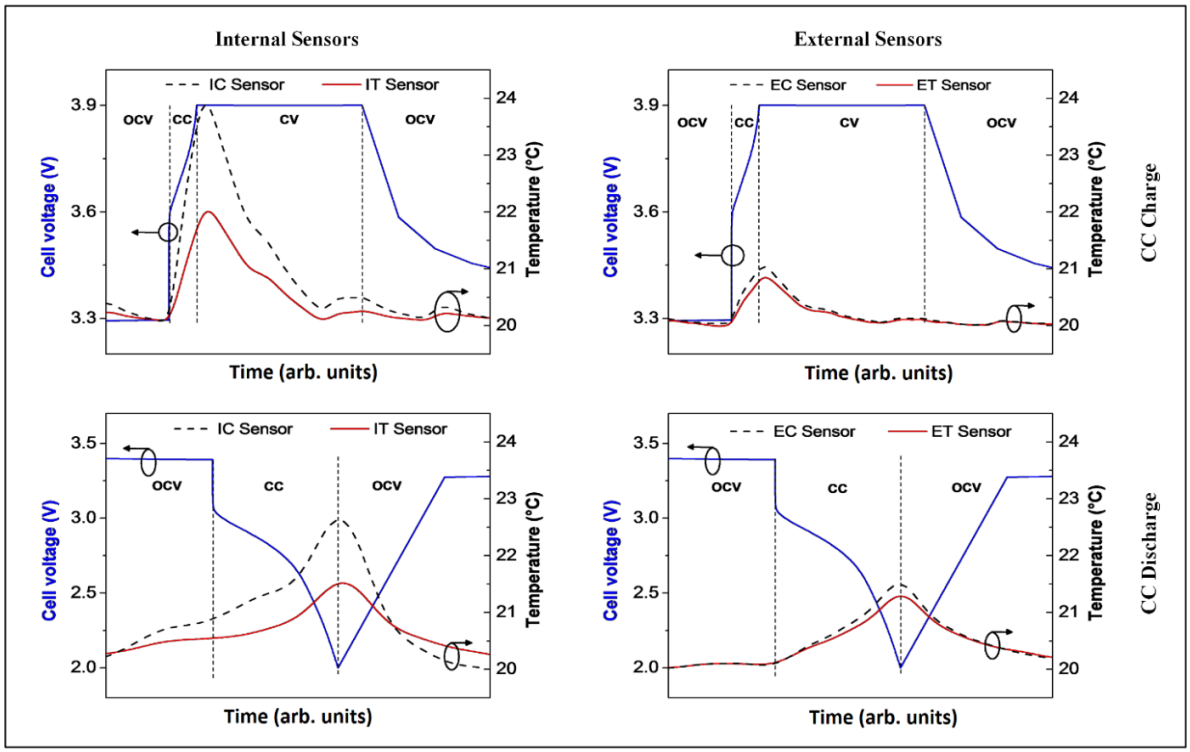

Figure II.3. Temperature changes observed with all four sensors before, during and after a CC discharge or CCCV charge half cycle (C-rate was 5 C) followed by an OCV step.

The temperature increase during CC charge was observed to be similar to CC discharge. However, there is a strong difference of the ΔT values detected by internal vs. external sensors (Figure II.3, left-hand side vs. right-hand side). The internal sensors directly measure the heat generated inside the battery. The external sensor's signal was not only found to be slightly delayed with respect to the internal signal, but also the observed temperature variations are significantly lower outside the pouch bag due to the heat dissipation to the outside. Still, the general trend observed with the internal sensors is also detected by the external ones (heating during CC vs. relaxation during CV steps and at OCV).

The sensors implemented in the cell recorded a larger ΔT (4.0 ± 0.1) °C, while only (1.5 ± 0.1) °C was observed for external measurements at the center of the active area (IC vs. EC). This proves that, even in the thin single-layer cells studied here, heat dissipation does not happen immediately and, hence, is not negligible [19]. Thus, internal temperature measurements provide much more insight and a more reliable basis for the modeling of the thermal behavior of Li-ion cells. Cells used commercially, especially for mobile device applications, are rarely under the OCV condition, but are often subjected to continuous cycling. In fact, strong heating of the batteries inside smartphones is an everyday experience. This is not only unpleasant, but also deleterious to the cell life as high temperatures favor electrolyte decomposition. A better understanding of the temperature variations in Li-ion cells under heavy-duty cycling, accessible with the sensors presented in this work, is key for the improvement of cell components as well as battery management systems.

Figure II.4 shows the temperature changes upon CC discharge followed directly by CCCV charge. The temperature curve of the initial CC discharge is the same as that shown before in Figure II.3. However, a direct CC charging does not lead to an ongoing temperature rise. In contrast, reversing the current induces an initial temperature drop followed by another increase after a short time, resulting in an overall higher ΔT (3.0 ± 0.1) °C than that observed during OCV separated half-cycles.

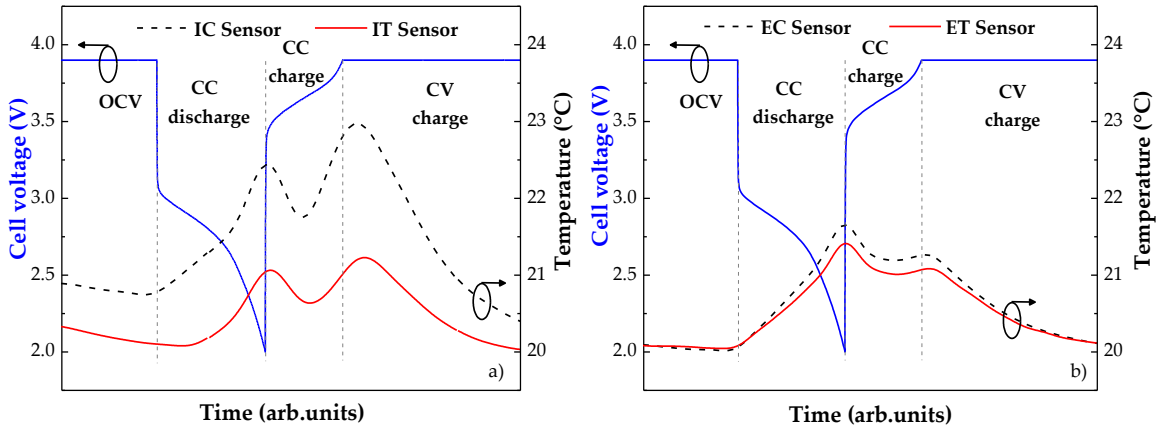

Figure II.4. Temperature changes observed with the four sensors during cycling with a CC discharge followed directly by a CCCV charge (C-rate was 5 C), where 4a) is for the internal sensors, and 4b) for the external ones.

During the CV charge step, where the current density decays exponentially, the temperature falls back to the surrounding temperature (controlled with the Peltier element). It can safely be assumed that this peculiar shape of the temperature curve is correlated with the concentration gradient inside the Li-ion cell. A relaxation of the gradient due to current reversing (from discharge to charge) or less current density (CV step) undoubtedly leads to thermal relaxation, i.e., faster heat dissipation than generation.

To further investigate the role of the current density, which determines the extent of cell polarization, a C-rate test was performed, comprising a series of five cycles (CC discharge + CCCV charge) at each C-rate. Figure II.5 shows the correlation of the C-rate with the maximum ΔT recorded during cycling.

As Figure II.5 highlights, the proximity of the internal sensors to the areas where electrochemical processes occur and heat is generated yields ΔT values that are higher than those recorded by the external sensors. The latter are unable to detect variations as high as 4.0 °C in this test setup.

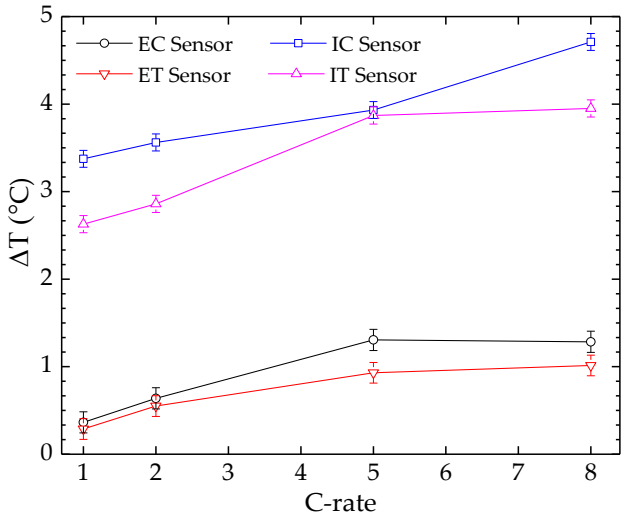

Figure II.5. Correlation of the C-rate with the maximum ΔT recorded during cycling.

The cells studied in this work were sealed inside an aluminum pouch bag foil much larger than the cell active area (100 cm^2 vs. 16 cm^2). It is possible that the heat generated inside the cell, which is directly recorded by the internal sensors, is dissipated over the whole pouch bag, leading to the smaller temperature changes observed with the external sensors. However, the difference in absolute ΔT values for internal and external measurements is expected to be higher for commercial cells with a high degree of electrode layer stacking, hence a more difficult way for heat dissipation. Optimized cell packaging (both casing materials and cell arrangement in full battery packs) and active cooling (especially for large batteries such as those in automotive applications) are therefore crucial to avoid dangerous temperatures inside Li-ion battery cells. In addition, permanent and immediate control of the internal temperature, as is feasible with the FBG sensor technology presented in this work, offers the possibility of the safe operation of Li-ion batteries by early detection of heat generation. Such direct temperature control is not possible with any other existing technology.

In Figure II.6, the temperature variations observed internally and externally at 5 C and 8 C, respectively, are illustrated.

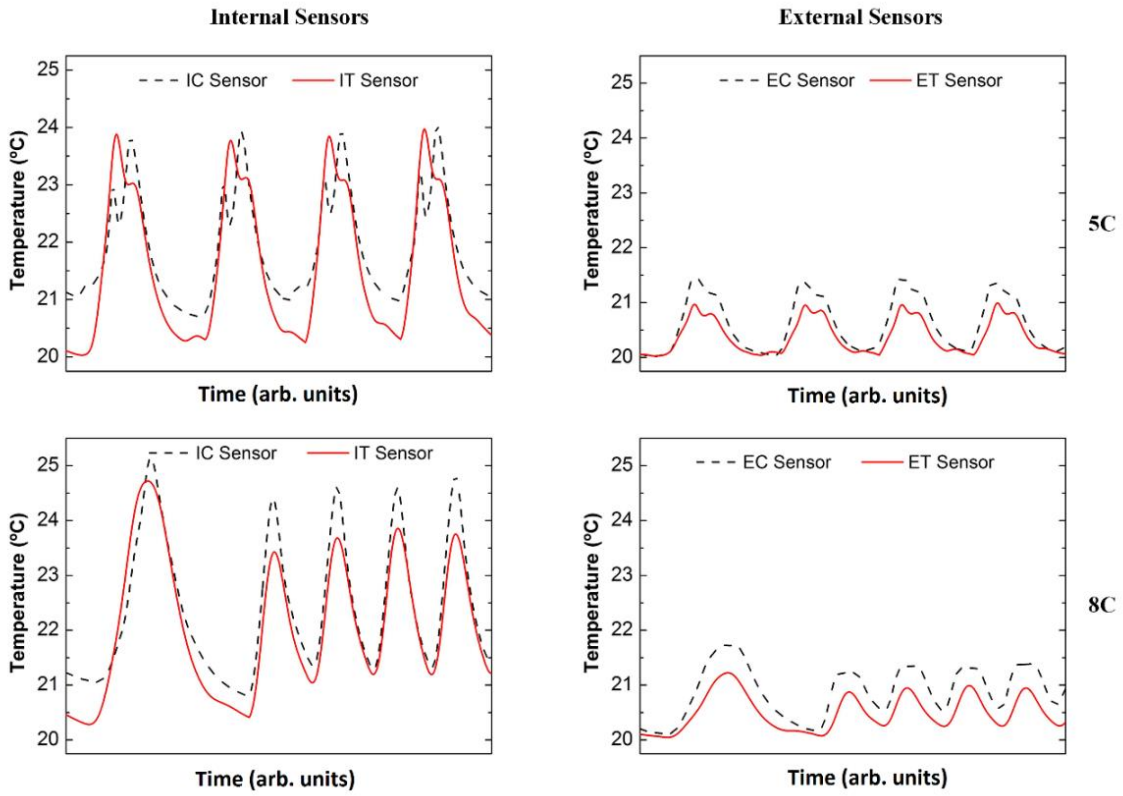

Figure II.6. Temperature variations observed internally and externally at 5 C and 8 C.

By comparing the FBG signals, no time delay related to the temperature variations is observed for any of the sensors, indicating that the response is always nearly instantaneous, irrespective of the positioning. Additionally, while it is still possible to distinguish two ΔT peaks corresponding to discharge and charge at 5 C, respectively (Figure II.6, top), at 8 C these two features are merged into one single broad peak (Figure II.6, bottom). This might be a direct result of the short time that separates the establishment of the two opposite concentration gradients. However, it is possible that the short cycle duration at 8 C (caused by the poor rate capability of the tested cells) does not actually lead to a full establishment of the concentration gradient, hence mitigating possible relaxation effects upon the current reversing. During the first cycle at 8 C, the maximum temperature variation of 4.0 ± 0.1 °C was detected by the IC sensor, while the IT sensor detected a value of about 4.7 ± 0.1 °C. Externally, the values detected by ET and EC are in the range of 1.5 ± 0.1 °C, indicating that the aluminum pouch bag foil allows the cell to equilibrate with the ambient temperature.

4. Conclusions

FBG sensors were successfully integrated in Li-ion pouch cells in order to monitor temperature changes during electrochemical testing at different C-rates (1 C, 2 C, 5 C and 8 C). Two different areas (the tab-electrode connection and the center of the electrochemical active area) were monitored, both on the inside and the outside of the pouch cell. The changes in temperature showed a direct correlation with the applied current gradient, with the highest peaks being detected always at the end of charge and discharge. This is in accordance with the fact that, over both charge and discharge, Li-ions migrate inside the cell to establish a concentration gradient, which generates heat as a function of the applied current. The results show that, internally, the cell temperature increased as much as 4.7 ± 0.1 °C. This outcome needs to be taken into account for battery modeling and battery management system purposes, since cell damage caused by overheating is an important reason for capacity fading in Li-ion batteries and thermal runaways are the major source of safety concerns. The FBG sensors were able to detect such temperature changes with a superior response rate, making them useful tools for failure detection in batteries. Their low invasiveness and high tolerance to the chemically aggressive environment inside Li-ion batteries makes them an interesting possibility for integration in commercial Li-ion cells as well as for research purposes for the in-situ study of temperature variations. The goal of the study was to show the functionality of the sensor and the positioning for monitoring the internal and external temperature variations in the active area of lithium batteries. In the near future the authors intend to perform an extension of this work on packs of lithium cells. A relationship between internal and external temperatures either through tables or equations is also expected to be established.

Acknowledgments: This work is funded by the EU Project "Stable Interfaces for Rechargeable Batteries" (SIRBATT) (FP7 ENERGY 2013, grant agreement No. 608502). Susana Novais, Micael Nascimento and M. Fátima Domingues are grateful for the research fellowships no. BI/UI96/6643/2014, BI/UI96/6642/2014 and BI/UI96/7040/2015, respectively. Lorenzo Grande would like to kindly acknowledge the travel grant allocated within the same project to perform this joint

research. Stephan Koch acknowledges the Foundation of German Business. Cátia Leitão and Ricardo Oliveira acknowledge the financial support from FCT through the Doctoral fellowships SFRH/BD/84076/2012 and SFRH/BD/88472/2012, Maria Domingues, Paulo Antunes and Nélia Alberto the Postdoctoral fellowships, SFRH/BPD/101372/2014, SFRH/BPD/76735/2011 and SFRH/BPD/78141/2011. The group at HIU would like to thank the companies Clariant, SGL Carbon, Imeris and Asahi Kasei for providing lithium iron phosphate, graphite conductive carbon and the separator, respectively. This work is also funded by FEDER funds through the COMPETE 2020 Programme, and National Funds through FCT under the projects UID/CTM/50025/2013 and UID/EEA/50008/2013.

Author Contributions: Susana Novais, Micael Nascimento, Lorenzo Grande and Stephan Koch designed the system and performed the experiments; Susana Novais, Micael Nascimento, Maria Domingues, Paulo Antunes, Nélia Alberto, Cátia Leitão, Ricardo Oliveira and João Pinto were focused on the development of the fiber sensor network; Lorenzo Grande, Stephan Koch, Guk-Tae Kim and Stefano Passerini were focused on the sensor integration and cell manufacturing. All authors were involved in the results analysis and paper-writing.
Conflicts of Interest: The authors declare no conflict of interest.

References

1. Chen, J.; Cheng, F. Combination of lightweight elements and nanostructured materials for batteries. *Acc. Chem. Res.* 2009, *42*, 713-723.

2. Kizilel, R.; Sabbah, R.; Selman, J.R.; Al-Hallaj, S. An alternative cooling system to enhance the safety of Li-ion battery packs. *J. Power Sour.* 2009, *194*, 1105-1112.

3. Sethuramana, V.A.; Van Winklea, N.; Abrahamb, D.P.; Bowera, A.F.; Guduru, P.R. Real-time stress measurements in lithium-ion battery negative-electrodes. *J. Power Sour.* 2012, *206*, 334-342.

4. Kima, U.S.; Yia, J.; Shin, C.B. Modelling the thermal behavior of a lithium-ion battery during charge. *J. Power Sour.* 2011, *196*, 5115-5121.

5. Yang, G.; Leitão, C.; Lib, Y.; Pinto, J.; Jiang, X. Real-time temperature measurement with fiber Bragg sensors in lithium batteries for safety usage. *Measurement* 2013, *46*, 3166-3172.

6. Spotnitza, R.M.; Weavera, J.; Yeduvaka, G.; Doughty, D.H.; Roth, E.P. Simulation of abuse tolerance of lithium-ion battery packs. *J. Power Sour.* 2007, *163*, 1080-1086.

7. Roder, P.; Stiaszny, B.; Ziegler, J.C.; Wiemhofer, H.-D. The impact of calendar aging on the thermal stability of a Mn2O4-Li (Ni1/3Mn1/3Co1/3) O2/graphite lithium-ion cell. J. Power Sour. 2014, 268, 315-325.

8. Fan, J.; Tan, S. Studies on charging lithium-ion cells at low temperatures. J. Electrochem. Soc. 2006, 153, A1081-A1092.

9. Huang, C.-K.; Sakamoto, J.S.; Wolfenstine, J.; Surampudi, S. The limits of low-temperature performance of Li-ion cells. *J. Electrochem. Soc.* 2000, *147*, 2893-2896.

10. Kima, U.S.; Shina, C.B.; Kim, C.-S. Effect of electrode configuration on the thermal behavior of a lithium-polymer battery. J. Power Sour. 2008, 180, 909-916.

11. Richardson, R.R.; Ireland, P.T.; Howey, D.A. Battery internal temperature estimation by combined impedance and surface temperature measurement. J. Power Sour. 2014, 265, 254-261.

12. Antunes, P.; Lima, H.; Alberto, N.; Bilro, L.; Pinto, P.; Costa, A.; Rodrigues, H.; Pinto, J.L.; Nogueira, R.; Varum, H.; André, P.S. Optical sensors based on FBG for structural health monitoring. In New Developments in Sensing Technology for Structural Health Monitoring; Mukhopadhyay, S.C., Ed.; Springer-Verlag: Berlin, Germany, 2011.

13. David, N.A.; Wild, P.M.; Hu, J.; Djilali, N. In-fibre Bragg grating sensors for distributed temperature measurement in a polymer electrolyte membrane fuel cell. J Power Sour. 2009, 192, 376-380.

14. Nascimento, M.; Novais, S.; Leitão, C.; Domingues, M.F.; Alberto, N.; Antunes, P.; Pinto, J.L. Lithium batteries temperature and strain fiber monitoring. In Proceedings of the SPIE 9634, 24th International Conference on Optical Fibre Sensors, Curitiba, Brazil, 28 September–2 October 2015; Volume 9634, pp. 9634V-1-9634V-4.

15. Sommer, L.W.; Raghavan, A.; Kiesel, P.; Saha, B.; Schwartz, J.; Lochbaum, A.; Ganguli, A.; Bae, C.-J.; Alamgir, M. Monitoring of Intercalation Stages in Lithium-Ion Cells over Charge-Discharge Cycles with Fiber Optics Sensors. J. Electrochem. Soc. 2015, 162, A2664-A2669.

16. Sommer, L.W.; Kiesel, P.; Ganguli, A.; Lochbaum, A.; Saha, B.; Schwartz, J.; Bae, C.J.; Alamgir, M.; Raghavan, A. Fast and slow ion diffusion processes in lithium ion pouch cells during cycling observed with fiber optic strain sensors. J. Power Sour. 2015, 296, 46-52.

17. Bae, C.; Manandhar, A.; Kiesel, P.; Raghavan, A. Monitoring the Strain Evolution of Lithium-Ion Battery Electrodes using an Optical Fiber Bragg Grating Sensor. Energy Technol. 2016, 4, 1-6.

18. Loeffler, N.; Zamory, J.; Laszczynski, N.; Doberdo, I., Kim, G.-T.; Passerini, S. Performance of $LiNi_{1/3}Mn_{1/3}Co_{1/3}O_2$/graphite batteries based on aqueous binder. *J. Power Sour.* 2014, *248*, 915-922.

19. Srinivasan, R.; Baisden, A.C.; Carkhuff, B.G.; Butler, M.H. The five modes of heat generation in a Li-ion cell under discharge. J. Power Sour. 2014, 262, 93-103.

IIA - Additional Information

The work presented in this Chapter has been complemented with other experiments, whose results were published in a Book Chapter in ***Advances in Sensors: Reviews' Book Series, vol. 5, 2018.*** In this Section, relevant additional information is given, which is based on that publication.

Fiber Bragg gratings inscription

The FBGs used in the first work were written into a 125 μm cladding diameter photosensitive SMF using the interferometric configuration shown in Figure II.7. The laser used to write the FBGs was an excimers laser, emitting at 248 nm, with energy of 5 mJ/pulse, 20 ns pulse duration and 500 Hz repetition rate. Light from the excimers laser is focused by the converging lens and passes through the phase mask, which acts as a beam splitter. The split light is then recombined at the core of the optical fiber, where a modulation of the effective refractive index occurs, originating the FBG.

The estimated length of the grating was of ~3 mm, derived from the laser spot length and the slit aperture.

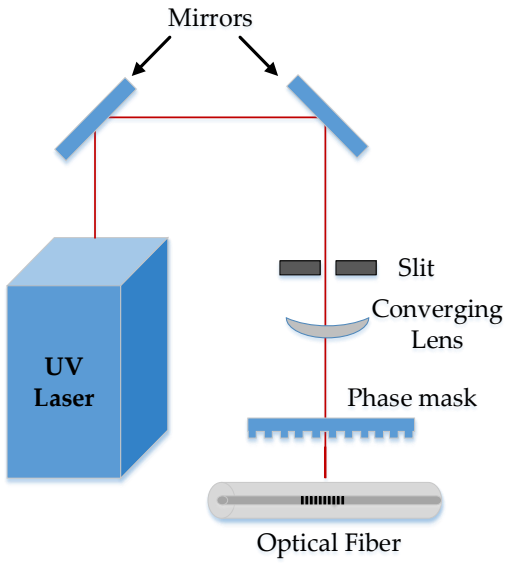

Figure II.7. Scheme setup of the FBG inscription.

Silica fiber chemical inertness study

The integration of sensors in Li-ion pouch cells can be a very interesting solution to better understand the temperature variations within the cell and for a more accurate monitoring. However, considering the chemically active environment inside a battery, the insertion of an optical fiber in such medium requires a previous analysis of its chemical inertness. The silica fibers chemical stability was tested by immersing 2-3 cm long fiber samples in a solution of $LiPF_6$ in 50:50 wt. % EC: DMC. The $LiPF_6$ salt contained in the electrolyte is known to react with water impurities and form hydrofluoric acid (HF), which has both a detrimental effect on the battery performance and poses a hazard risk. Given the reactivity of HF towards silicon oxide, which the optical fibers are constituted of, small amounts of water (100, 500, and 1000 ppm) were added to probe the sensors chemical reactivity and their degree of dissolution into the cell environment. After two weeks of storage, the amount of dissolved silica was determined by means of ICP-OES. Only small amounts of Si were detected, as can be seen from Figure II.8. Assuming uniform fiber dissolution, this only corresponds to the removal of a few atomic layers from the fiber surface. Consequently, it can be concluded that the battery chemical constitution should not affect a FBG sensor sensitivity and response, since the FBG itself is recorded at the fiber core, and there is an average distance of 58.5 μm between the FBG and the optical fiber outer diameter, hence, confirming their suitability to be used in a Li-ion pouch cell environment.

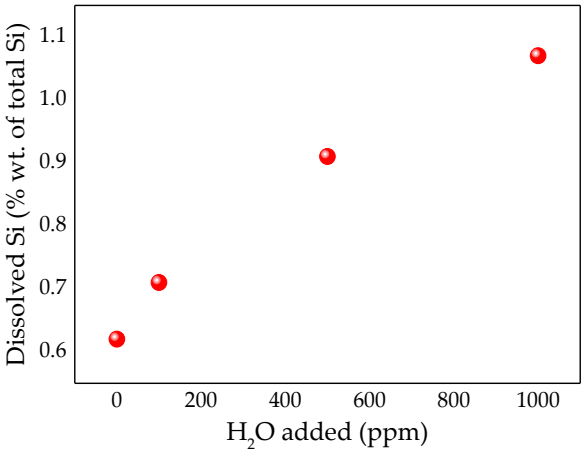

Figure II.8. Amount of Si dissolved from the fiber into the electrolyte after two weeks.

Li-ion pouch cells assembly

The Li-ion pouch cells were assembled using an anode, cathode and an electrolyte solution. All these components and the operation range are shown in Table II.2. All cell assembly operations were carried out inside a dry room (relative humidity < 0.1 % at 20 °C), where all materials were stored prior to usage (Figure II.9).

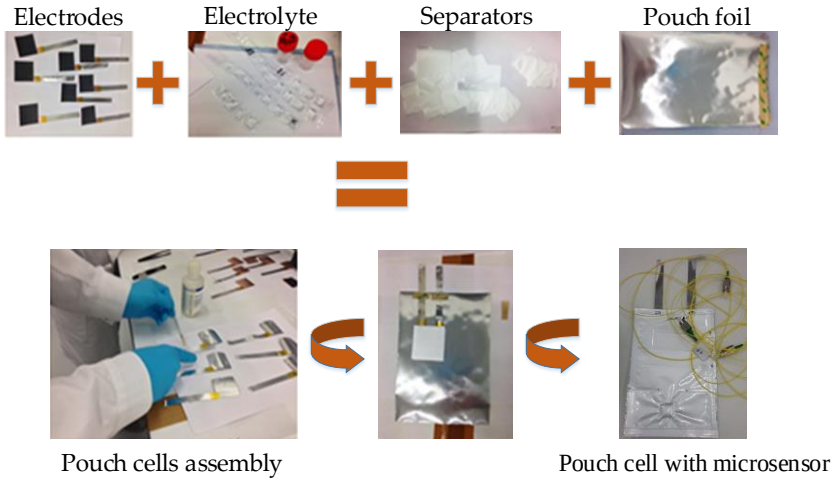

Figure II.9. Experimental procedure for the pouch cells assembly with integrated FBGs.

Table II.2. Chemistry, voltage range, dimensions and capacity at 1 C of the cells.

Chemistry	Cathode Anode Electrolyte	Lithium iron phosphate Graphite LP30 without additives
Voltage Range (V)	Minimum Maximum	2.0 3.8
Dimensions (cm)	Length Width	15.0 12.0
Capacity at 1 C (mAh)	20	

Electrochemical testing

To study the FBG sensors response under different electrochemical inputs, the assembled cells were subjected to a cycling protocol involving a series of different galvanostatic/potentiostatic and open circuit voltage steps.

When varying the external temperature, the FBG response arises due to the inherent thermal expansion of the fiber material and the corresponding temperature dependence of

the refractive index [20]. Through Eq. 1 (previously shown in Chapter 1), the effects of this measurand are accounted for in the Bragg wavelength shift by,

$$\Delta\lambda = 2\lambda_B\left(\frac{1}{n_{eff}}\frac{\partial n_{eff}}{\partial T}+\frac{1}{\Lambda}\frac{\partial \Delta}{\partial T}\right)\Delta T = \lambda_B(\alpha+\xi)\Delta T \quad (1)$$

where α and ξ are the thermal expansion and thermo-optic coefficient of the fiber material, respectively. For a wavelength in the range of 1550 nm, the typical temperature is ~13.0 pm/°C [21]. Figure II.10 shows the results obtained for the cell under study, using the following protocol: 5 CCCV cycles at 1 C, 2 C, 5 C, 8 C, and 1C.

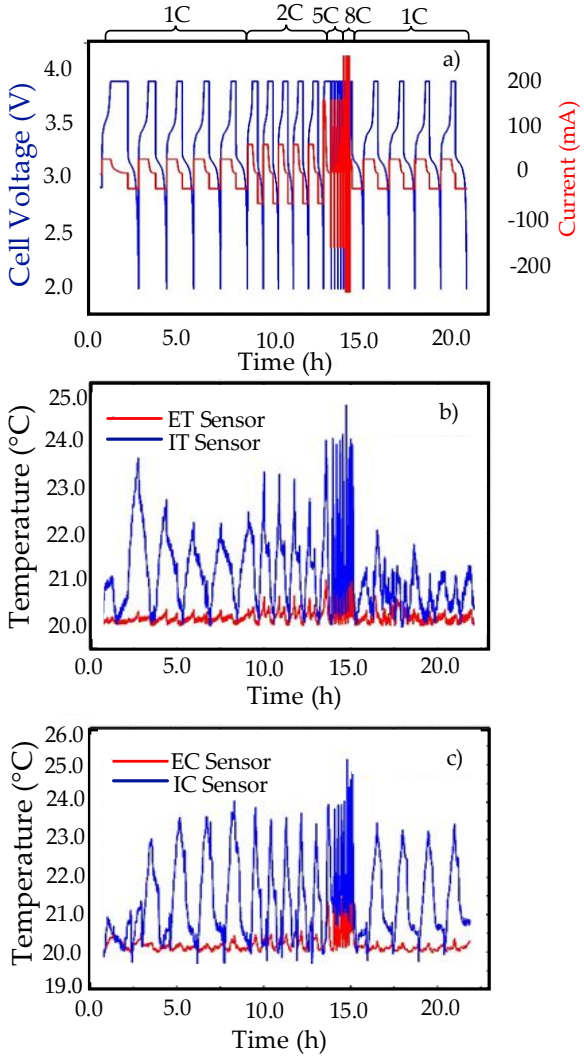

Figure II.10. Temperatures detected by all FBG sensors during the galvanostatic cycling tests.

The cell voltage and current variation are presented on Figure II.10 (a). The temperatures detected, both externally and internally, near the tab and in the center of the

cell are shown in Figure II.10 b) and c), respectively. Comparing the FBG signals, no time delay related to the temperature variations is observed for all sensors, indicating that the sensors response is nearly instantaneous, regardless of their position. The highest temperature variations are, as expected, detected by the internal sensors (IT and IC), larger than their external counterparts (ET and EC) by a factor of 2 to 4. Also, the temperature inside the cell becomes higher as the C-rates increases, as it was expected.

References

20. A. Othonos, *Fiber Bragg gratings*, Review of Scientific Instruments, Vol. 68 (12), pp. 4309-4341, 1997.

21. Y. J. Rao, *Fiber Bragg grating sensors: principles and applications*. In: Grattan K T V, Meggitt. B T, eds. Optical Fiber Sensor Technology, Vol. 2, pp. 355-389, 1998.

III

Lateral load sensing with an optical fiber inline microcavity

Published in IEEE Photonics Technology Letters, Vol. 29, no. 7, September 1, 2017

DOI: 10.1109/LPT.2017.2735021

Lateral load sensing with an optical fiber inline microcavity

Susana Novais, Marta S. Ferreira, João L. Pinto

Abstract: A Fabry-Perot air bubble microcavity fabricated between a section of single mode fiber and a multimode fiber that requires only the use of a commercial fusion splicer is proposed. The study of the microcavities growth with the number of applied arcs is performed and several sensors are tested. The sensors are tested for lateral load measurements, and it is observed that there is dependence between the sensor dimensions and its sensitivity. The maximum sensitivity of 2.11 nm/N was obtained for the 161 μm long cavity. Moreover, given the low temperature sensitivity (<1 pm/°C), the proposed cavity should be adequate to perform temperature independent measurements. The accurate technique control leads to the fabrication of reproducible cavities with the sensitivity required for the application. The way of manufacturing using a standard fusion splicer and given that no oils or etching solutions are involved, emerges as an alternative to the previously developed air bubble based sensors.

Keywords- Optical fibers, Fabry-Perot, microcavities, sensing.

1. Introduction

The first works based on the use of spherical air bubbles as sensing elements were applied for strain sensors [1,2]. The cavities were formed by splicing a standard single-mode fiber (SMF) with an index-guiding photonic crystal fiber. Since then, several works with air bubbles have been presented. These cavities can be fabricated at the fiber tip [3, 4] or inline [5-10]. Several fabrication methods have been proposed in the literature. For instance, the Fabry-Perot (FP) interferometers have been fabricated by fusion splicing a segment of hollow-core photonic bandgap fiber to the SMF [6, 10] or two sections of SMF [5, 8, 9], by ablating a groove in a SMF by use of a femtosecond laser [7], by the catastrophic fuse effect [11], and by applying chemical etching [4].

Lateral load sensing has been done with different configurations [4, 12-16]. Compared with the strain sensing, the lateral load is applied in the direction perpendicular to the fiber longitudinal axis. In the last years, lateral load sensing has been realized by using fiber Bragg gratings [12] or long period gratings [17], and more recently with FP

microcavities fabricated at the fiber tip [4, 16].

In the present work, the development of a FP air cavity made by splicing a section of single mode fiber and multimode fiber is proposed. The sensor is employed for lateral load measurements. It is observed that there is a dependence between the sensor dimensions and its sensitivity. Besides, given the low temperature sensitivity, the proposed cavity can be a good candidate to perform temperature independent measurements.

2. Sensor microfabrication

The Fabry-Perot (FP) cavities developed in this work were obtained by producing an air bubble between a section of single mode fiber (SMF 28e) and multimode fiber (MMF GIF625). The procedure used to fabricate the sensing devices is shown in Figure III.1. Initially the two fibers were placed in the splicing machine (Fujikura 62S) and aligned using the manual mode (Figure III.1a). The parameters were set to an arc power of 20 arb. units, and the arc duration was 700 ms. The SMF was removed and an arc discharge was applied to the MMF tip (Figure III.1b). The electrical discharge high power was transferred to the MMF tip, causing a partial melting. As a result of the surface tension, the fiber acquired a round shape (Figure III.1c). The parameters of the splicing machine were then changed to an arc power of 10 arb. units and the duration was 400 ms. Both fibers were aligned once again and a small amount of compression was applied between them (Figure III.1d). After one arc, the energy transferred to the fiber tips will cause their melting and, as the temperature in the fibers outer region decreases faster than on the inside, some air is trapped, forming a microbubble [5]. The microcavity volume can be increased by applying successive electrical arcs, using the same parameters. The microscope photograph of one of the cavities produced is shown in Figure III.1e).

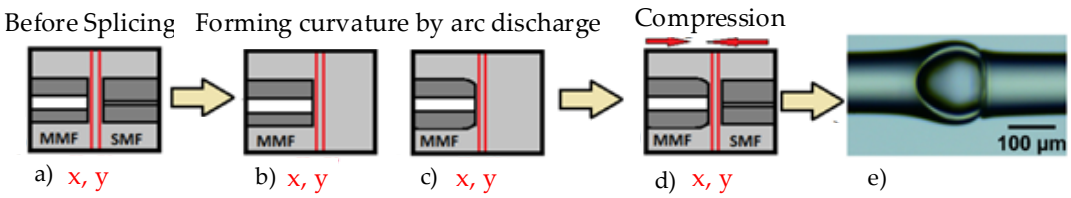

Figure III.1. Schematic of the procedures used to fabricate the FP cavity.

Using this technique several devices were fabricated, with cavity lengths that ranged from ~50 µm up to ~200 µm. The air FP cavities growth with the increase of the number of arcs is shown Figure III.2. With the successive electrical arcs, it can be observed that the cavity tends to grow into the MMF side, whereas SMF surface preserves a flat surface. The parameters used to produce the microcavities were found empirically. However, once they were set, it was possible to reproduce the sensors and fabricate them with the desired dimensions. By changing the parameters, similarly shaped cavities with different dimensions can also be fabricated.

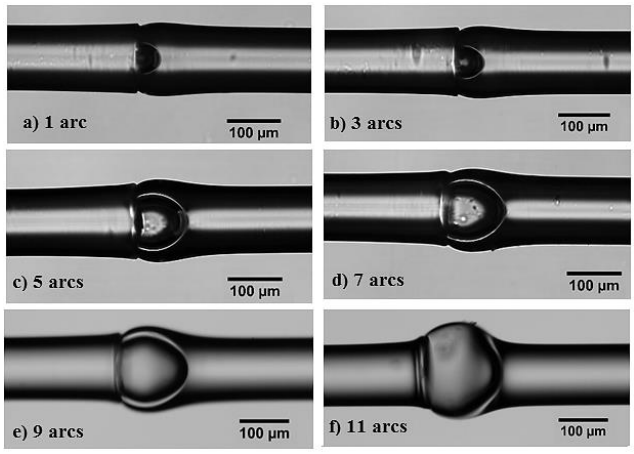

Figure III.2. Microscope photographs of the sensing structure after the fabrication process, with increasing number of arc discharges.

The microcavities diameter, corresponding to the FP length, was measured after each electric-arc discharge and depicted in Figure III.3. There is stronger growth at the beginning of the fabrication (first five arc discharges). After that point the microcavities growth tends to stabilize, as can be seen in Figure III.3. A final diameter of ~160 µm was attained, after 11 electric arc discharges. Above this value, the microcavities thickness became very thin (Figure III.2f), damaging the sensors. In the inset of Figure III.3, it was

observed that the insertion loss increases with the increase of the number of electrical arcs, and consequently with the cavity length. The insertion loss values shown were measured in transmission at 1550 nm for each electric arc applied.

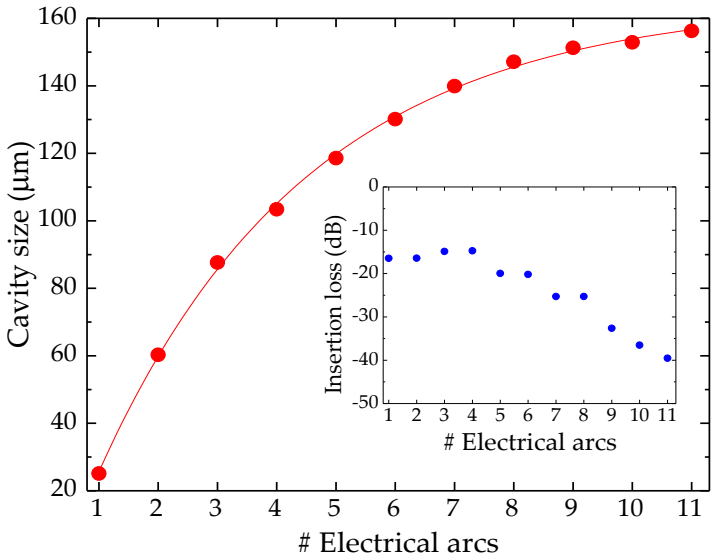

Figure III.3. Dependence of the cavity size and insertion losses at 1550 nm (inset) with the number of electric arcs.

3. Experimental results

The spectral response of this sensing structure was observed by connecting it to an optical circulator[6]. A broadband optical source (bandwidth of 80 nm, centered at 1570 nm), and an optical spectrum analyzer (OSA Anritsu MS9740A) were connected to the other two ports of this optical component, in a typical reflection scheme, as shown in Figure III. 4. The readings were done with a resolution of 0.2 nm.

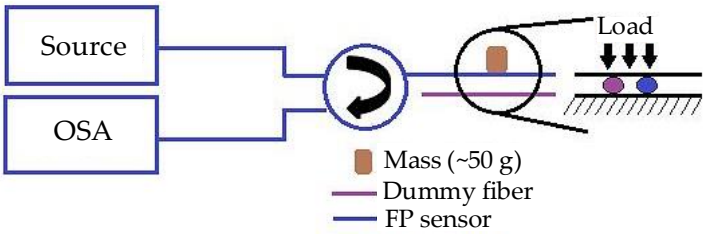

Figure III.4. Scheme of the experimental setup with a zoom of the cross-section view.

[6] Please see the Additional Information Section at the end of this Chapter for more results.

The reflection spectra of the first 5 cavities are shown in Figure III.5 and can be approximated to a two-wave interferometer. The subtraction of the wavelengths of two adjacent peaks, $\Delta\lambda=\lambda_2-\lambda_1$, corresponds to the free spectral range (FSR). This parameter is related to the length of the cavity, L_{FP}, through the Eq. $\Delta\lambda = \lambda_1\lambda_2/(2n_{eff}L_{FP})$, where it was considered that the effective refractive index, n_{eff} (λ), was constant. The length of each sensing device was measured through the microscope photographs, whereas the two adjacent peak wavelengths were obtained from the sensing heads spectral response. Thus, from this relationship it is possible to estimate the n_{eff} inside the cavity to be 1.00.

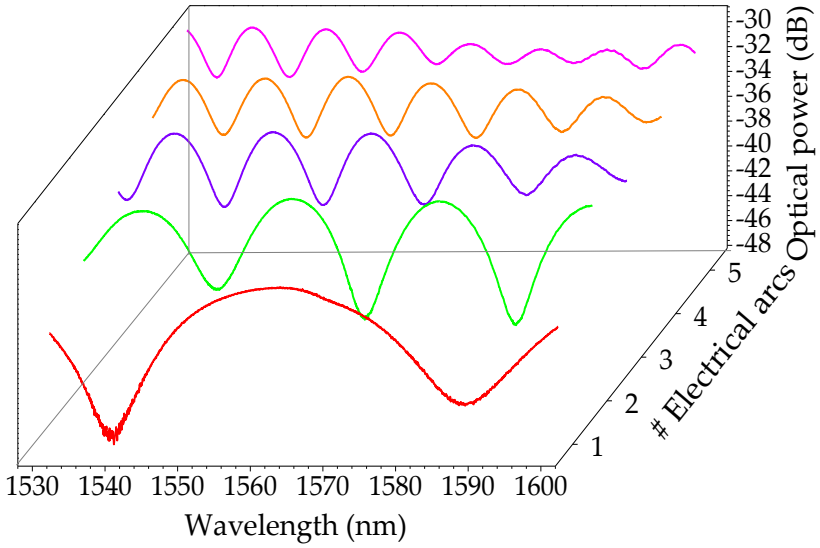

Figure III.5. Spectral response of FP cavity with different number of electrical arcs.

As the number of electrical arcs increases (until 9) the signal visibility diminishes (Figure III.6). However, for 10 electrical arcs this parameter increases once again, and for 11 discharges, the increase is even more significant. This can be due to the fact that the interface air/MMF changes as the cavity expands. For the first 9 arcs the interface presents a curvature increase and the diffraction effects are significant. After that value, the interface becomes more flat, diminishing the light diffraction and improving the quality of the mirrors.

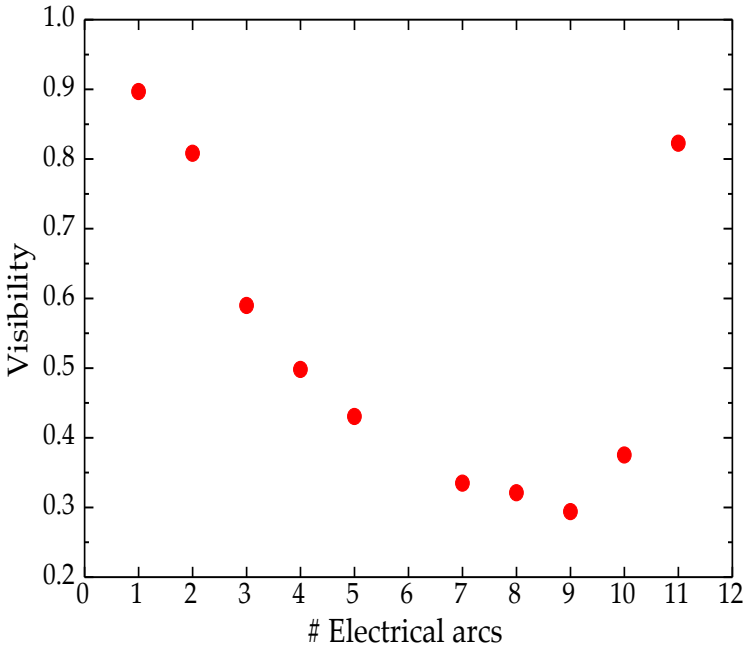

Figure III.6. Spectral response of visibility with different number of electrical arcs.

The lateral load measurements were carried out by placing the sensor in flat platform, so that the stress was applied evenly throughout the structure. As shown in the Figure III.4, a dummy fiber was placed parallel to the sensor (~1 cm apart) to provide full leveling as the weights were placed on top of the sensor. Cylindrical weights of ~50 g and a base diameter of 2.0 cm were sequentially positioned on top of the sensor, translating into a lateral load ranging from 0.0 N to ~4.0 N. Due to experimental constraints, it was not possible to estimate the maximum loading of the sensors. This is still a matter under study. Lateral load tests were carried out in several sensors, whose cavities dimensions ranged from 47 μm up to 161 μm, using the experimental setup depicted in Figure III.4.

The sensors response towards this parameter is shown in Figure III.7. It can be seen that there is a wavelength shift towards longer wavelengths, for all sensors. The experimental data was well adjusted for a linear function (with a correlation factor higher than 0.99). All the experiments were performed several times and by considering both the increase and decrease of lateral load. There was good reproducibility of the results, evidencing the reversibility of the structure.

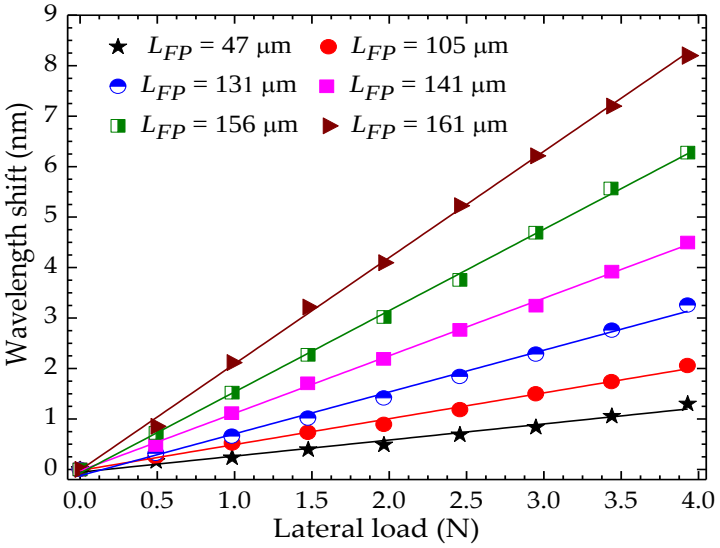

Figure III.7. Sensors response to the applied lateral load.

From these results, there appears to be a relationship between the cavity size and the lateral load sensitivity (Figure III.8). In fact, the longer the cavity, the higher the sensitivity is. This behavior occurs due to the larger volume of the cavity, a parameter that plays an important role in air bubble based FP cavities [10]. A minimum sensitivity to the lateral load of the 0.32 nm/N was obtained, for the smallest cavity manufactured (47 µm), whereas a maximum sensitivity of the 2.11 nm/N was obtained for the largest cavity (161 µm). A resolution of ~0.1 N was estimated, considering the sensor with the highest sensitivity, and taking into account that the readings resolution. The dependence between the sensitivity and sensors size presents a nonlinear response as shown in Figure III.8.

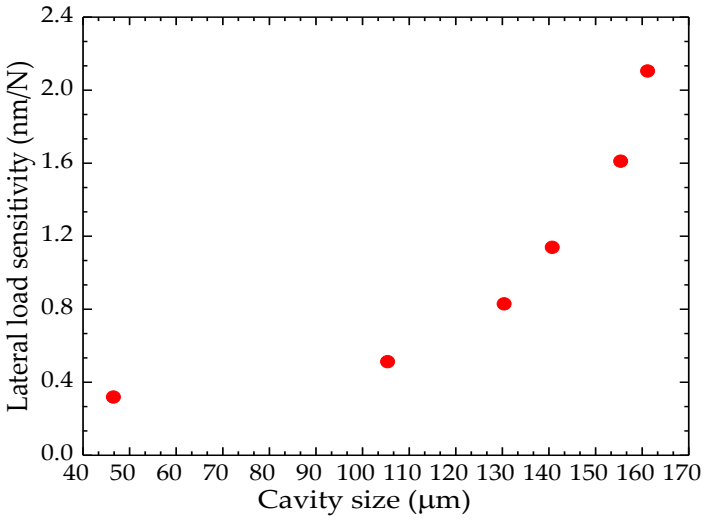

Figure III.8. Relation between cavity size and lateral load sensitivity.

Compared with the fiber Bragg grating or long period grating based lateral load sensors that typically have a lateral load sensitivity of 2.93×10^{-2} nm/N [15] and 1.02 nm/N [17], respectively, the microcavity lateral load sensor shows a higher sensitivity of 2.11 nm/N. To the best of our knowledge, this is the highest lateral load sensitivity reported for inline sensors.

During the experiments, it was observed that the air bubbles were not fully symmetric (see the inset Figure III.9), which means that the thickness of the silica walls is not constant. This feature comes as a consequence of the manufacturing process and so far it is not fully controllable. This is still a matter under study.

Depending on the position of the sensor, the mass will be exerting load in a region that may have more or less silica, resulting in variation of the sensor sensitivity. In Figure III.9, the 131 μm sensor response to lateral load is shown. Two different positions were considered by slightly turning the fiber, under a 5× magnifying lens. The fiber was kept straight, without tension or distortion. A sensitivity enhancement from 0.83 nm/N (solid red dots) to 1.01 nm/N (open black dots) was determined.

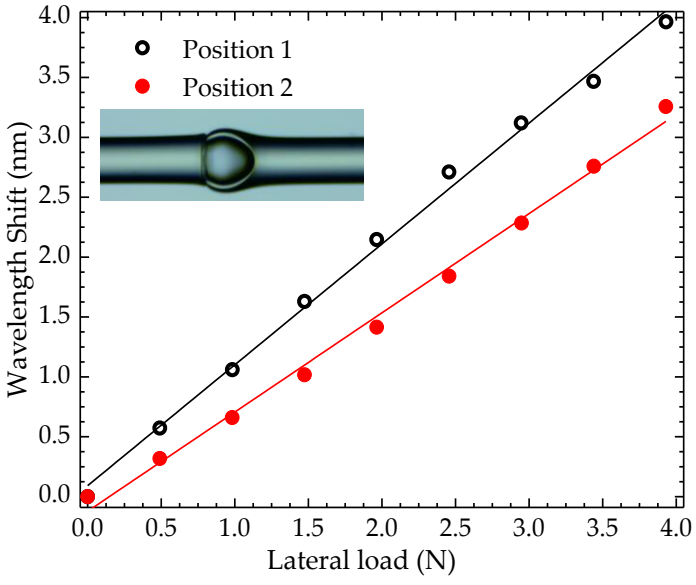

Figure III.9. Response of the 131 μm long sensor to lateral load considering two different positions.

The temperature response of the 131 μm long microcavity sensor was measured by using a thermal chamber (Model 340, Challenge Angelantoni Industry) and the

wavelength variations were monitored using the same interrogation scheme as shown in Figure III.4. The temperature was raised in steps of 10 °C, from 0 °C until 100 °C, and maintained for about 30 min at each step to make sure that the temperature in the thermal chamber had stabilized. The same process for the cooling was followed. The sensor response to the temperature variations is shown in Figure III.10. The proposed sensor exhibited very low thermal dependence (< 1 pm/°C), which is in good agreement with the results found in the literature for air cavities inside an optical fiber [10]. In principle, with this sensing device there is no need to perform temperature compensation, as the cross-sensitivity between this parameter and lateral load was lower than 3.14×10^{-3} N/°C.

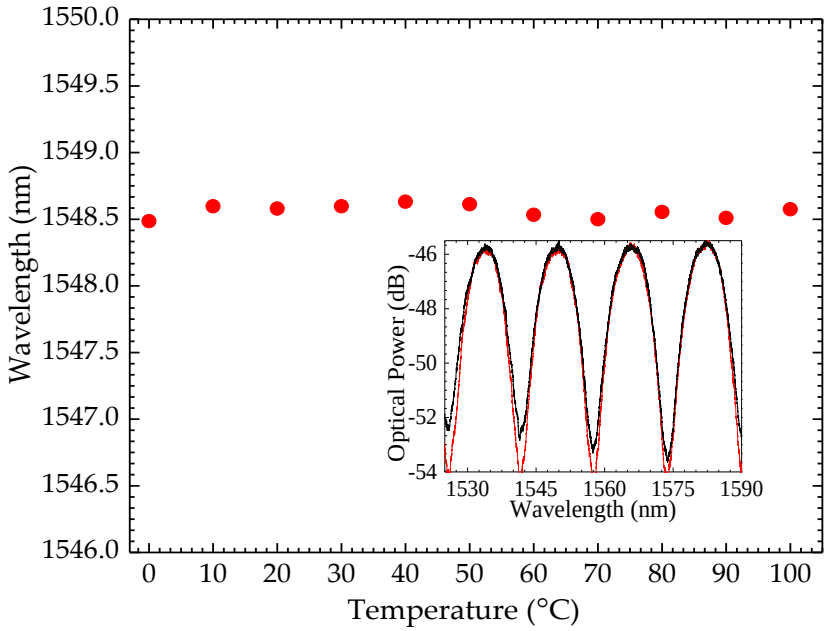

Figure III.10. Response of the 131 μm long sensor to temperature.

4. Conclusions

In summary, a microcavity sensor was fabricated by using the electric arc discharge technique to create an air bubble between a section of single mode fiber and multimode fiber. It was observed that with the increasing number of arcs both the cavity length and volume increase, which also has influence on the sensitivity to lateral load. Larger cavities exhibit higher sensitivities. The sensor with a smaller cavity length presented a sensitivity of 0.32 nm/N, for loads ranging from 0.0 N to 4.0 N, whereas the sensor with a higher

cavity length achieved a maximum sensitivity of 2.11 nm/N. Besides, given the low temperature sensitivity (< 1 pm/°C), the proposed cavity can be a good candidate to perform temperature independent measurements. To the best of our knowledge, the obtained sensitivity is higher than the reported in the literature, for inline reflection fiber sensors. This way of manufacturing the sensors using only standard single mode and multimode fibers, a fusion splicer and given that no liquids, oils or etching solutions are involved, emerges as an alternative to the previously developed air bubble based sensors.

Acknowledgments: This work was supported in part by the European Project Stable Interfaces for Rechargeable Batteries (FP7-ENERGY-2013) under Grant 608502 and in part by FEDER funds through the COMPETE 2020 Programme and National Funds through FCT–Portuguese Foundation for Science and Technology under Project UID/CTM/50025/2013. The work of S. Novais was supported by Research Fellowship BI/UI96/6643/2016. The work of M. S. Ferreira was supported by Research Fellowship BPD/UI96/7331/2016.

References

1. J. Villatoro, V. Finazzi, G. Coviello, and V. Pruneri, "Photonic-crystal-fiber-enabled micro-Fabry-Perot interferometer," Opt. Lett., Vol. 34, no. 16, pp. 2441-2443, 2009.

2. E. Li, G. D. Peng, and X. Ding, "High spatial resolution fiber-optic Fizeau interferometric strain sensor based on an in-fiber spherical microcavity," Appl. Phys. Lett., Vol. 92, pp. 101117, 2008.

3. C. Liao, S. Liu, L. Xu, C. Wang, Y. Wang, Z. Li, Q. Wang, and D. N. Wang, "Sub-micron silica diaphragm- based fiber-tip Fabry-Perot interferometer for pressure measurement," Opt. Lett., Vol. 39, no. 10, pp. 2827-2830, 2014.

4. X. Jiang and D. Chen, "Low-cost fiber-tip Fabry-Perot interferometer and its application for transverse load sensing," Progress in Electromagnetics Research Lett., Vol. 48, pp. 103-108, 2014.

5. D. W. Duan, Y. J. Rao, Y. S. Hou, and T. Zhu, "Microbubble based fiber-optic Fabry-Perot interferometer formed by fusion splicing single-mode fibers for strain measurement," Appl. Optics., Vol. 51, no. 8, pp. 1033-1036, 2012.

6. M. Deng, C. P, Tang, T. Zhu, and Y. J. Rao, "PCF- based Fabry-Perot interferometric sensor for strain measurement at high temperatures," IEEE Photonic .Tech. L., Vol. 23, no. 11, pp. 700-702, 2011.

7. Y. Liu, S. Qu, W. Qu, R. Que, "A Fabry-Perot cuboid cavity across the fibre for high-sensitivity strain force sensing," J. Opt. Vol. 16, pp. 105401, 2014.

8. S. Liu, K. Yang, Y. Wang, J. Qu, C. Liao, J. He, Z. Li, G. Yin, B. Sun, J. Zhou, G. Wang, J. Tang, and J. Zhao, "High-sensitivity strain sensor based on in-fiber rectangular air bubble," Sci. Reports., Vol. 5, pp. 7624, 2015.

9. S. Liu, Y. Wang, C. Liao, G. Wang, Z. Li, Q. Wang, J. Zhou, K. Yang, X. Zhong, J. Zhao, and J. Tang, "High-sensitivity strain sensor based on in-fiber improved Fabry-Perot interferometer," Opt. Lett., Vol. 39, no. 7, pp. 2121-2124, 2014.

10. F. C. Favero, L. Araujo, G. Bouwmans, V. Finazzi, J. Villatoro, and V. Pruneri, "Spheroidal Fabry-Perot microcavities in optical fibers for high-sensitivity sensing," Opt. Express., Vol. 20, no. 7, pp. 7112-7118, 2012.

11. M. F. Domingues, T. B. Paixão, E.F.T. Mesquita, N. Alberto, A. R.Frias, R. A. S. Ferreira, H. Varum, P. F. C. Antunes, P. S. B. André, "Liquid Hydrostatic pressure optical sensor based on micro-cavity produced by the catastrophic fuse effect", IEEE Sensors Journal., Vol. 15, no. 10, pp. 5654-5658, 2015.

12. T. Geernaert, G. Luyckx, E. Voet, T. Nasilowski, K. Chah, M.Becker, H. Bartelt, W. Urbanczyk, J. Wojcik, W. Waele, J. Degrieck, H. Terryn, F. Berghmans, and H. Thienpont, "Transversal load sensing with fiber Bragg gratings in oicrostructured Optical Fibers," IEEE Photonic. Tech. L., Vol. 21 no. 1, pp. 6-8, 2009.

13. C. Jewart, K. P. Chen, B. McMillen, M. M. Bails, and S. P. Levitan, "Sensitivity enhancement of fiber Bragg gratings to transverse stress by using microstructural fibers," Opt. Lett. Vol. 31, no. 15, 2260-2262, 2006.

14. H. Chi, X. M. Tao, and D. X. Yang, "Simultaneous measurement of axial strain, temperature, and transverse load by a superstructure fiber grating," Opt. Lett., Vol. 26, no. 24, pp. 1949-1951, 2001.

15. R. Correia, E. Chechura, J. Li, S.W. James and R. P. Tatam, " Enhanced sensivity fibre Bragg grating (FBG) load sensor," Meas. Sci. Tech., Vol. 21, pp. 1-7, 2010.

16. J. Ma, J. Ju, L. Jin, W. Jin, and D. Wang "Fiber-tip micro-cavity for temperature and transverse load sensing," Opt. Express., Vol. 19, no. 13, pp. 2-9,2011.

17. Y. Liu, L. Zhang, and I. Bennion, "Fibre optic load sensors with high transverse strain sensitivity based on long-period gratings in B/Ge co-doped fibre," Electron. Lett., Vol. 35, no.8, pp. 661-663, 1999.

IIIA - Additional Information

The sensor described in this Chapter was developed to be integrated in Li-ion batteries, in the framework of the European Project SIRBATT. The final goal was to obtain a hybrid structure, by inscribing a fiber Bragg grating close to the FP cavity and therefore, to be able to discriminate strain and temperature.

To complement the results previously discussed, the sensors were also used to measure strain. The results from this study were published in the Proceedings of SPIE 10453, *3rd International Conference on Applications of Optics and Photonics*, DOI: 10.1117/12.2276342.

Experimental Results

The spectral response of this sensing structure was observed by connecting it to an optical circulator. A broadband optical source (bandwidth of 80 nm, centered at 1570 nm), and an optical spectrum analyzer (OSA Anritsu MS9740A) were connected to the other two ports of this optical component, in a typical reflection scheme, as shown in Figure III.11. The readings were done with a resolution of 0.2 nm. Figure III.11 present experimental setup for strain sensing.

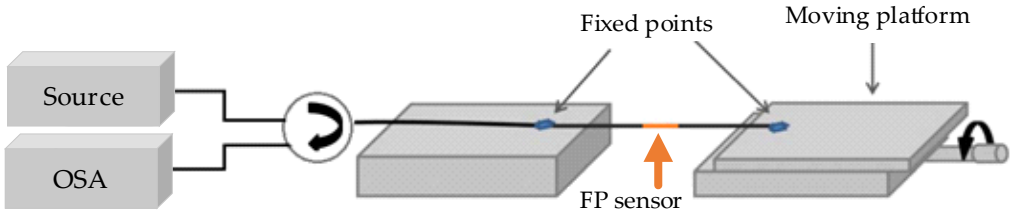

Figure III.11. Scheme of the experimental setup for strain measurements.

To characterize the strain sensors sensitivity, a translation stage was used. The sensors were fixed between a rigid fixed support and the translation stage as shown in Figure III.11. The data acquisition system was the same used for the lateral load tests already explained. The sensor reflection spectrum was obtained for each sensor, as

function of the imposed elongation. In Figure III.12a), it can be seen that there is a wavelength shift towards longer wavelengths for all sensors. The experimental data was well adjusted to a linear function (with a correlation factor higher than 0.99).

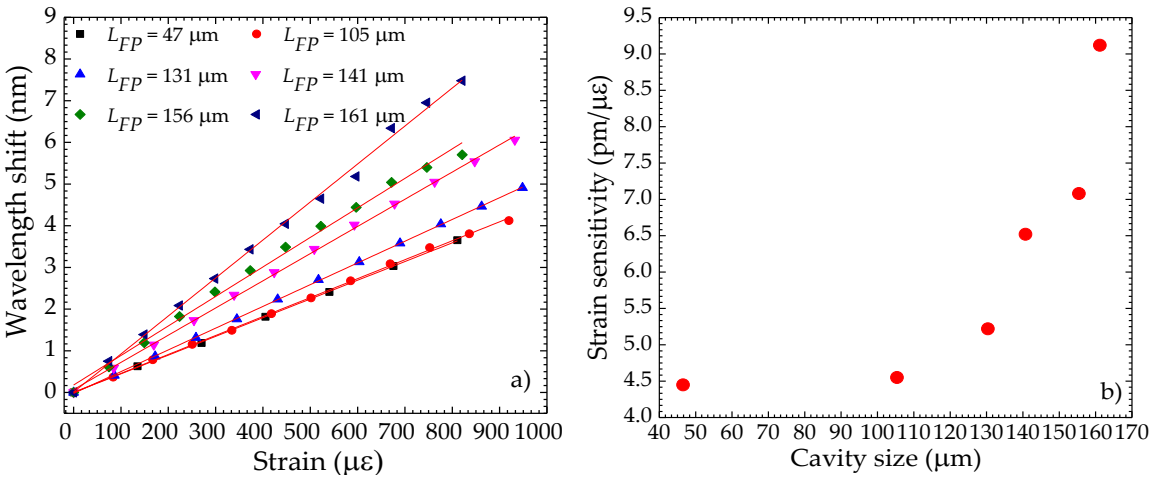

Figure III.12. Sensors response to the applied strain (a) and relation between cavity size and strain sensitivity (b).

The sensors response to strain also exhibited a dependence on the cavities dimension, as shown in Figure III.12b). A minimum sensitivity of 4.49 pm/με was obtained, for the smallest cavity manufactured (47 μm), whereas the maximum sensitivity of the 9.12 pm/με, was obtained for the largest cavity (161 μm). Note that the microcavity radial dimension is much higher than the optical fiber core diameter, implying that a large number of transversal optical modes are allowed. Moreover, due to the limited size of the fiber diameter, when compared to the cavity width, a strain applied along the fiber longitudinal axis also imposes a reduction of the cavity width.

IV

Optical fiber Fabry-Perot tip sensor for detection of water-glycerin mixtures

Published in Journal of Lightwave Technology, Vol. 36, no.9, May 1, 2018

DOI: 10.1109/JLT.2017.2784540

Optical fiber Fabry-Perot tip sensor for detection of water-glycerin mixtures

Susana Novais, Marta S. Ferreira, João L. Pinto

Abstract: A fiber sensor based on a Fabry-Perot cavity is reported for measuring mixtures of water and glycerin. The sensor is fabricated by producing an air bubble near the end face of a multimode fiber section, and reshaping the tip in order to produce a thin silica diaphragm. It is observed that there is dependence between diaphragm dimensions and the structure sensitivity. The sensor with a 20 μm thick diaphragm presents a sensitivity of 7.81 pm/wt.% regarding the variation of water mass fraction in glycerin. With this sensing head, an experimental resolution of 2.5 wt.% is estimated. By converting the mass fraction into refractive index variations, a maximum sensitivity of 5.49 nm/RIU is obtained. Moreover, given the low temperature sensitivity (1.6 pm/°C), the proposed cavity should be adequate to perform temperature independent measurements. The purity degree of glycerin is one of the most important parameters to be determined in applications such as in pharmaceutical or cosmetic area. The proposed sensor can be an alternative to the previously developed ones.

Keywords- Fiber optics sensors, Fabry-Perot interferometer, graded-index fiber, glycerin-water mixtures.

1. Introduction

The water-cosolvent mixtures have been broadly used in pharmaceutical industry in order to enhance the solubility of drugs scarcely soluble in water during the plan of homogeneous pharmaceutical dosage forms, such as elixirs and syrups, suppositories, anesthetics, antibiotics and antiseptics [1]. Ethanol and glycerin are two of the cosolvents used nowadays, intended for elaboration of peroral and parenteral medications and as an evaporation regulator in several formulations [2]. The increase of the interactions between unlike molecules and the large differences in molar volumes of the pure components lead to non-additive volumes on mixing. In this way, the mixtures obtained using these cosolvents and water show highly non-ideal behaviors [3, 4]. Thus, it is essential to characterize the volumetric behavior of such binary mixtures in order to extend all

physicochemical information as well as to understand the intermolecular interactions present in cosmetic and pharmaceutical liquid systems [1].

The degree of purity of crude glycerin from biodiesel can only be achieved through complex and costly processes such as distillation and, in the case of glycerin, from the transesterification of waste oils and fats. The process is technically complex and its economic viability needs to be very well evaluated [5]. Therefore, it is of utmost importance to find sensing solutions that can bring accurate information in real-time, during the purification process. In the last years, several optical fiber sensors were reported in the literature, where glycerin-water mixtures were realized to induce the environmental refractive index variations. Usually, the sensors response in terms of mass fraction it is not addressed a valuable information in practical applications.

For instance, a Mach-Zehnder interferometer based on a photonic crystal fiber section coated with hafnium oxide was reported [6]. The simultaneous measurement of refractive index and temperature using a multimode-singlemode-multimode structure coated with polydimethylsiloxane and gold was proposed [7]. A different configuration was proposed by Qi *et al*., based on a highly reflective long period fiber grating located near the fiber tip, which was coated with a layer of silver and quartz [8]. The Fabry-Perot (FP) based interferometers were also explored for the measurement refractive index based on glycerin-water mixtures. For example, the proposed sensors were obtained by splicing a section of suspended hollow core fiber with a single mode fiber (SMF) [9], or by selectively etching a special designed fiber, which was spliced between a SMF and a coreless fiber [10].

Spherical air bubbles produced inside the optical fiber and used as sensing elements were firstly proposed for strain sensing [11]. Over the last years, this type of configuration has been subject of extensive research. These FP cavities were mainly applied in strain and temperature sensing, and astonishing sensitivities were reported [12-17]. Regarding refractive index sensing, it was proposed by using a hollow core fiber ended with a hollow core silica sphere tip [18]. On the other hand, a biconically tapered fiber concatenated to an air bubble based FP was also presented [19]. Recently, a FP fiber tip

sensor based on an inner air-cavity produced between a section of SMF and hollow core photonic crystal fiber (HC PCF) has been proposed [20].

In this work, a fiber sensor based on a Fabry-Perot cavity is reported for measuring water-glycerin mixtures. The sensors fabrication method is an adaptation of the one described in [21], where the bubble was obtained between a SMF and MMF fiber section. Here, only MMF is used and the sensing head is fabricated at the fiber tip. The structure is robust and easy to manufacture. When the sensing head is placed in a liquid medium, the visibility of the reflected signal diminishes, causing a variation in the phase of the optical signal, which becomes sensitive to variations of the external medium. Furthermore, the structure is also characterized for temperature variations.

2. Principle of operation and simulation

The schematic diagram of the fiber tip Fabry-Perot (FP) sensor developed in this work is shown in Figure IV.1. The sensing head was obtained by producing an air bubble near the tip of a multimode fiber, which was then reshaped to create a thin silica diaphragm. The proposed device contains three reflection mirrors, M_1, M_2, and M_3, respectively, as shown in Figure IV.1, which form three cavities. The first cavity, with a physical length L_1, results from the reflections occurring between M_1 and M_2. The second cavity, with a length L_2, corresponds to the diaphragm formed between M_2 and the MMF end face, M_3. The third cavity results from the conjunction of the two previous cavities, being its length of $L_1 + L_2$.

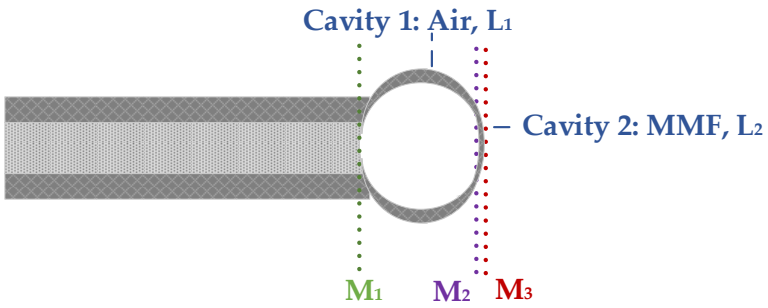

Figure IV.1. Scheme of the fiber tip FP sensor, where the M_1, M_2, M_3 are the sensors mirrors. L_1 and L_2 are the lengths of cavity 1 and 2, respectively.

The reflection coefficients at each interface, R_1, R_2, and R_3, are given by:

$$R_1 = R_2 = \left(\frac{n_{MMF} - n_{air}}{n_{MMF} + n_{air}} \right)^2, \quad R_3 = \left(\frac{n_{MMF} - n_s}{n_{MMF} + n_s} \right)^2, \tag{1}$$

where n_{MMF}, n_{air}, and n_s are the refractive indices of the multimode fiber, the air cavity, and the surrounding medium, respectively. The total reflected electric field at the detector, E_r, is given approximately by the sum of all the reflected electric fields from the three surfaces. Given the low reflectivity of the reflective surfaces, the sensor can be simplified as a low-finesse FPI and E_r can be derived as follows [22]:

$$E_r = E_0 \left[\sqrt{R_1} + (1-\alpha_1)(1-R_1)\sqrt{R_2} e^{-j\varphi_1 + j\pi} + (1-\alpha_1)(1-\alpha_2)(1-R_1)(1-R_2)\sqrt{R_3} e^{-j(\varphi_1+\varphi_2)} \right], \tag{2}$$

where E_0 is the input field, whereas α_1 and α_2 are the transmission loss factors due to the mode mismatching and surface imperfections at M_1 and M_2, respectively. ϕ_1 and ϕ_2 are the phase shifts in the cavity given by:

$$\phi_1 = \frac{4\pi n_{air} L_{FP}}{\lambda}, \ \phi_2 = \frac{4\pi n_{MMF} L_2}{\lambda}, \tag{3}$$

where L_{FP} corresponds to the high frequency signal cavity length, L_2 is the cavity length of the low frequency signal. For simplicity, the spherical shape of the cavity was not taken into consideration in this simulation. The π-phase shift introduced in Eq. 2 is originated at M_2, where the reflection occurs at a medium with higher refractive index. Furthermore, it was considered the situation where $n_s < n_{MMF}$.

From Eq. 2, the total reflective intensity can be described by the intensity ratio of the reflected electric field to the incident electric field:

$$\begin{aligned} I_{Rtotal}(\lambda) = \left| \frac{E_r}{E_0} \right|^2 &= R_1 + (1-\alpha_1)^2 (1-R_1)^2 R_2 \\ &+ (1-\alpha_1)^2 (1-\alpha_2)^2 (1-R_1)^2 (1-R_2)^2 R_3 \\ &+ 2\sqrt{R_1 R_3} (1-\alpha_1)(1-\alpha_2)(1-R_1)(1-R_2)\cos(\phi_1 + \phi_2) \\ &- 2\sqrt{R_2 R_3} (1-\alpha_1)^2 (1-\alpha_2)(1-R_1)^2 (1-R_2)\cos(2\phi_1 + \phi_2) \\ &- 2\sqrt{R_1 R_2} (1-\alpha_1)(1-R_1)\cos(\phi_1) \end{aligned} \tag{4}$$

The simulated spectra for air, water, and glycerin shown in Figure IV.2 were obtained by using (4) and considering the following parameters: n_{air} = 1.000 RIU, n_{MMF} = 1.513 RIU, n_{water} = 1.3154 RIU, $n_{glycerin}$ = 1.4571 RIU, L_1 = 147 μm, L_2 = 20.1 μm, α_1 = 0.5 and α_2 = 0.7.

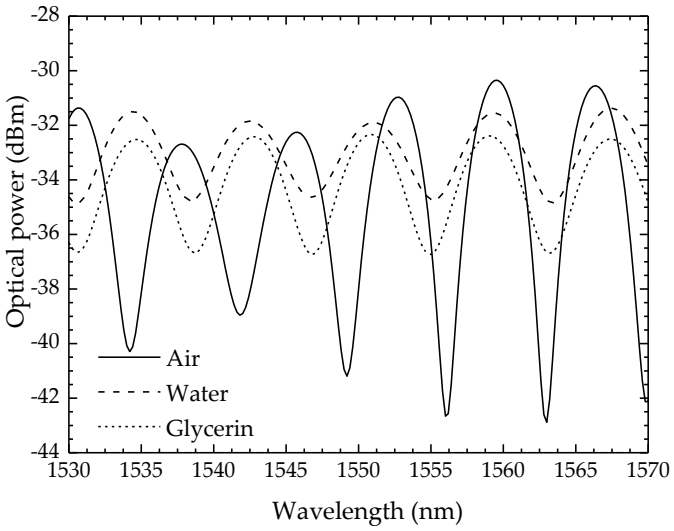

Figure IV.2. Simulated spectra for three different surrounding media (air, water, and glycerin).

When the sensor is surrounded by air, the reflection coefficients are the same at the three interfaces. According to the experimental observation, the interferometric behavior was essentially determined by the reflections occurring at M_1 and M_3. Thus, in this case, the length considered in the simulations was $L_{FP} = L_1 + L_2$. However, when the sensor is submerged in a liquid, R_3 diminishes and the amplitude of the wave reflected at M_3 is reduced, which indicates that the reflection at M_2, whose coefficient of reflection has remained unaltered, becomes dominant. The larger the surrounding medium refractive index, the more pronounced is this reduction in amplitude [23]. The combination between the two waves reflected at M_2 and M_3 leads to a variation not only in the spectrum visibility, but also in wavelength [24]. In this case, the simulations were performed considering that $L_{FP} = L_1$.

3. Mass fraction and refractive index relationship

The variation of mass fraction in a mixture of water and glycerin translates in a change of the medium refractive index. This parameter was determined for all the

solutions tested in this work, using an Abbe refractometer (Krüss optronic refractometer). This equipment provides information in the spectral visible range (λ = 589 nm). However, the sensing device used during the experiments operated in the 1550 nm region. Therefore, it was necessary to consider the refractive index at this wavelength range. Saunders *et al.* reported on the near-infrared refractive indices of common solvents [25]. Through the third order polynomial function present in Eq. 5, and using the parameters *A*, *B*, *C*, and *D* shown in Table IV.1, it was possible obtain the numerical values for refractive index at 1550 nm, for the different weight fractions, ω, considered in this work.

$$n(\omega) = A\omega^3 + B\omega^2 + C\omega + D\,, \tag{5}$$

Figure IV.3 presents the refractive index dependence on the mass fraction, where 0 corresponds to a solution of 100 % glycerin and 1 is relative to 100 % water. Both the experimental and numerical values at 589 nm and 1550 nm, respectively, are shown in the Figure IV.3. Notice that the behavior is similar in both cases. The experimental data was also fitted to a third order polynomial, whose parameters can be found in Table IV.1.

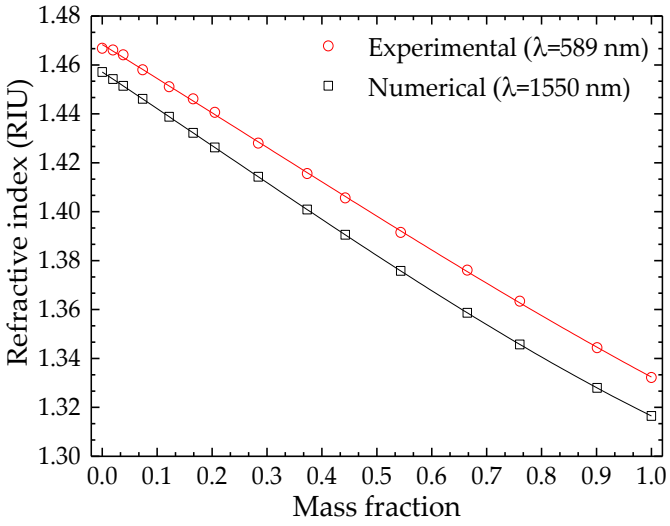

Figure IV.3. Refractive index dependence on mass fraction, for two different wavelengths: 589 nm (experimental data) and 1550 nm (numerical values [25]).

Table IV.1. Polynomial fitting parameters of n @ 589 nm (experimental) and n @ 1550 nm (numerical [25]).

	λ = 589 nm	λ = 1550 nm
A	0.0139	0.0216
B	-0.0121	-0.0136
C	-0.1377	-0.1486
D	1.4683	1.4571

4. Sensor fabrication

The FP cavities developed in this work were obtained by producing an air bubble at the tip of a multimode fiber (MMF) section (GIF625). The procedure used to fabricate the sensing devices is shown in Figure IV.4.

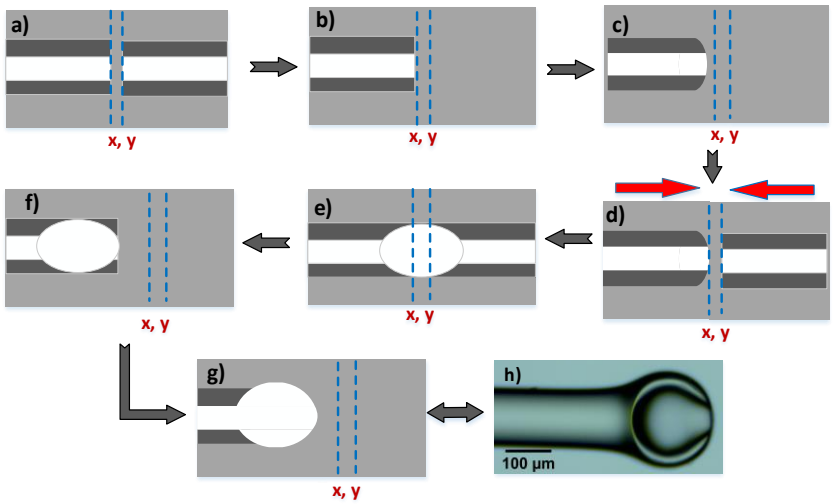

Figure IV.4. Scheme of the optical fiber tip fabrication steps.

Initially, the two MMFs were placed in the splicing machine (Fujikura 40S) and aligned using the manual mode (Figure IV.4a). The parameters, found empirically, were set to an arc power of 20 arb. units, and an arc duration of 700 ms. One of the fibers was removed and an arc discharge was applied to the remaining MMF tip (Figure IV.4b). The high power of the electrical discharge was transferred to the fiber tip, causing a partial melting. As a result of the surface tension, it acquired a round shape (Figure IV.4c). The parameters of the fusion splicer were then changed to an arc power of 10 arb. units and

duration of 400 ms. Both fibers were aligned once again and a small amount of compression was applied between them (Figure IV.4d). This compression was produced manually by moving the fiber holders towards each other. Even though this step is currently not fully controlled, efforts are being made to develop an automatization procedure. After one arc discharge, the energy transferred to the tips causes their melting and, as the temperature in the fibers outer region decreases faster than on the inside, some air is trapped, forming a microbubble (Figure IV.4e) [15]. To illustrate the influence of the splicing parameters in the air bubbles production, several structures were fabricated. Figure IV.5 shows the FP cavity length (L_{FP}) as a function of the arc discharge time and power, after applying one arc discharge.

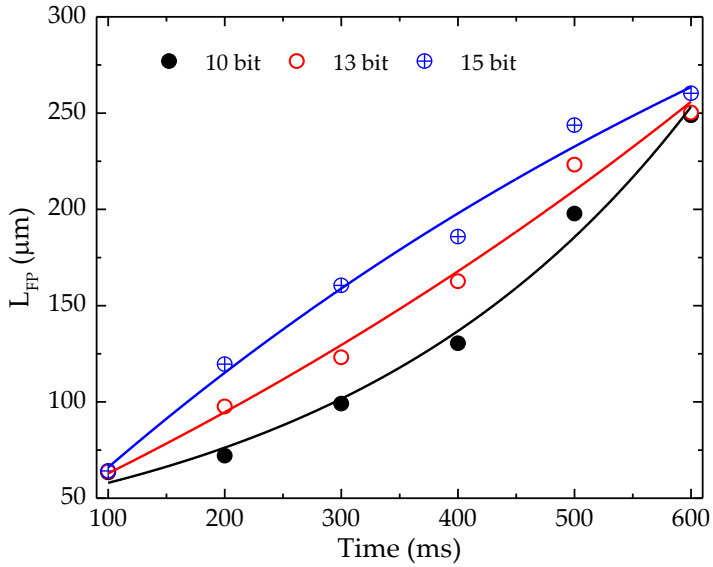

Figure IV.5. Variation of the FP cavity length with the fusion splicer parameters (time and electric power).

As expected, the increase of both parameters leads to larger cavities. However, in all cases the behavior is non-linear, as evidenced by the tendency curves. Above 600 ms, the cavities became damaged and could not be used for the sensor fabrication. Notice that all sensors presented in this work were fabricated using an arc power of 10 bits and duration of 400 ms (steps shown in Figure IV.4e and IV.4g). The fiber with the air bubble was then cleaved as close to the cavity as possible, under a 5x magnifying lens (Figure IV.4f). The final step consisted in placing the fiber tip in the splice machine with a considerable

lateral offset, after which successive arcs were applied until the desired round shape was obtained (Figure IV.4g). The arc discharge was not applied directly to the fiber to prevent the collapsing of the structure. With this final step, the influence of possible issues during cleaving (such as scratches, undesired cleaving angle or other surface imperfections) was minimized as the electrical arc discharges reshaped the sensing structure to attain the desired spherical cavity with thin diaphragm. The microscope photograph of one of the cavities produced is shown in Figure IV.4h.

5. Experimental results and discussion

Figure IV.6 displays the experimental setup used in this work. The spectral response of this sensing structure was observed in a typical reflection scheme, by connecting the broadband optical source (bandwidth of 50 nm), the optical spectrum analyzer (OSA Anritsu MS9740A), and the sensing head to the three ports of an optical circulator[7]. The readings were performed with a resolution of 0.02 nm.

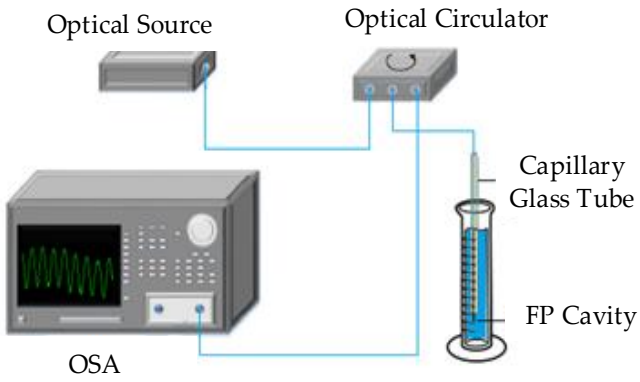

Figure IV.6. Scheme of the experimental setup.

A series of mixtures consisting of different mass fractions of deionized water in glycerin were prepared under a controlled laboratory environment, from 0 to 100 wt.%, translating into a refractive index variation between 1.4571 RIU and 1.3165 RIU. The solutions were prepared by adding different amounts of water to 25 g of glycerin. A

[7] Please see the Additional Information Section at the end of this Chapter for more results.

magnetic stirrer (NAHITA, magnetic stirred, model nº 690/1) was used to dilute the deionized water in the glycerin. After the preparation, the samples were stored during 24 hours, to allow their stabilization. The sensing tip was inserted vertically in the different solutions with the aid of capillary glass tube, as shown in Figure IV.6. This ensured the sensor robustness as well as the stability of the fiber inside the liquid. Notice that the cavity was kept outside this tube, in direct contact with the solutions.

Three sensors with different diaphragm thicknesses were fabricated through the method described in section IV. The dimensions presented in Figure IV.7 were obtained taking into consideration the microscope images as well as the spectral characteristics (Figure IV.8). The associated uncertainty was of ±3 μm.

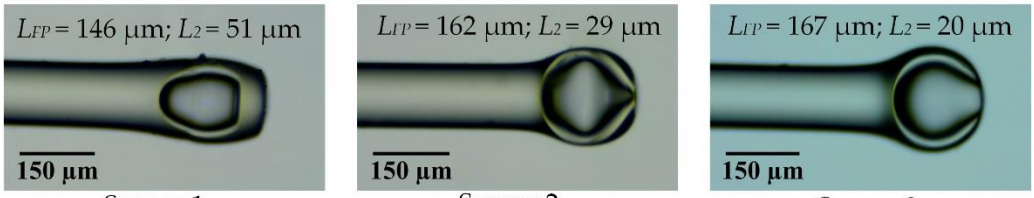

Figure IV.7. Microscope images of three sensing heads with respective cavity and diaphragms dimensions.

The sensors spectral response in different media (air, water and glycerin) is shown in Figure IV.8. For smaller diaphragm thicknesses (Figure IV.8b-c), there is a change of the visibility when the sensing head is placed in a liquid media. Besides the fringe period also changes, which corroborates with the numerical simulation previously presented. This behavior is highly dependent on the diaphragm thickness. The spectrum of the sensor with larger diaphragm does not present any significant dependence on the surrounding medium.

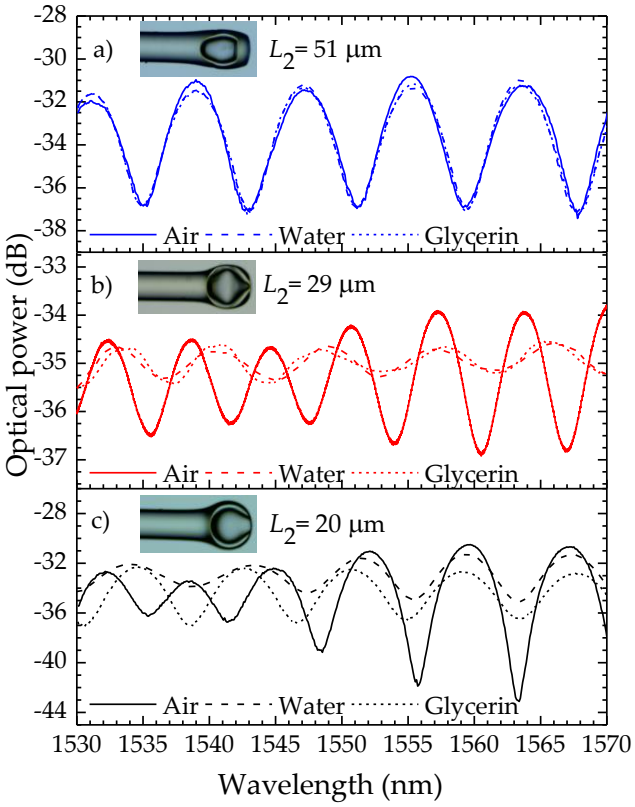

Figure IV.8. Spectra of the different sensing heads in air, water and glycerin. L_2 corresponds to the diaphragm thickness.

The wavelength shift dependence with water mass fraction in glycerin is shown in Figure IV.9. There is an approximately linear behavior in all cases. Sensitivities of -0.29 pm/wt.%, 3.61 pm/wt.%, and 7.81 pm/wt.%, were achieved for the sensors 1, 2, and 3, respectively. As expected, the thickness of the diaphragm influences the sensor sensitivity: sensors with smaller diaphragms present higher sensitivities to the water presence in glycerin. Comparing sensor 2 and 3, the air cavity lengths are very approximate. However, sensor 3, which has a thinner diaphragm, is 2.2 times more sensitive than sensor 2. Considering the sensor with the highest sensitivity, and taking into account the OSA resolution, an experimental resolution of 2.5 % of water weight in glycerin was estimated.

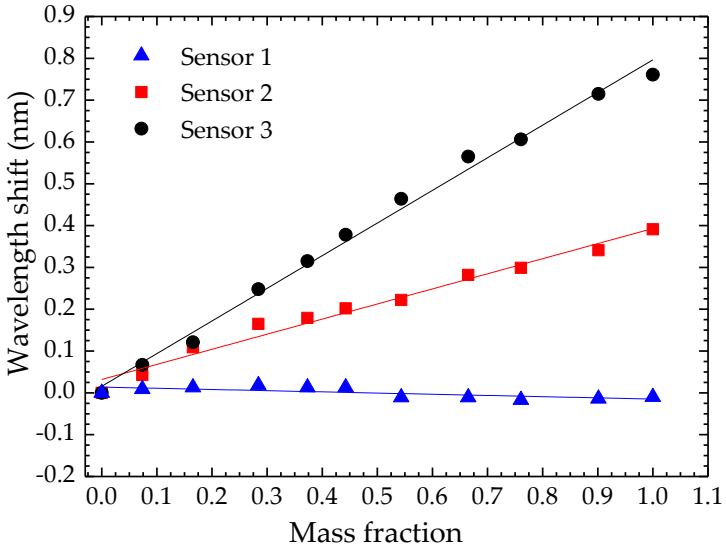

Figure IV.9. Sensors response to mass fraction variations.

The influence of the air cavity length in the sensor response was evaluated by comparing the responses of sensor 2 (L_{FP}=162 μm and L_2=29 μm) with a new sensor, whose image is depicted in Figure IV.10 (L_{FP}=196 μm and L_2=32 μm). The sensor with the largest cavity presented a lower sensitivity (2.75 pm/wt.%) than the other one (3.61 pm/wt.%). This means that the behavior of this sensing structure does not depend significantly on the microbubble cavity length.

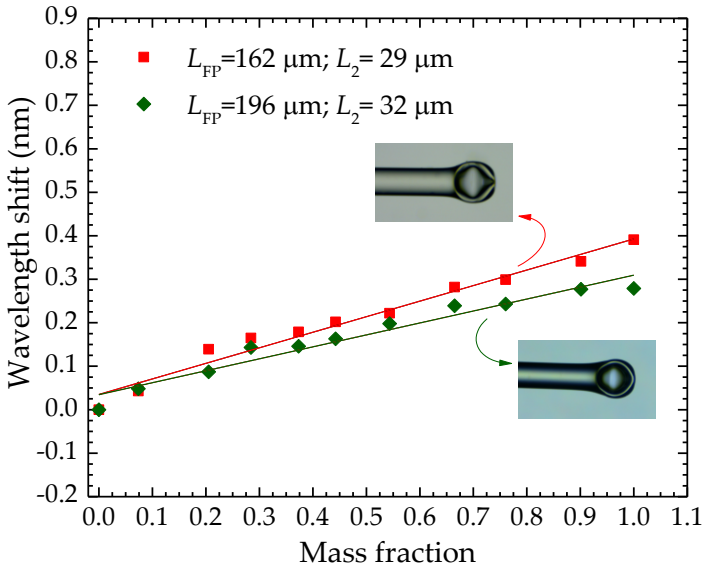

Figure IV.10. Sensors response to mass fraction variations. L_2 corresponds to the diaphragm thickness and L_{FP} is the air cavity length.

Using the relationship between refractive index and mass fraction described in section 3 the sensing heads responses towards the changes in the solutions refractive index were determined (Figure IV.11).

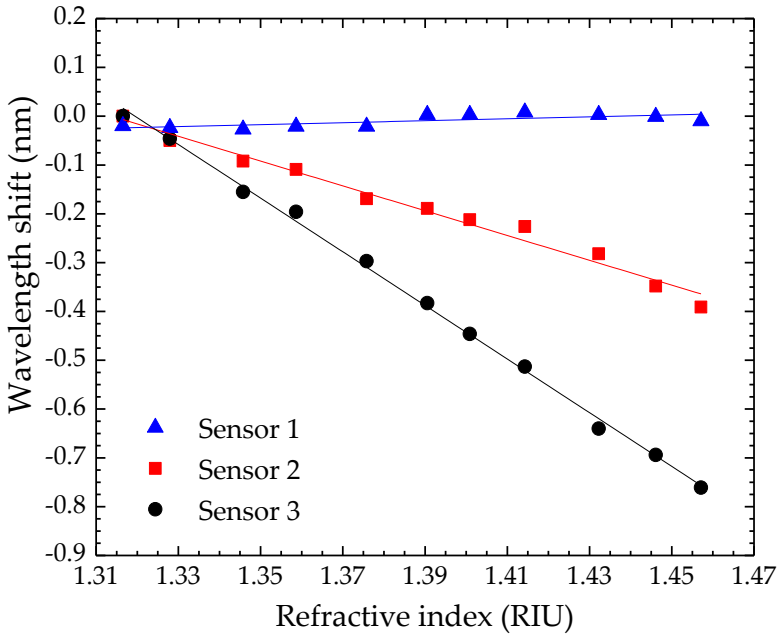

Figure IV.11. Sensors response to external refractive index variations.

Once again, sensor 3 presents the highest sensitivity, being of -5.49 nm/RIU followed by the sensor with the 29 μm long diaphragm, with the sensitivity of -2.54 nm/RIU. Sensor 1 revealed to be insensitive towards this parameter (0.20 nm/RIU).

The temperature response of the microcavity sensor was measured by immersing the sensor 3 in water, which was heated up to 80 °C, using a hot plate. The wavelength variations were monitored using the same interrogation scheme as shown in Figure IV.6. The temperature was raised in steps of 5 °C, from room temperature up to 80 °C. The same process for the cooling was followed. The sensor response to the temperature variations is shown in Figure IV.12. A sensitivity of 1.6 pm/°C, was determined, which is in good agreement with the sensitivity found in the literature for a hollow silica sphere tip [18]. A temperature cross sensitivity of 0.2 wt.%/°C was estimated for this sensor.

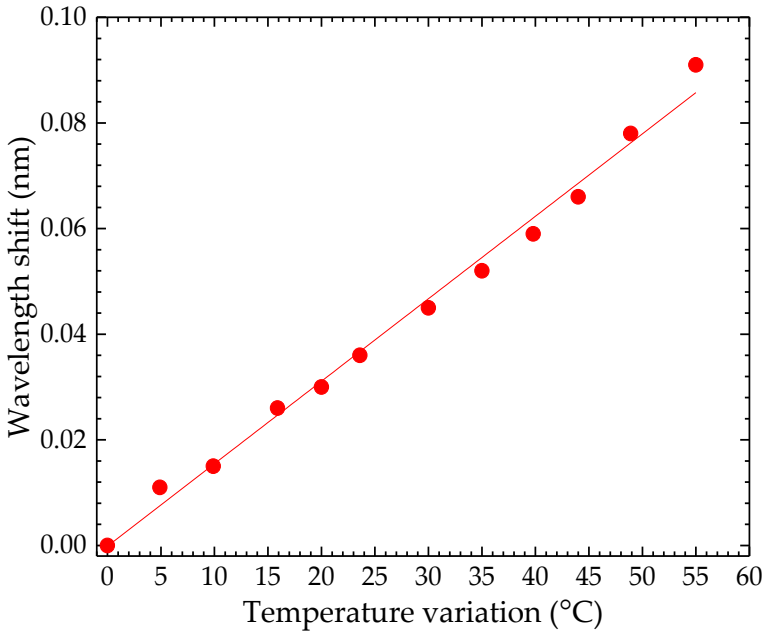

Figure IV.12. Response of sensor 3 to water temperature variations.

There are a number of advantages associated with this sensing device. As the microbubble is fabricated between two sections of standard multimode fiber, the sensor is cost effective. Given its reduced dimensions, it can be used for punctual detection, requiring low volume samples. Also, as shown in Table IV.2, the FP air cavities at the fiber tip are usually sensitive in visibility. In this work, the variations also occur in wavelength.

Table IV.2. Comparison between the results reported in the literature and this work regarding FP air cavities at the fiber tip.

Configuration	FP Cavity Length (μm)	Range (RIU)	Sensitivity/ Resolution	Ref.
SMF + etched graded-index fiber	515	1.32-1.45	~160 dB/RIU	[26]
SMF + etched graded-index fiber	25	1.32-1.47	~45.05 dB/RIU	[27]
Ellipsoidal cavity between SMF + photonic crystal fiber (PCF)	~14	1.332-1.45	~61.74 dB/RIU	[9]
Simplified hollow core fiber with hollow silica sphere tip	~119.7	1.33-1.457	6.2×10^{-5} RIU (visibility)	[18]
Air cavity between SMF + HC PCF	---	1.333-1.413	-54.409 dB/RIU	[20]
Air cavity between two sections of MMF	~147	1.316-1.457	-5.49 nm/RIU	Present work

Notice that in this Table were only included sensing configurations where the cavity is enclosed in the fiber and the liquid does not enter in direct contact with the fiber core. Furthermore, as it does not require any special fibers, hazardous chemicals or oils to be fabricated, this sensor can be a good alternative to the sensors reported in the literature.

6. Conclusions

A fiber-optic sensor based on a Fabry-Perot interferometer formed at the tip of a multimode fiber was proposed for the detection of water in glycerin. Three sensing heads with different diaphragm thicknesses were fabricated using only the splicing technique. It was observed that the diaphragm thickness influences the sensor sensitivity. The sensor with the thinner diaphragm presented the highest sensitivity of 7.81 pm/wt.% regarding the variation of water mass fraction in glycerin. This parameter was converted into refractive index variations and a maximum sensitivity of -5.49 nm/RIU was achieved. Furthermore, the sensing head was characterized towards temperature, with a cross sensitivity of 0.2 wt.%/°C. This kind of measurements can be considered an added value both for industry and medicine, since one of the most important parameters in the glycerin characterization process is its purity degree, especially when it is used in the pharmaceutical and cosmetic area.

Acknowledgments: This work was supported in part by the European Project "Stable Interfaces for Rechargeable Batteries" (SIRBATT) (FP7-ENERGY-2013, under Grant 608502) and in part by FEDER funds through the COMPETE 2020 Programme and National Funds through FCT-Portuguese Foundation for Science and Technology under the Project UID/CTM/50025/2013. The work of S. Novais and M. S. Ferreira was supported by the research fellowships BI/UI96/6643/2016 and BPD/UI96/7331/2016, respectively.

References

1. D. M. Cristancho, D. R. Delgado, F. Martinez, M. A. A. Fakhree, A. Jouyban, "Volumetric properties of glycerin + water mixtures at several temperatures and correlation with the Jouyban-Acree model," *Rev. Colomb. Cienc. Quim. Far.*, Vol. 40, no. 1, pp. 92-115, 2011.

2. R. D. Peralta, R. Infante, G. Cortez, R. R. Ramirez, J. Wisniak, "Densities and excess volumes of binary mixtures of 1,4-dioxane with either ethyl acrylate, or butyl acrylate, or methyl methacrylate, or styrene at T = 298.15 K," *J. Chem. Thermodynamics*., Vol. 35, no. 239, 2003.

3. J. Jimenez, F. Martinez, "Study of some volumetric properties of 1,2 propanediol + water mixtures at several temperatures," *Rev. Colomb. Cienc. Quím. Farm.,* Vol. 34, no. 46, 2005.

4. D. R. Delgado, F. Martinez, M. A. A. Fakhree, A. Jouyban, "Volumetric properties of the glycerin formal + water cosolvent system and correlation with the Jouyban- Acree model," *Phys. Chem. Liq.,* Vol. 50, no. 3, pp. 284-301, 2012.

5. F. Yang, M. A Hanna, R. Sun, "Value-added uses for crude glycerol-a byproduct of biodiesel production," *Biotechnology for Biofuels,* Vol. 3, pp. 1-10, 2012.

6. L. Melo, G. Burtona, P. Kubikb, P. Wilda, "Refractive index sensor based on inline Mach-Zehnder interferometer coated with hafnium oxide by atomic layer deposition," *Sens. Actuators B*., Vol. 236, pp. 537-545, 2016.

7. J. S. V. González, D. M. Hernández, D. M. Hernández, F. M. Pinón, I. H. Romano, "Simultaneous measurement of refractive index and temperature using a SPR-based fiber optic sensor," *Sens. Actuators B*., Vol. 242, pp. 912-920, 2017.

8. L. Qi, C. L. Zhao, J. Yaun, M. Ye, J. Wang, Z. Zang, S. Jin, "Highly reflective long period fiber grating sensor and its application in refractive index sensing," *Sens. Actuators B.,* Vol. 193, pp. 185-189, 2014.

9. T. Wang, M. Wang, "Fabry–Pérot Fiber sensor for simultaneous measurement of refractive index and temperature based on an in-fiber ellipsoidal cavity," *IEEE Photonic .Tech. L.,* Vol. 24, no. 19, 2012.

10. S. Pevec, D. Donlagic, "High resolution, all-fiber, micro-machined sensor for simultaneous measurement of refractive index and temperature," *Opt. Exp.*, Vol. 22, no. 13, 2014.

11. J. Villatoro, V. Finazzi, G. Coviello, and V. Pruneri, "Photonic-crystal fiber-enabled micro-Fabry-Perot interferometer," *Opt. Lett*., Vol. 34, no.16, pp. 2441-2443, 2009.

12. Y. Liu, S. Qu, W. Qu, R. Que, "A Fabry-Perot cuboid cavity across the fibre for high-sensitivity strain force sensing," J. Opt. Vol. 16, pp. 105401, 2014.

13. S. Liu, K. Yang, Y. Wang, J. Qu, C. Liao, J. He, Z. Li, G. Yin, B. Sun, J. Zhou, G. Wang, J. Tang, and J. Zhao, "High-sensitivity strain sensor based on in-fiber rectangular air bubble," *Sci. Reports*., Vol. 5, pp. 7624, 2015.

14. M. Deng, C. P, Tang, T. Zhu, and Y. J. Rao, "PCF- based Fabry-Perot interferometric sensor for strain measurement at high temperatures," *IEEE Photonic. Tech. L.,* Vol. 23, no. 11, pp. 700-702, 2011.

15. D. W. Duan, Y. J. Rao, Y. S. Hou, and T. Zhu, "Microbubble based fiber optic Fabry-Perot interferometer formed by fusion splicing single-mode fibers for strain measurement," *Appl. Optics.,* Vol. 51, no. 8, pp. 1033-1036, 2012.

16. C. L. Lee, H. J. Chang, Y. W. You, G. H. Chen, J. M. Hsu, J. S. Horng, "Fiber Fabry-Perot interferometers based on air-bubbles/liquid in hollow core fibers," *IEEE Phot. Tech Lett.,* Vol. 26, no. 8, pp. 749-752, 2014.

17. S. Liu, Y. P. Wang, C. R. Liao, G. J. Wang, Z. Y. Li, Q. Wang, J. T. Zhou, K. M. Yang, X. Y. Zhong, J. Zhao, J. Tang, "High-sensitivity strain sensor based on in-fiber improved Fabry-Perot interferometer," Opt Lett., Vol. 39, no. 7, pp. 2121-2124, 2014.

18. D. J. J. Hu, Y. Wang, J. L. Lim, T. Zhang, K.B. Milenko, Z. Chen, M. Jiang, G. Wang, F. Luan, P.P. Shum, Q. Sun, H. Wei, W. tong, T.R. Wolinski, "Novel miniaturized Fabry-Perot refractometer based on a simplified hollowcore fiber with a hollow core silica sphere tip," *IEEE Sensors J.,* Vol. 12, no. 5, pp. 1239-1245, 2012.

19. M. C. Contreras, A. D. G. Chavez, E. V. Rodriguez, E. G. Arellano, D. J. V., R. I. M. Chavez, M. T. Cisneros, R. R. Laguna, "Refractive index sensing setup based on a taper and an intrinsic micro Fabry-Perot interferometer," *J.Eur.Opt.Soc.Rapi.,* Vol. 10, no. 15039, 2015.

20. G. Zhang, M. Yang, Y. Dai, "Fabry-Perot fiber tip sensor based on an inner air-cavity for refractive index sensing," Chinese Opt Lett., Vol. 12, no. 7, pp. S11201-S11202-2, 2014.

21. S. Novais, M. S. Ferreira, J. L. Pinto, "Lateral load sensing with an optical fiber inline microcavity," *IEEE Photonic. Tech. L.,* Vol. 29, no. 17, pp. 1502-1505, 2017.

22. Z. L. Ran, Y. J. Rao, W. J Liu, X. Liao, K. S. Chiang, " Laser-micromachined Fabry-Perot optical tip sensor for high-resolution temperature-independent measurement of refractive index," *Opt. Exp.*, Vol.16, no. 3, pp. 2252-2263, 2008.

23. J. Ma, J. Ju, L. Jin, W. Jin, D. Wang, "Fiber-tip micro-cavity for temperature and transverse load sensing," *Opt. Exp.*, Vol. 19, no. 13, pp. 12418-12426, 2011.

24. M. S. Ferreira, J. Bierlich, S. Unger, K. Schuster, J. L. Santos, O. Frazão, "Optical phase refractometer based on post-processed interferometric tip sensors," J. Lightwave Technol., Vol. 32, no. 17, pp. 3002-3007, 2014.

25. J. E. Saunders, C. Saunders, H. Chen, H. P. Loock, "Refractive indices of common solvents and solutions at 1550 nm," *App. Optics.,* Vol. 55, no. 4, 2016.

26. Y. A. Gong, Y. Guo, Y. J. Rao, T. A. Zhao, Y. Wu, " Fiber-Optic Fabry-Perot sensor based on periodic focusing effect of graded-index multimode fibers," Ieee Photonic Tech L, Vol. 22, no. 23, pp. 1708-1710, 2010.

27. Y. A. Gong, T. A. Zhao, J. Y. Rao, Y. Wu, Y. Guo, "A ray-transfer-matrix model for hybrid fiber Fabry-Perot sensor based on graded-index multimode fiber, Opt Express, Vol. 18, no. 15, pp. 15844-15852, 2010.

IVA - Additional Information

To complement the results previously discussed, inline FP sensors created between two sections of MMF using the same fabrication process as shown in Chapter IV were developed. The inline sensors were used to measure strain, and the results from this study were presented during the conference Photonics Europe, in May 2018, DOI: 10.1117/12.2307609.

Experimental Results

The spectral responses of these sensing structures were observed in the same way that in previous results (Figure IV.13).

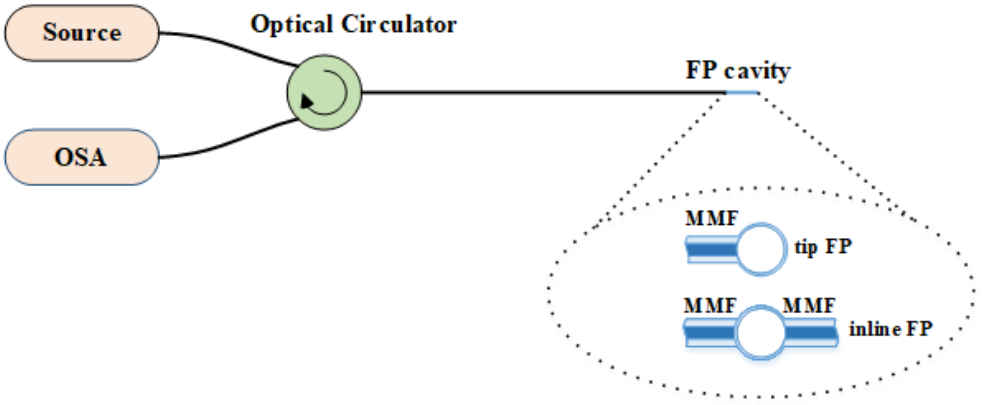

Figure IV.13. Scheme of the experimental setup with tip FP and inline FP.

The air spectra of the two configurations were compared and presented in Figure IV.14. The spectral behavior of the cavity, and consequently the spatial frequency spectra, are related not only to the air bubble dimensions, but also to the quality of the splices and the end face cleave. The visibility of an interferometric cavity can be determined by two adjacent maxima and minima of the interference signal. The tip FP presents a higher spectrum visibility (~61%), when compared to the inline configuration (~36%), as can been seen in Figure IV.14.

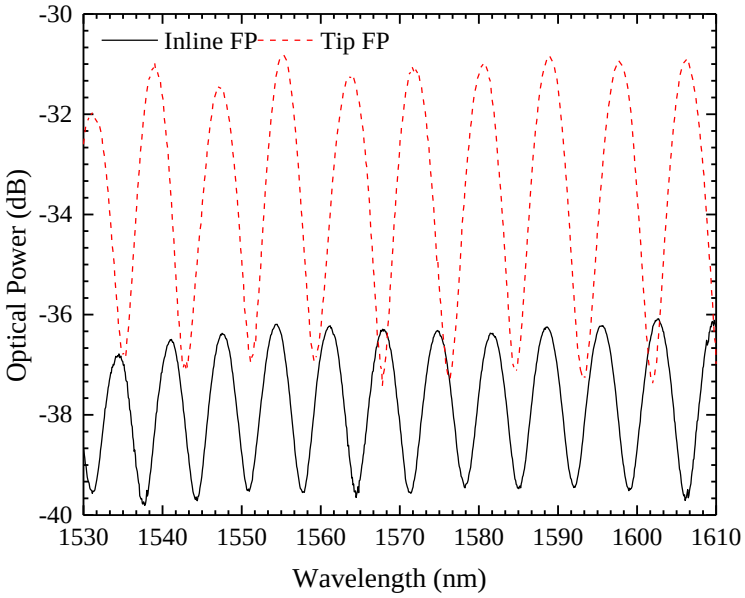

Figure IV.14. Spectra of the two developed sensing configurations.

Strain sensing

To perform the strain measurements, the inline FP sensor was fixed to a translation stage with a resolution of 10 μm. It can be seen in Figure IV.15a) that there is a wavelength shift towards longer wavelengths for all sensors. The experimental data were well adjusted to a linear function (with a correlation factor higher than 0.99). A minimum sensitivity of 1.25 pm/με was obtained, for the smallest cavity (with a length of ~40 μm), whereas the maximum sensitivity of 6.48 pm/με, was achieved for the largest cavity (297 μm long). A non-linear relationship between the strain sensitivity and the cavities lengths was observed, as shown in Figure IV.15b). Table IV.3 presents the sensitivities obtained for each sensor. It was observed that larger cavities exhibited higher sensitivities to strain.

Table IV.3. Sensitivities obtained for each sensor.

Sensor characteristics	Sensitivity
L_{Fp}= 40 μm	1.25 pm/με
L_{Fp}= 127 μm	1.76 pm/με
L_{Fp}= 218 μm	2.71 pm/με
L_{Fp}= 297 μm	6.48 pm/με

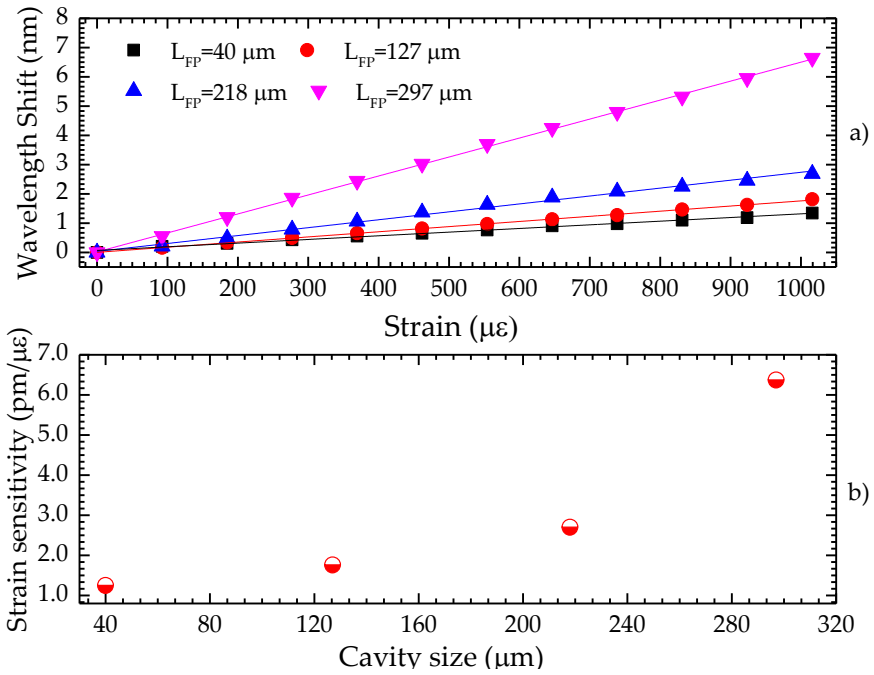

Figure IV.15. a) Sensors response to the applied strain and b) relation between cavity size and strain sensitivity.

The temperature response of both sensing configurations was evaluated by placing the 218 µm long inline sensor (Figure IV.16) in a thermal chamber. The temperature was raised in steps of 5 °C, from 10 °C until 65 °C, and maintained for about 30 min at each step to make sure that the temperature in the thermal chamber had stabilized. The proposed inline and tip sensor exhibited very low thermal dependence (< 1.8 pm/°C), meaning that with these sensing devices there are no need to perform temperature compensation. The cross-sensitivity between this parameter and strain for inline sensor was 0.8 µε/°C.

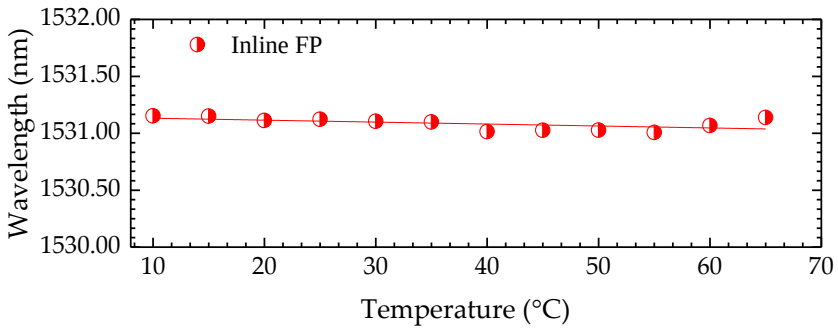

Figure IV.16. Inline sensor response to temperature variations.

V

Optical fiber tip sensor for the measurement of glucose aqueous solutions

Published in IEEE Photonics Journal, Vol. 10, no. 5, September 9, 2018

DOI: 10.1109/JPHOT.2018.2869944

Optical fiber tip sensor for the measurement of glucose aqueous solutions

Susana Novais, Catarina I. A. Ferreira, Marta S. Ferreira, João L. Pinto

Abstract: A reflective fiber optic sensor based on multimode interference for the measurement of refractive index variations in glucose aqueous solutions is proposed. The sensor is fabricated by splicing a short section of coreless silica fiber to standard single mode fiber. The influence of the coreless fiber dimensions on the sensor performance is analyzed. By changing the sensor length, no significant impact is observed. However, the reduction of the sensing head diameter leads to a large improvement of the sensitivity. The smaller sensor, with a length of 5 mm and a diameter of 24 μm, presents a maximum sensitivity of 1467.59 nm/RIU, for the refractive index range between 1.364 RIU and 1.397 RIU. Taking into account the acquisition system, a maximum theoretical resolution of 6.8×10^{-5} RIU is achieved.

Keywords: Fiber optic sensors, multimode interferometry, refractive index sensing, chemical analysis.

1. Introduction

The multimode interference (MMI), as typically example the single mode-multimode-single mode (SMS) structure, has been explored as an attractive technology on optical communications and sensing. Due to the clear advantages of simplicity, low-cost, facility of manufacture, and high repeatability, it emerges as an alternative to existing fiber-based refractometers [1], or for strain measurement with temperature compensation [2], curvature sensing [3] or in edge filtering for wavelength measurement [4]. The subjacent operating principle of this kind of sensors is the MMI excited between modes in the multimode fiber (MMF) section, which can be influenced by external perturbations [5, 6]. To perform refractive index sensing based on the SMS fiber structure, different techniques have been reported. For instance, a MMF core section was sandwiched between two single mode fibers (SMFs), where the MMF cladding was removed through chemical etching [1]. Zhao *et al.* proposed a sensor composed by two sections of SMF and one section MMF, with high sensitivity to refractive index [7]. Jung *et al.* reported a compact

surrounding refractive-index sensor using a multimode-coreless-multimode structure [8]. A SMS fiber structure used in combination with a uniform Bragg grating [9] and an enhanced evanescent field fiber sensor based on a tapered MMF sandwiched between two SMFs [10] have also been reported for refractive index measurement. Regarding the use of a coreless silica fiber as sensing device, some works have also been reported for the measurement of refractive index [11] and temperature [12], however the measurements were usually based on a transmission scheme [13, 14].

In many fields such as disease diagnosis, clinical analysis and quality monitor in food industry, the rapid and precise detection of glucose concentration is vital. In particular, the abnormal body blood glucose level monitoring is critically essential for human health [15]. The significance of glucose detection and potential commercial value has attracted constant effort on research. One of the used key methods for glucose sensing is centered on fluorescently labeled sensing schemes, which employ changes in fluorescent intensity to reflect sample concentration [16], but the short lifetime of fluorescent agents and the high cost of enzymes limit their further development and application in biosensing [17]. For that reason, the development of low-cost and robust sensing methods is highly desirable. A surface plasmon resonance fiber sensor based on a multimode plastic clad silica fiber was coated with silver and silicon films. Glucose oxidase was immobilized at the fiber surface for the detection of low levels of glucose [18]. A long period fiber grating coated with enzyme was firstly proposed by Deep *et al.* for the measurement of glucose. A linear relationship was found in the range of 10-300 mg dL^{-1} [19]. The same immobilization technique was used on a fiber with an 81° tilted Bragg grating (TFBG). A low temperature cross-talk, good linearity and Q-factor was achieved in the proposed glucose sensor [20]. A glucose sensor based on enzymatic graphene oxide functionalized TFBG was also proposed. The analytical range considered was of 0-8 mM, which contains the biological region for human blood glucose levels [21].

In this work, a multimode fiber tip interferometer based on an etched coreless silica fiber is proposed for the measurement of the refractive index variations of glucose aqueous solutions. A comparison between the performance of sensors with similar

diameters and different lengths, and similar lengths and different diameters is performed.

The reflection configuration has several advantages over the inline MMIs. On one hand, the length is reduced by half, since light is reflected at the coreless end face and recoupled to the single mode fiber. On the other hand, the cleaning procedure is easier, smaller amounts of analyte can be employed, the sensing structure becomes less fragile, even after etching, and it can be placed at a long distance regarding the acquisition system, thus becoming a good alternative in harsh environments where refractive index or concentration variations need to be monitored.

2. Sensor and operation principle

The sensing device developed in this work consists on a short section of coreless silica fiber (CSF) spliced to single mode fiber (SMF), as shown in Figure V.1. Light is guided through the SMF and when it enters the coreless fiber section, several modes are excited and guided until the fiber end section is achieved. Due to the Fresnel reflection, a small fraction of the light is reflected and recoupled once again to the SMF fundamental mode.

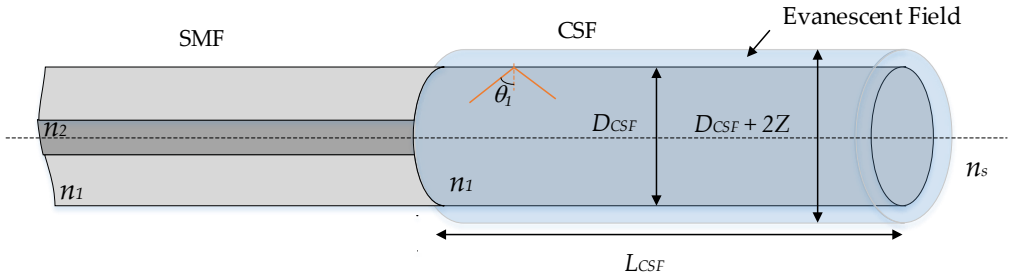

Figure V.1. Schematic diagram of the sensor structure, where n_1 is both the refractive index of the SMF cladding and the coreless fiber, n_2 and n_s are the refractive index of SMF core and surrounding medium; L_{CSF} and D_{CSF} are the coreless fiber length and diameter, respectively, and Z is the evanescent field penetration depth.

The interference wavelength, λ_0, can be expressed according to Eq. 1 [22]:

$$\lambda_0 = \frac{n_1 D_{CSF}^2}{2L_{CSF}} p \,, \tag{1}$$

where n_1, D_{CSF}, and L_{CSF} are the CSF refractive index, diameter, and length, respectively,

whereas p is the interference number. One of the important characteristics of a multimode interferometer (MMI), is that λ_0 can be easily designed to be in the wavelength region used, by selecting the appropriate dimensions [22]. When p = 4, the self-image is formed due to the constructive interference between several guided modes, and the sensor presents lowest losses [13]. However, at different interference numbers, even though no self-image is present, the constructive interference between two consecutive modes with high coupling efficiency can originate a spectrum that, although with higher losses, is still suitable to perform measurements.

From Eq. 1, there is no obvious dependence of the wavelength with the external medium. However, if one considers the evanescent field generated at the CSF/external media interface, the diameter can be considered as an effective value of $D + 2Z$, where Z corresponds to the penetration depth. This parameter is given by Eq. 2 [12],

$$Z = \frac{\lambda_0}{2\pi n_1 \sqrt{\sin^2\theta - \left(n_s/n_1\right)^2}}, \tag{2}$$

where n_s is the surrounding medium refractive index and θ is the incident angle at the CSF/surrounding medium interface, as shown in Figure V.1. As the environmental refractive index changes, the propagation constants for each guided mode within the CSF will change too, which leads to shifts in the output spectra, owing to the direct exposure of the CSF [23].

To determine the influence of both CSF length and diameter on the sensitivity of the developed sensors, the previous equations were combined and solved in order to obtain the wavelength dependence on refractive index. The CSF refractive index was considered to be 1.444 at 1550 nm, and θ was estimated to be 84.94° [24]. In the first part of the simulation, the diameter was fixed to be 125 μm, and the length varied between 28.2 mm and 50.0 mm (Figure V.2a). In the second part, the length parameter was kept constant (5 mm), and the diameter was changed between 125 μm and 24 μm (Figure V.2b). The interference order p was estimated using Eq. 1, for an operation wavelength within the 1550 nm range.

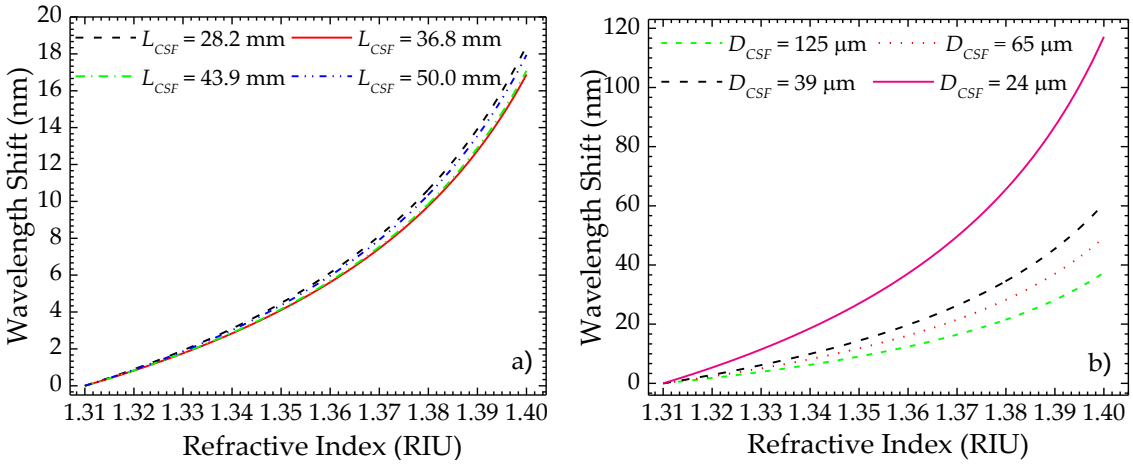

Figure V.2. Simulated wavelength shift dependence on external media refractive index, considering a) constant diameter and different lengths and b) constant length and different diameters.

As can been seen in the simulation results, the wavelength shift increases non-linearly with the surrounding refractive index. This behavior is expected until the refractive index of the external medium becomes close to the one of the CSF. In this case, the total internal reflection condition ceases to exist, and no light is expected to be reflected at in the sensor region. In Figure V.2a), there is no direct correlation between the CSF length and the wavelength shift. However, if the ratio between L_{CSF} and p is taken into account, the relationship becomes clearer: larger values of L_{CSF}/p lead to lower sensitivities. For instance, a 36.8 mm long sensor (L_{CSF}/p = 7.36) has a similar response to the one with a length of 43.9 mm (L_{CSF}/p = 7.32), whereas the sensors with lengths of 50.0 mm (L_{CSF}/p = 7.14) and 28.2 mm (L_{CSF}/p = 7.05) are more sensitive than in the previous cases. This ratio can be used to maximize the sensors sensitivity, according to the desired application. Nevertheless, in this case no significant changes are observed in the sensors response, meaning that the variation of length does not play a decisive role in the sensitivity. However, the smaller the diameter, the more significant becomes the evanescent field, which translates into higher sensitivities.

3. Results

Figure V.3 presents the scheme of the experimental setup used in this work, both for the refractive index measurements in liquid media and for the temperature experiments. The sensing structure spectral response was observed in a typical reflection scheme, by connecting the broadband optical source (bandwidth of 80 nm, centered at 1570 nm), the sensing head, and the optical spectrum analyzer (OSA Anritsu MS9740A) to the three ports of an optical circulator. The readings were performed with a resolution of 0.1 nm.

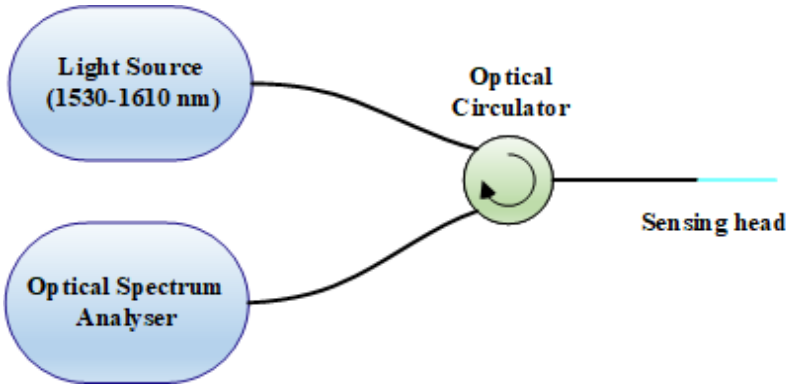

Figure V.3. Scheme of the experimental setup.

A series of glucose aqueous solutions were prepared under a controlled laboratory environment, with glucose mass fractions ranging from 0 wt.% to ~45 wt.%. A magnetic stirrer (NAHITA, magnetic stirred, model nº 690/1) was used to dilute the glucose in the deionized water. After the preparation, the samples were stored for 24 hours, to allow their stabilization. The refractive index experiments were carried out at room temperature (~23 °C), under a controlled environment. The sensor was inserted vertically in the different solutions with the aid of capillary glass tube. However, the sensing area was kept outside this tube, in direct contact with the measurand. This setup ensured the sensor robustness as well as the stability of the fiber inside the liquid.

Figure V.4 presents the shifts in the reflection spectra due to the direct exposure of the CSF under different percentages of glucose, for one sensing head with a diameter of 125 μm and a length of 59.6 mm (sensor 1). With the increase of the mass fraction, not

only the amplitude of the reflected spectra changes, but there is also a notorious wavelength shift. This is related to the increase of the solutions refractive index, ie with the increase of glucose concentration in the aqueous solution.

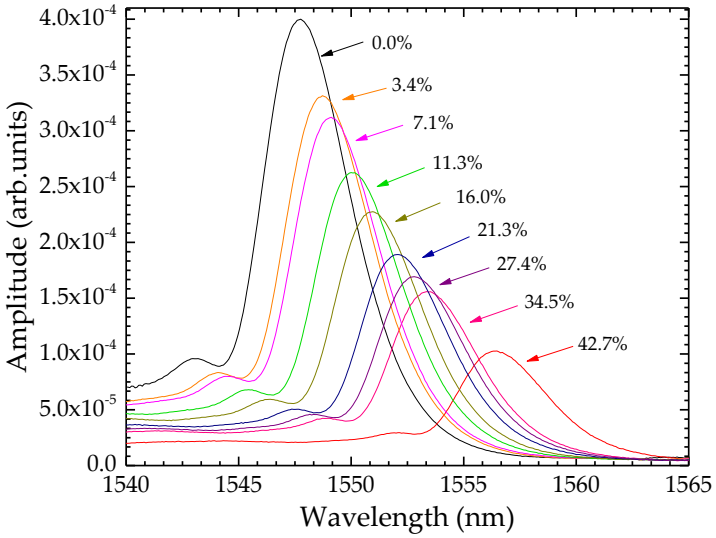

Figure V.4. Output spectra of sensor 1 under different mass fraction percentages of glucose.

The refractive index of each solution was measured using an Abbe refractometer (Krüss optronic refractometer), that provides information in the spectral visible range ($\lambda = 589$ nm). Since the optical source used in the experiments was centered in the 1550 nm region, it was necessary to first calibrate the solutions and thus estimate the refractive index at this wavelength range.

This was achieved by subjecting sensor 1 to previously calibrated glycerin aqueous solutions, where the refractive index at 1550 nm has been determined [25]. The wavelength shift ($\Delta\lambda$) dependence on refractive index (n), shown in Figure V.5a), was adjusted by the second order polynomial (Eq. 3):

$$\Delta\lambda = 2725.11n + 1604.23n^2 \quad (3)$$

with a correlation factor of 0.998. The same sensor was then evaluated for each glucose-water mixture and, by using the previous equation, it was possible to convert wavelength variations into refractive index. Figure V.5b) shows the relation between refractive index and mass fraction for the glucose solutions at the two wavelength regions considered. It is possible to observe that in both cases the behavior is similar. A third-

order polynomial fit was applied to the data, according to Eq. 4:

$$n(w) = A + Bw + Cw^2 + Dw^3, \tag{4}$$

where w indicates the solubility range as weight fraction, whereas A, B, C, and D are the fitting parameters. The values are gathered in Table V.1.

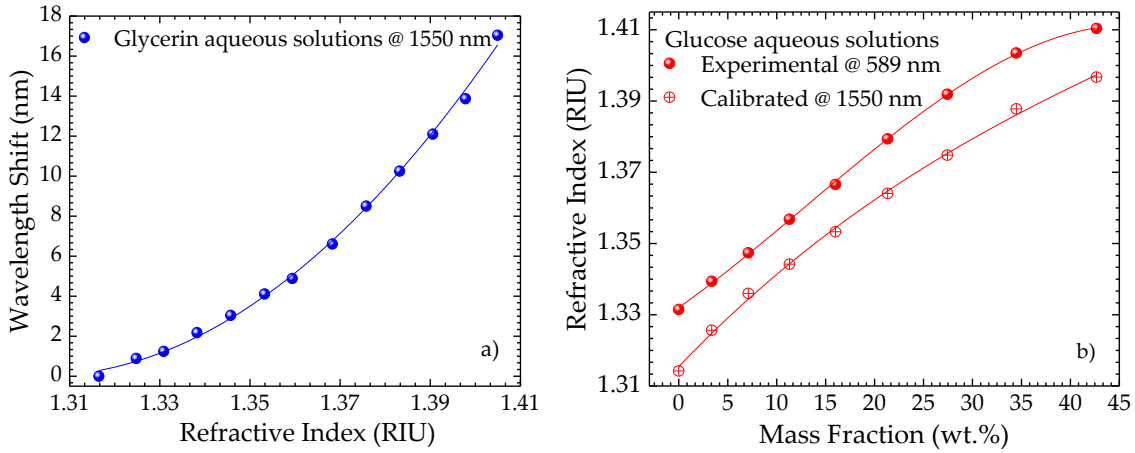

Figure V.5. Sensor calibration to refractive index measurements. a) wavelength shift dependence on refractive index of glycerin aqueous solutions, for an operating wavelength of 1550 nm and b) refractive index variation with mass fraction for glucose aqueous solutions, at 589 nm, measured through the Abbe refractometer and 1550 nm, determined from the calibration.

Table V.1. Parameters for third order polynomial fits of the refractive index dependence on mass fraction for glucose solutions, at 589 nm and 1550 nm.

	Glucose (1550 nm)	**Glucose (589 nm)**
w	0 - 0.45	0 - 0.45
A	1.3166	1.3320
B	0.00287	0.0019
C	-3.0260×10^{-5}	2.8140×10^{-5}
D	1.8666×10^{-7}	-7.1865×10^{-7}

Four sensors with lengths ranging from 28.2 mm to 50.0 mm were fabricated. Considering the refractive index of the CSF to be 1.444, and the operation wavelength in air of ~1530 nm, p was estimated to be between 4 and 7. Although the self-image occurs at $p = 4$, and lower losses are obtained, the sensors revealed to be adequate to perform refractive index measurements. The results are shown in Figure V.6. As expected, in all

cases the behavior is non-linear, following the tendency described in Section 2. Furthermore, it is observed that there are no significant changes regarding the sensor sensitivity. Two different linear regions were considered to estimate the sensors sensitivity, k_n. The first region, for lower refractive index variations, ranges from 1.316 RIU and 1.353 RIU, whereas the higher refractive index variations were considered between 1.364 RIU and 1.397 RIU. The sensitivities attained are shown in Table V.2, where D_{CSF} and L_{CSF} are the CSF diameter and length, respectively.

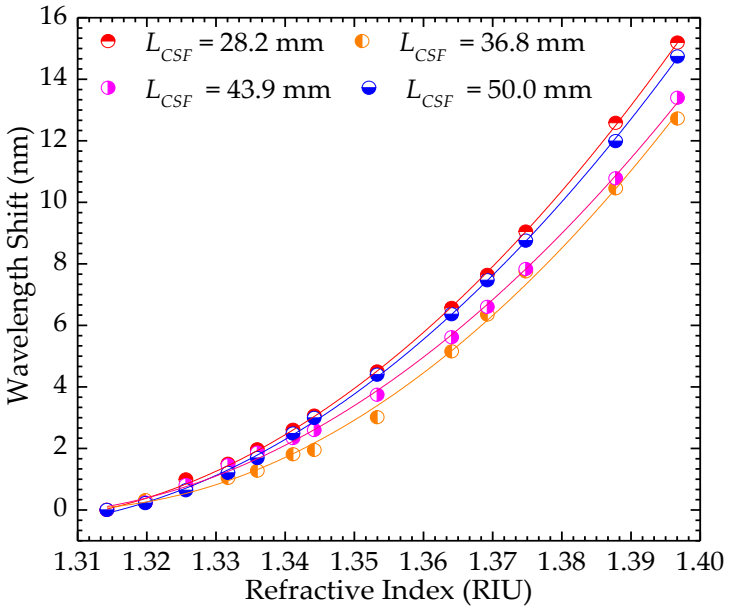

Figure V.6. Sensors response to refractive index variations for sensors with different lengths.

Table V.2. Sensitivities obtained for each sensor.

Sensor characteristics			**1.316 – 1.353**		**1.364 – 1.397**	
p	***D*CSF (μm)**	***L*CSF (mm)**	***k*n (nm/RIU)**	***r*²**	***k*n (nm/RIU)**	***r*²**
4	125	28.2	114.42	0.976	266.53	0.997
5		36.8	73.49	0.971	228.68	0.998
6		43.9	96.49	0.989	236.93	0.994
7		50.0	113.29	0.952	255.44	0.995

The length of the sensing device can be a limiting factor in practical applications. When using sensors with several centimeters in length, not only the sensors become more fragile, but also larger sampling volumes are required, since the liquid must be in contact with the whole sensing structure. However, in order to have a reflection spectrum with a

peak in the 1550 nm region, and considering smaller lengths, it is necessary to reduce the fiber diameter as well. Besides, as it was observed in Section 2, an increase of the sensor sensitivity is expected with the decrease of the diameter. To further test the sensing performance and evaluate the practicability of these sensors, four different samples with a length of ~5 mm were produced. Three of these sensors were subjected to wet chemical etching using a 40% hydrofluoric acid (HF) solution. To obtain a structure with a nearly constant core diameter over its length, as well as a smooth surface, the HF solution was placed inside an ultrasound bath at room temperature.

A preliminary experiment was performed to determine the etching rate[8]. A sample of CSF was submerged in liquid HF, at room temperature, for a few minutes, after which it was removed from the solution and cleaned thoroughly with ethanol. A microscope picture was taken to estimate the CSF diameter. The sample was once one again placed in the etching solution for a few additional minutes and the process was repeated. An etching rate of 1.63 μm/min was determined. Figure V.7 presents the wavelength dependence with the refractive index variations for the sensors with different CSF diameters, which ranged from 125 μm to 24 μm, translating into *p* values between 1 and 19.

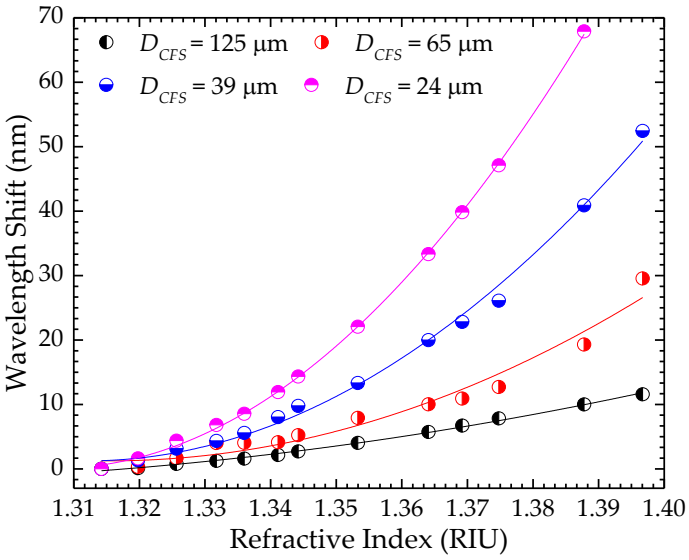

Figure V.7. Sensors response to refractive index variations.

[8] More information regarding the etching rate in the Additional Information Section at the end of this Chapter.

As observed for the non-etched sensors, a non-linear response is obtained. However, in this case, the difference between each sensor response is more significant and, as expected, the sensor with a smallest diameter presented the highest sensitivity. Once again, two different ranges can be considered, between 1.316 RIU and 1.353 RIU, and between 1.364 RIU and 1.397 RIU. Table V.3 summarizes the sensitivities to refractive index (k_n) obtained for each sensor, in both regions considered. As can be seen from the results, as the diameter of the CSF decreases, the sensitivity increases, in both ranges presented. The thinnest sensor is 8.3× more sensitive than the one with largest diameter, for the higher refractive index range. Considering the sensor with the highest sensitivity and the OSA resolution, a maximum theoretical resolution of 6.8×10^{-5} RIU is achieved [26]. The results indicate that it is possible to tailor the sensor dimensions according to the desired sensitivity and to the application. Larger sensors, on one hand, do not exhibit high sensitivities, and require higher volume samples. On the other hand, smaller sensors present better responses. However, as the diameter decreases, the fiber becomes more fragile. In such case, and considering a practical application, a suitable package should be developed to ensure robustness of the sensor. Nevertheless, in all cases the sensors presented a fast response and were very stable in the liquid media.

Table V.3. Sensitivities obtained for each sensor.

	Sensor characteristics		**1.316 – 1.353**		**1.364 – 1.397**	
p	L_{CSF} **(mm)**	D_{CSF} **(μm)**	k_n **(nm/RIU)**	r^2	k_n **(nm/RIU)**	r^2
1	5	125	102.42	0.959	177.69	0.999
3		65	197.84	0.903	582.54	0.945
7		39	338.23	0.972	1012.66	0.974
19		24	544.88	0.956	1467.59	0.995

The temperature response was measured by placing the sensor with a diameter of 125 μm and with a length of 43.9 mm, in a tubular oven with a resolution of 1 °C. The temperature was increased in steps of 100 °C, until 700 °C, and maintained for about 20 min at each step to make sure that the temperature in the oven had stabilized. Figure V.8a) presents the sensor response towards this parameter. It exhibited thermal dependence of 6.8 pm/°C, with a correlation factor of 0.978. The sensitivity towards

temperature is essentially due to the silica thermal expansion, being comparable to that of a fiber Bragg grating [27]. The sensor stability was evaluated by placing the sensor in the water solution, at room temperature, for 90 minutes. The spectrum was acquired every 30 seconds. The peak wavelength variations with time, is shown in Figure V.8b). The mean value was of 1535.86 nm and the standard deviation was of 0.01 nm. During the experiment, the temperature fluctuations were of 0.2 °C. The proposed sensor revealed high stability, the results are reproducible, and the cross-sensitivity was determined to be 7.1×10^{-5} RIU/°C.

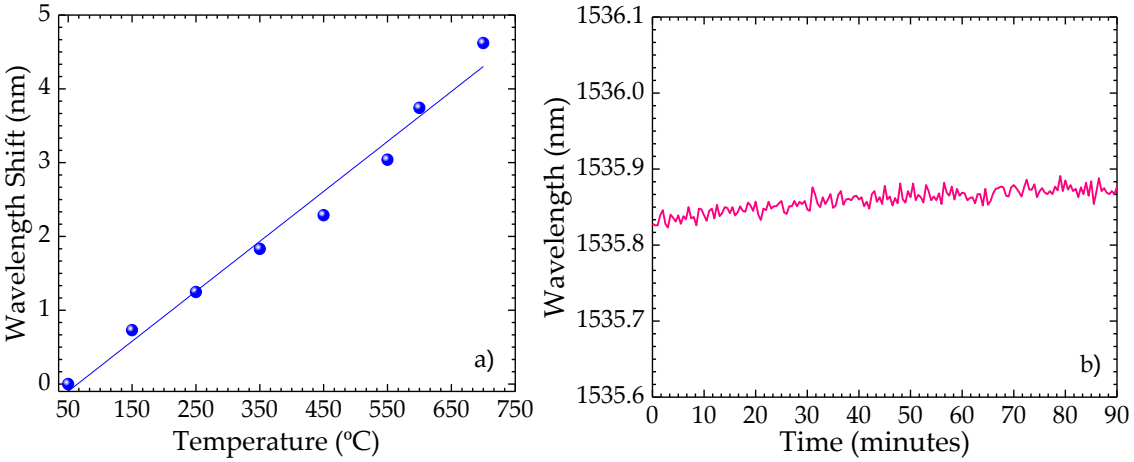

Figure V.8. Response of the sensor with a diameter of 125 μm to temperature variations a) and long term stability experiment, using a solution of water at room temperature b).

4. Conclusions

In summary, a high-sensitivity reflective optical fiber sensor based on coreless silica fiber (CSF) for the measurement of refractive index variations in glucose aqueous solutions was proposed. The sensor was fabricated by splicing standard single mode fiber to a short section of CSF. Firstly, four sensors with the same diameter and different lengths were used to perform refractive index measurements. It was observed that the CSF length has no significant influence on the sensitivity to external medium variations. The influence of the sensor diameter was studied by using four samples with similar lengths. Three of such samples were subjected to wet chemical etching using a 40% hydrofluoric acid solution, to decrease their diameter. It was observed that as the

diameter decreased, the sensitivity increased significantly. In fact, the sensor with the smaller diameter presented a maximum sensitivity of 1467.59 nm/RIU, for the refractive index range between 1.364 RIU and 1.397 RIU. By reducing the structure diameter, an enhancement of ~8.3× was achieved. In practical applications, the sensitivity to temperature should be compensated with a suitable method. The developed structure has attractive advantages, such as simple structure, fast response and stability. It has possibilities to expand in various sensing applications, where the use of only a fiber tip can be a better alternative to inline multimode interference sensors.

Acknowledgements: This work was supported by FEDER funds through the COMPETE 2020 Programme and National Funds through FCT-Portuguese Foundation for Science and Technology under the Project UID/CTM/50025/2013 and POCI-01-0145-FEDER-016414. Susana Novais, Catarina I. A. Ferreira and Marta S. Ferreira are grateful for the research fellowships no. BI/UI96/6643/2016, SATCTPAC1003612015, BPD/UI96/6274/2017, and SFRH/BPD/124549/2016, respectively.

References

1. Q. Wang, G. Farrell, "All-fiber multimode-interference-based refractometer sensor: proposal and design," *Opt. Lett.*, Vol. 31, pp. 317-319, 2006.

2. A. M. Hatta, Y. Semenova, Q. Wu, G, Farrell, "Strain sensor based on a pair of single-mode-multimode-single-mode fiber structures in a radiometric power measurement scheme," *Appl. Opt.*, Vol. 49, pp. 536-541, 2010.

3. S. Silva, O. Frazão, J. Viegas,L. A. Ferreira, F. M. Araújo, F. X. Malcata, J. L. Santos, "Temperature and strain independent curvature sensor based on a singlemode/ multimode fiber optic structure," *Meas. Sci. Technol.*, Vol. 22, pp. 085201, 2011.

4. Q. Wang, G. Farrell, "Multimode-fiber-based edge filter for optical wavelength measurement application and its design," *Microw. Opt. Technol. Lett.*, Vol. 48, pp. 900-902, 2006.

5. L. B. Soldano, E. C. M. Penning, "Optical multi-mode interference devices based on self-imaging: principles and applications," *J. Lightwave Technol.*, Vol. 13, pp. 615-627, 1995.

6. X. Zhou, K. Chen, X. Mao,W. Peng, Q. Yu, "A reflective fiber-optic refractive index sensor

based on multimode interference in a coreless silica fiber," Opt. Commun., Vol. 340, pp. 50-55, 2015.

7. Y. Zhao, L. Cai, X. Li Z. Zhao, "Investigation of the high sensitivity RI sensor based on SMS fiber structure," Sens. Actuators: A., Vol. 205, pp.186-190, 2014.

8. Y. Jung, S. Kim, D. Lee, K. Oh, "Compact three segmented multimode fibre modal interferometer for high sensitivity refractive-index measurement," Meas. Sci. Technol., Vol.17, pp. 1129-1133, 2006.

9. Q. Wu, Y. Semenova, P. Wang, G. Farrel, "High sensitivity SMS fiber structure based refractometer-analysis and experiment," Opt. Express., Vol. 19, pp. 7937-7944, 2011.

10. P. Wang, G. Brambilla, M. Ding,Y. Semenova, Q. Wu, "A high sensitivity, evanescent field refractometric sensor based on tapered multimode fiber interference," Opt. Lett., Vol. 36, pp. 2233-2235, 2011.

11. I. Del Villar, A. B. Socorro, J. M. Corres, F. J. Arregui, and I. R. Matias, "Refractometric sensors based on multimode interference in a thin-film coated singlemode–multimode–single-mode structure with reflection configuration," Appl. Optics., Vol. 53, pp. 3913-3919, 2014.

12. H. Fukano, Y. Kushida, and S. Taue, "Sensitivity improvement of optical-fiber temperature sensor with solid cladding material based on multimode interference," Jap. J. Appl. Physics., Vol. 54, pp. 032502-1 - 032502-5, 2015.

13. S. Silva, E. G. P. Pachon, M. A. R. Franco, J. G. Hayashi, F. X. Malcata, O. Frazão, P. Jorge, and C. M. B. Cordeiro, "Ultrahigh-sensitivity temperature fiber sensor based on multimode interference," Appl. Optics., Vol. 51, pp. 3236-3242, 2012.

14. H. Fukano, Y. Kushida, S. Taue "Multimode-interference structure optical-fiber temperature sensor with high sensitivity", Elect. Exp., Vol. 10, pp. 1-5, 2013.

15. Y. Li, H. Ma, G. Lin, Q. Liu, Z. Yan, D. Liu, O. Sun, "Immobilized optical fiber microprobe for selective and high sensitive glucose detection", Sens. Actuators: B, Vol. 255, pp. 3004-3010, 2018.

16. R. Ballerstadt, A. Polak, A. Beuhler, J. Frye, "In vitro long-term performance study of a near-infrared fluorescence affinity sensor for glucose monitoring," Biosens. Bioelectron, Vol. 19, pp. 905-914, 2004.

17. R. Esposito, B.D. Ventura, S.D. Nicola, C. Altucci, R. Velotta, D.G. Mita, M. Lepore, "Glucose sensing by time-resolved fluorescence of sol–gel immobilized glucose oxidase," Sensors,

Vol. 11, pp. 3483, 2011.

18. S. Sarika, D. Banshi, "Fabrication and characterization of a surface plasmon resonance based fiber optic sensor using gel entrapment technique for the detection of low glucose concentration," Sens. Actuators: B., Vol. 177, pp. 589-595, 2013.

19. A. Deep, U. Tiwari, P. Kumar, V. Mishra, J. Subhash, N. Singh, P. Kapur, L. Bharadwaj, "Immobilization of enzyme on long period grating fibers for sensitive glucose detection," Biosens. Bioelectron., Vol. 33, pp. 190-195, 2012.

20. B. Luo, Z. Yan, Z. Sun, J. Li, L. Zhang, "Novel glucose sensor based on enzyme-immobilized 81tilted fiber grating," Opt. Express, Vol. 22, pp. 30571-30578, 2014.

21. B. Jiang, K. Zhou, C. Wang, Q. Sun, G. Yin, Z. Tai, K. Wilson, J. Zhao, L. Zhang, "Label-free glucose biosensor based on enzymatic graphene oxide-functionalized tilted fiber grating," Sens. Actuators: B., Vol. 254, pp. 1033-1039, 2017.

22. J. E. Antonio-Lopez, A. Castillo-Guzman, D. A. May-Arrioja, R. Selvas-Aguilar, P. LiKamWa, "Tunable multimode-interference bandpass fiber filter," Opt. Lett., Vol. 35, pp. 324-326, 2010.

23. Y. Li, Z. Liu, S. Jian, "Multimode interference refractive index sensor based on coreless fiber," Photonics Sensors., Vol. 4, pp. 21-27, 2014.

24. Y. Raichlin, A. Katzir, "Fiber-Optic Evanescent Wave Spectroscopy in the Middle Infrared," App. Spectroscopy., Vol.62, pp. 55A-72A, 2008.

25. S. Novais, M. S. Ferreira, and J. L. Pinto, "Optical fiber Fabry–Perot tip sensor for detection of water–glycerin mixtures," J. Lightwave Technol., Vol. 36, pp. 1576-1582, 2018.

26. F. Chiavaioli, C. Gouveia, P. Jorge, F. baldini, "Towards a Uniform Metrological Assessment of Grating-Based Optical Fiber Sensors: From Refractometers to Biosensors", Biosensors., Vol. 7, 2017.

27. Y-J. Rao, "In-fibre Bragg grating sensors," Meas. Sci. Technol., Vol. 8, pp. 355-375, 1997.

VA - Additional Information

In this Section, more information is provided regarding the sensors chemical etching. The fiber sensors were subjected to wet chemical etching using a 40 % hydrofluoric acid (HF) solution. To obtain a structure with a nearly constant core diameter over its length, as well as a smooth surface, the HF solution was placed inside an ultrasound bath at room temperature. The reduction of the CSF diameter was observed after submerging the sample in liquid HF for a few minutes, removing it from the solution and cleaning it thoroughly with ethanol. A microscope image of the fiber tip was taken, to estimate its diameter. The sensing head was once again placed in the etching solution for a few additional minutes and the process was repeated. Figure V.9 (left) presents the microscope images taken at different times and Figure V.9 (right) shows the diameter variation with the etching time. The data was adjusted to a linear fitting and an etching rate of 1.63 μm/min was determined.

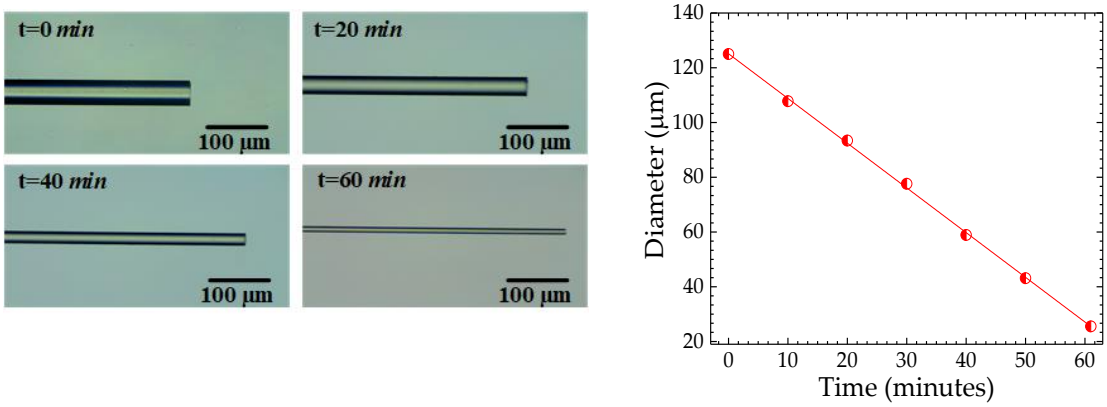

Figure V.9. Left: Microscope photos of CSF tip, at different etching times. Right: CSF diameter vs. time.

VI

Determination of thermo-optic coefficient of ethanol-water mixtures with optical fiber tip sensor

Published in Optical Fiber Technology, Vol. 45, pp. 276-279, August 3, 2018

DOI: 10.1016/j.yofte.2018.08.002

Determination of thermo-optic coefficient of ethanol-water mixtures with optical fiber tip sensor

Susana Novais, Marta S. Ferreira, João L. Pinto

Abstract: In this work, the thermo-optic coefficient (TOC) of ethanol-water mixtures, through refractive index and temperature measurements are determined using an etched optical fiber tip based on a multimode interferometer. The proposed probe is fabricated by fusion-splicing a 5.2 mm long coreless fiber section to a single mode fiber. To reduce the sensor dimensions and improve its sensitivity towards external medium variations, the fiber tip is subjected to wet chemical etching using a solution of 40% hydrofluoric acid, presenting a final diameter of 24.4 μm. The TOC of each solution is estimated and, in the case of deionized water and pure ethanol, its value is of -1.128×10^{-4} °C^{-1} and -3.117×10^{-4} °C^{-1}, respectively.

Keywords: Fiber optic sensors; interferometry; temperature; thermo-optic coefficient.

1. Introduction

The fact that ethanol is an element miscible in non-polar and polar substances makes the ethanol a versatile solvent used in several industrial sectors such as chemical, pharmaceutical or fuel. Due to the inevitable depletion of the world's petroleum supply (in the fuel sector), there is an increasing worldwide interest in alternative, non-petroleum-based sources of energy. In order to preserve the product quality, the water-ethanol proportion must be periodically monitored and compared to standardized conditions taking into account that the ethanol production process is characterized by sequential procedures, and in several cases the water is a constituent of the final product [1].

According Nish *et al*, the refractometric analysis of ethanol-water mixtures is hampered because this kind of mixtures presents deviations from a linear behavior, and the existence of anomalous physical-chemical properties. During the process of the mixture of water and ethanol the entropy of the system increases differently from that expected for an ideal solution of randomly mixed molecules. Thereby, the refractive index

of the ethanol-water mixture shows a non-linear dependence with the ethanol concentration, and it is expected that as the ethanol concentration rises beyond a critical value, the refractive index relation becomes a two-valued function, presenting an ambiguous region for the determination of the ethanol proportion in the mixture [2]. Nowadays, a huge variety of optical fiber sensors to determine the concentration in liquid mixtures has been suggested, since de concentration is correlated to the refractive index and temperature of the samples [3], and several methods have been used in the literature to study and measure water and ethanol mixtures.

The measurement of the refractive index dependence with temperature, at a given wavelength in liquid solutions (thermo-optic coefficient (TOC)) has attracted a lot of attention, due to its importance in chemical and bio-chemical analysis [4]. As for water-ethanol mixtures, due to the high TOC of ethanol, the temperature fluctuations contribute to the uncertainty in the refractive index measurements [5].

Several optical fiber-based configurations have been already proposed for the TOC determination, using etched fiber Bragg gratings [6,7], long period gratings (which have also demonstrated high sensitivity to the refractive index of surrounding medium) [8, 9], surface plasmon resonance effects [10], a two-mode interferometric probe based on a special fiber [4] and using a hollow core Fabry-Perot interferometer [11].

The use of coreless fiber has also been addressed for sensing applications, namely for high sensitivity refractive index [12] and temperature [13] measurements. The configurations reported are usually based on a transmission scheme, where the coreless fiber is spliced between two sections of single mode fiber [14]. The reflection scheme, where the coreless fiber tip is spliced to one section of single mode fiber, has also been proposed. Typically, a metal coating is applied to the sensor to increase its reflectivity and performance [15].

In this work, an etched coreless fiber tip is proposed for measurement of refractive index of ethanol aqueous mixtures as well as for the determination of their thermo-optic coefficient. The sensing device is previously calibrated using water-glycerin mixtures with

known refractive index at the 1550 nm wavelength range. The TOC for each solution is estimated through refractive index and temperature measurements.

2. Experimental results

The sensor head was obtained by fusion splicing a section of coreless fiber (with an initial diameter of 125 μm, supplied by Thorlabs) to standard single mode fiber (SMF), using the manual program of the splicing machine (Fujikura 62S). Afterwards, the fiber was cleaved, presenting a length of 5.2 mm. The tip was then subjected to wet chemical etching for 61 minutes, using a solution of 40% hydrofluoric acid. After the chemical etching procedure, the sensor presented a final length of 5.1 mm and a diameter of ~24.4 μm.

To determine the thermo-optic coefficient of ethanol-water mixtures, a set of 5 solutions with ethanol mass fractions ranging from 0 wt.% to 100 wt.% were prepared under a controlled laboratory environment. After stirring the solutions for 60 minutes with a magnetic stirrer (NAHITA, model no. 690/1), they were stored for 24 hours, to allow their stabilization. The sensing device was inserted vertically in the 5 different solutions with aid of capillary glass tube, to ensure the sensor robustness as well as the stability of the fiber. The spectral response of this sensing structure was observed in a typical reflection scheme, as shown in Figure VI.1. The experimental setup consisted on a broadband optical source, an optical spectrum analyzer (OSA Anritsu MS9740A) and the sensing head, connected by means of an optical circulator. The optical source was centered at 1570 nm, with a bandwidth of 80 nm. All readings were done with a resolution of 0.1 nm.

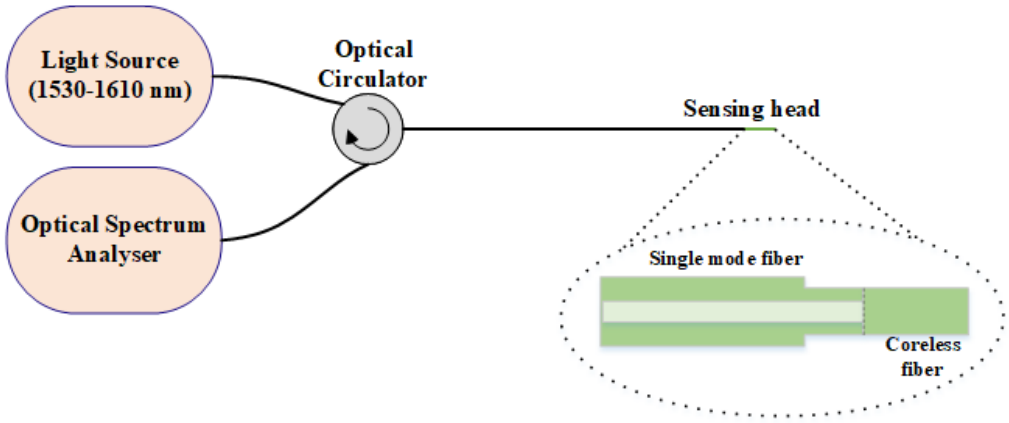

Figure VI.1. Scheme of the experimental setup.

When the light guided through the SMF enters the coreless fiber section, several modes are excited. These modes are reflected at the coreless fiber/surrounding medium interface, and recoupled to the SMF fundamental mode. The reflected wavelength, λ_0, can be tailored according to Eq. 1:

$$\lambda_0 = n_1 D^2 p / (2L), \quad (1)$$

where n_1, D, L and p are the coreless fiber refractive index, the fiber diameter, the length, and the interference order number, respectively [13]. For the present work, given the sensor dimensions and the reflected wavelength in air, p was estimated to be 19. According to the literature, the self-image of the multimode interferometer occurs at multiples of p = 4, and lower losses are obtained. However, at other interference order numbers (no self-image), two consecutive modes with high coupling efficiency can constructively interfere, originating a spectrum that is suitable to perform measurements. This sensor revealed to be adequate to perform high sensitivity measurements and it presented a fast response and high stability in the liquid media. The thinner the coreless fiber section, the larger the evanescent field in the sensing area, which interacts with the external medium. Therefore, a large sensitivity is expected, when compared to an unetched fiber section [13].

In Figure VI.2a) and VI.2b) it is possible to observe the spectra obtained at room temperature for each ethanol aqueous solution, and the wavelength shift dependence with the mass fraction for all solutions, respectively. The sensor response to temperature

and refractive index variations was determined by following the shift of the dip wavelength (located at ~1551 nm for pure deionized water). The decrease in the wavelength shift exhibited for 100 wt.% ethanol, evidenced in Figure VI.2b) is related to the decrease of the refractive index at that concentration.

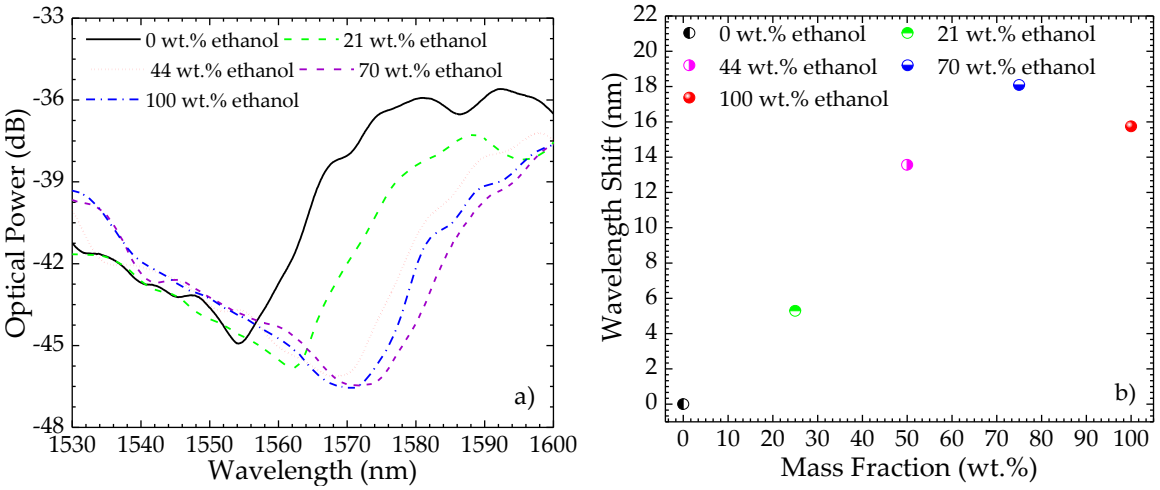

Figure VI.2. Fiber tip sensor a) spectra and b) wavelength shift, considering water-ethanol mixtures with different mass fractions.

The variation of mass fraction in a mixture of water and ethanol translates in a change of the medium refractive index. This parameter was determined for each solution and measured with an Abbe refractometer (Krüss optronic refractometer) operating at 589 nm. However, since the optical source was centered in the 1550 nm region, it was necessary to calibrate the sensor, thus estimating the refractive index of each solution in this wavelength range. This was achieved by placing the sensor in glycerin aqueous solutions that ranged from 0 wt.% to 51 wt.% glycerin, which were previously calibrated for the proper operation wavelength [16]. Figure VI.3 presents the wavelength shift dependence with the refractive index variations. As expected, a non-linear response is observed. Nevertheless, the behavior for the refractive index range between 1.315 RIU and 1.365 RIU, is approximately linear. The ethanol-water mixtures refractive index range is expected to be located within this region [5]. The sensor presented a linear sensitivity of 627.9 nm/RIU, with a fitting correlation factor of 0.994.

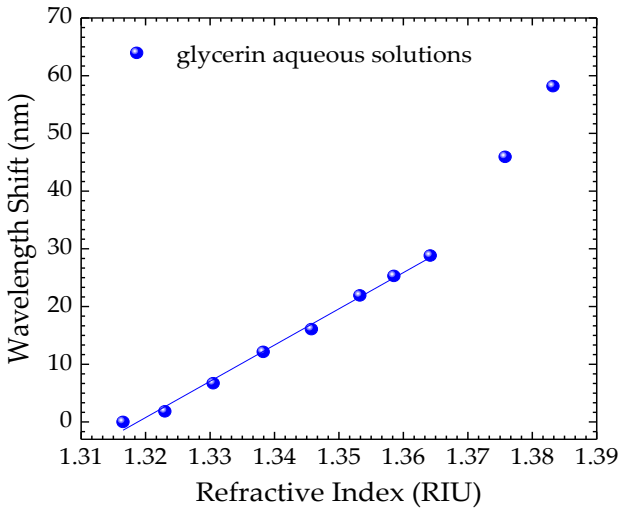

Figure VI.3. Sensor calibration to refractive index measurements: wavelength dependence with refractive index for glycerin-water mixtures.

Once the relationship between wavelength shift and refractive index was established, the sensor spectral response was evaluated for each water-ethanol solution. The correspondent refractive index was determined through the sensitivity obtained in the calibration procedure. Figure VI.4 presents the refractive index dependence with mass fraction for the ethanol-water mixtures, for the experimental (589 nm) and calibrated (1550 nm).

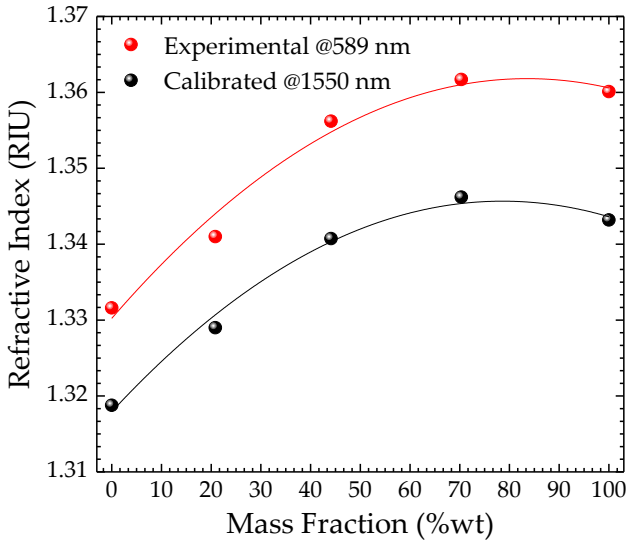

Figure VI.4. Refractive index dependence on mass fraction for ethanol-water mixtures, for two different wavelengths: 589 nm (experimental data) and 1550 nm (calibrated data).

As can be seen from the results when the ethanol mass fraction increases, the refractive index also increases, until a mass fraction of ~80% [17], after this value, there is a decrease of the refractive index. It is also possible to observe that the behavior is consistent for both wavelengths.

To perform the experiments, the sensor device was inserted vertically in the ethanol-water solutions which were placed in a temperature controlled hot plate (resolution of 0.1 °C) and subjected to temperature variations from 30 °C until 80 °C, with steps of 5 °C. Figure VI.5 presents the wavelength shift with temperature, for each solution. A shift towards shorter wavelengths (blue shift) with temperature increase is observed in all cases. On the other hand, it is observed that with the increase of ethanol mass fraction, the wavelength shift becomes more pronounced, which indicates that the sensor sensitivity also increases. Notice that the response is non-linear for the solutions with a mass fraction of 0 wt.%, 21 wt.%, and 44 wt.% ethanol. For higher concentrations, the behavior becomes linear. This is consistent with the behavior already reported in the literature [1, 5, 10].

To improve the TOC determination, the silica TOC and thermal expansion effects were compensated by performing temperature measurements in air, in the same wavelength range as for the liquids measurements. The sensor was placed in a thermal chamber (Model 340, Challenge Angelantoni Industry), and the readings were done with a resolution of 0.1 °C. Figure VI.5a) also shows the sensor response in air (red solid circles), from which a linear sensitivity, $\Delta\lambda_1/\Delta T = k_{T1}$=12.75 pm/°C was attained. On the other hand, when the sensor is placed in the liquid, the wavelength shift can be attributed to two components: one due to the coreless thermal expansion, k_{T1}, previously determined, and the other one due to the liquids TOC. The wavelength shift can be estimated through the expression $\Delta\lambda_2 = (k_{T1} + k_{T2})\Delta T$. Using the two equations, the sensitivity due to the liquid contribution can be determined through $\Delta\lambda_2 - \Delta\lambda_1 = k_{T2}\Delta T$. Figure VI.5b) presents the calculated wavelength shift due the liquids contribution.

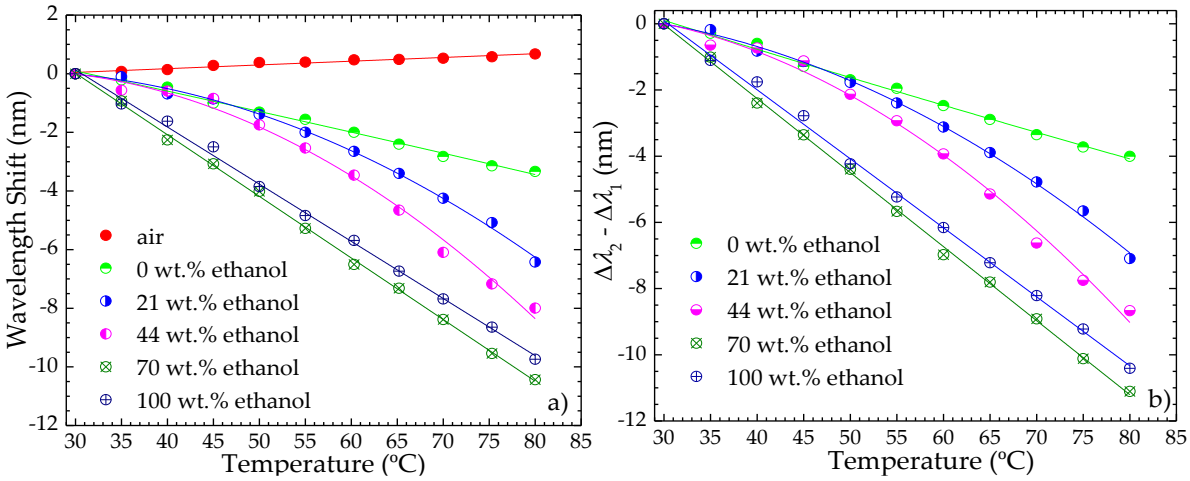

Figure VI.5. a) Wavelength shift dependence with temperature variations, b) calculated wavelength shift due the liquids contribution with temperature variations.

Table VI.1 summarizes the sensitivities to refractive index (k_n), and to temperature (either polynomial or linear fitting) attained for each solution, after compensating the effects due to the sensing head.

Table VI.1. Refractive index and temperature sensitivity for each solution. λ corresponds to the wavelength, in nm, and T to the temperature, in °C. The correlation coefficient, r^2 is also show.

$w_{ethanol}$ (wt.%)	k_n (nm/RIU)	*Polynomial and linear fitting*	r^2
0		$\Delta\lambda_2 - \Delta\lambda_1 = 8.699 \times 10^{-5}\, T^2 - 0.093\, T + 2.821$	0.995
21		$\Delta\lambda_2 - \Delta\lambda_1 = -0.002\, T^2 + 0.055\, T - 0.064$	0.998
44	627.93	$\Delta\lambda_2 - \Delta\lambda_1 = -0.002\, T^2 + 0.084\, T - 0.350$	0.993
70		$\Delta\lambda_2 - \Delta\lambda_1 = -0.224\, T + 6.689$	0.999
100		$D\lambda_2 - \Delta\lambda_1 = -0.209\, T + 6.348$	0.998

Taking into account the refractive index measurements made, it was possible to convert the wavelength shifts into refractive index, by using the expression $\Delta n = \Delta\lambda / k_n$. Thus, the refractive index dependence on temperature for each solution was obtained (Figure VI.6). The values were adjusted by a second-order polynomial fitting for the three solutions with smaller mass fraction, and by a linear fitting for the measurements of the last two solutions. The TOC coefficient was determined through the derivative of each fitting equation. The higher TOC obtained for the 70 wt.% solution when compared to the

TOC for pure ethanol can be due to the larger refractive index of the solution at that concentration. Notice that if one considers a linear fitting to the experimental data in the case of deionized water, as a first approximation, TOC of -1.128 × 10^{-4} °C^{-1} is determined. The TOCs obtained for pure deionized water and pure ethanol in our experiments are in good agreement with the values found in the literature for this wavelength range [6, 11]. To the best of our knowledge, there is no information in the literature regarding the TOC of water-ethanol mixtures in the wavelength range here studied. Table VI.2 reports the thermo-optic coefficient for each ethanol aqueous solution.

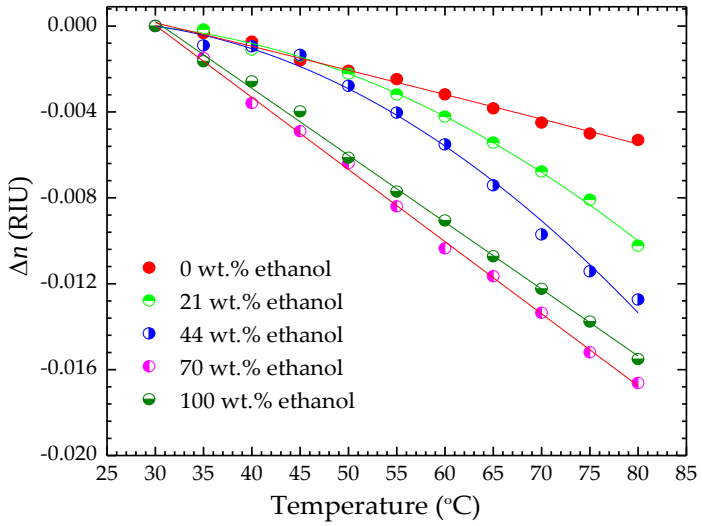

Figure VI.6. Refractive index shift dependence with temperature.

Table VI.2. Thermo-optic coefficient for each ethanol aqueous solution.

$w_{ethanol}$(wt.%)	dn/dT (TOC) °C^{-1}	r^2
0	$-1.543 \times 10^{-7}\ T - 1.044 \times 10^{-4}$	0.993
21	$-6.018 \times 10^{-6}\ T + 1.310 \times 10^{-4}$	0.997
44	$-8.089 \times 10^{-6}\ T + 1.777 \times 10^{-4}$	0.991
70	-3.358×10^{-4}	0.999
100	-3.117×10^{-4}	0.998

3. Conclusions

An etched coreless fiber tip multimode interferometer was proposed for the determination of the thermo-optic coefficient of water-ethanol mixtures. The sensing device was firstly calibrated using glycerin-water mixtures with refractive indices known in the 1550 nm region. A set of ethanol-water solutions was characterized using the proposed sensor, by varying the temperature in a range of ~60 °C. The response was determined by following the shift of the dip wavelength. A spectral blue shift was observed in all cases, which was mainly attributed to the liquid TOC. Through the relationship between refractive index and temperature, the TOC of each solution was determined. In the case of deionized water and pure ethanol, the estimated TOC value was of $-1.128 \times 10^{-4}\ °C^{-1}$ and $-3.117 \times 10^{-4}\ °C^{-1}$, respectively. Consistently, negative TOC values indicated decrease in refractive index with increasing temperature, which is in good agreement with the values found in the literature. It should be highlighted that the sensor was stable, did not require any coating to operate or any specially designed optical fiber, being an alternative solution to the sensing configurations proposed in the literature.

Acknowledgments: This work was supported by FEDER funds through the COMPETE 2020 Programme and National Funds through FCT-Portuguese Foundation for Science and Technology under the Project UID/CTM/50025/2013 and POCI-01-0145-FEDER-016414. Susana Novais and Marta S. Ferreira are grateful for the research fellowships no. BI/UI96/6643/2016, BI/UI96/6643/2018 and SFRH/BPD/124549/2016, respectively.

References

1. F. K. Coradin, G. R. C. Possetti, R. C. Kamikawachi, M. Muller, J. L. Fabris, Etched Fiber Bragg Gratings Sensors for Water-Ethanol Mixtures: a Comparative Study, Journal of Microwaves, Optoelectronics and Electromagnetic Applications 9, (2010), 131-143.

2. N. Nishi, S. Takahashi, M. Matsumoto, A. Tanaka, K. Muraya, Hydrogen bonding cluster formation and hydrophobic solute association in aqueous solution of ethanol, Journal of Physical Chemistry, 99, (1995), pp. 462-468.

3. C. B. Kim, C. B. Su, Measurement of the refractive index of liquids at 1.3 and 1.5 microns using a fibre optic Fresnel ratio meter, Meas. Sci. Technol. 15, (2004), pp. 1683-6.

4. Y. H. Kim, S. J. Park, S.-W. Jeon, S. Ju, C.S. Park, W.T. Han, and B. H. Lee, Thermo-optic coefficient measurement of liquids based on simultaneous temperature and refractive index sensing capability of a two-mode fiber interferometric probe, Opt. Express 20, (2012), pp. 23744-23754.

5. C. M. Hernández, O. R. Quiroz, D. M. Hernández, J. Villatoro, Contactless optical fiber interferometric sensor to monitor water content in ethanol, Sensors Journal, 18, (2018), pp. 3211-3217.

6. R. C. Kamikawachi, I. Abe, A. S. Paterno, H. J. Kalinowski, M. Muller, J. L. Pinto, and J. L. Fabris, Determination of thermo-optic coefficient in liquids with fiber Bragg grating refractometer, Opt. Commun. 281, (2008), pp. 621-625.

7. U. S. Raikar, V. K. Kulkari, A. S. Lalasangi, K. Madhav, and S. Asokan, Etched fiber Bragg grating as ethanol solution concentration sensor, Optoelectron. Adv. Mater, 1, (2007), pp. 149-151.

8. R. Falate, R.C. Kamikawachi, M. Muller, H.J. Kalinowski, J.L. Fabris, Fiber optic sensors for hydrocarbon detection, Sensors and Actuators B, 105, (2005), pp. 430-436.

9. G .R. C. Possetti, L. C. Côcco, C. I. Yamamoto, L. V. R. Arruda, R. Falate, M. Muller, J. L. Fabris, Application of a long-period fibre grating-based transducer in the fuel industry, Meas. Sci. Technol., 20, (2009), pp. 034012V-1-034012V-9.

10. S. K. Srivastava, R. Verma, B. D. Banshi, Surface plasmon resonance based fiber optic sensor for the detection of low water content in ethanol, Sens. Actuators B, Chem., 153, (2011), pp. 194-198.

11. C.L. Lee, H.-Y. Ho, J.H. Gu, T.Y. Yeh, and C.-H Tseng, Dual hollow core fiber-based Fabry–Perot interferometer for measuring the thermo-optic coefficients of liquids, Opt. Lett. 40, (2015), pp. 459-462.

12. I. Del Villar, A. B. Socorro, J. M. Corres, F. J. Arregui, and I. R. Matias, Refractometric sensors based on multimode interference in a thin-film coated singlemode–multimode–single-mode structure with reflection configuration, Appl. Optics 53, (2014), pp. 3913-3919.

13. H. Fukano, Y. Kushida, and S. Taue, Sensitivity improvement of optical-fiber temperature sensor with solid cladding material based on multimode interference, Jap. J. Appl. Physics 54, (2015), pp. 032502-1 - 032502-5.

14. S. Silva, E. G. P. Pachon, M. A. R. Franco, J. G. Hayashi, F. X. Malcata, O. Frazão, P. Jorge, and C. M. B. Cordeiro, Ultrahigh-sensitivity temperature fiber sensor based on multimode interference, Appl. Optics 51, (2012), pp. 3236-3242.

15. G. Zhou, Q. Wu, R. Kumar, W. P. Ng, H. Liu, L. Niu, N. Lalam, X. Yuan, Y. Semenova, G. Farrell, J. Yuan, C. Yu, J. Zeng, G. Y. Tian, and Y. Q. Fu, High sensitivity refractometer based on reflective SMF-small diameter no core fiber structure, Sensors 17, (2017), pp. 1415.

16. S. Novais, M. S. Ferreira, and J. L. Pinto, Optical fiber Fabry–Perot tip sensor for detection of water-glycerin mixtures, J. Lightwave Technol. 36, (2018), pp. 1576-1582.

17. David R. Lide, *Handbook of Chemistry and Physics*, CRC Press, 2004.

VII

Relative humidity fiber sensor based on multimode interferometer coated with agarose-gel

Published in Coatings, Vol. 8, pp. 453, December8, 2018

DOI: 10.3390/coatings8120453

Relative humidity fiber sensor based on multimode interferometer coated with agarose-gel

Susana Novais, Marta S. Ferreira, João L. Pinto

Abstract: In this work, a relative humidity (RH) sensor based on a structure with multimode interference is proposed and experimentally demonstrated. The multimode sensor is fabricated by fusion splicing a coreless fiber section to a single mode fiber. A hydrophilic agarose gel is coated on the coreless fiber, using the dip coating technique. By changing the surrounding RH, the refractive index of the coated agarose gel will change, causing a wavelength shift of the peak in the reflection spectra. For RH variations in the range between 60.0%RH and 98.5%RH, the sensor presents a maximum sensitivity of 44.2 pm/%RH, and taking in consideration the interrogation system, a resolution of 0.5%RH is acquired. This sensor has a great potential in real time RH monitoring and can be of interest for applications where a control of high levels of relative humidity is required.
Keywords: Fiber optics sensors; relative humidity; agarose gel.

1. Introduction

The measurement of relative humidity (RH) has shown significant importance in a large range of applications, such as bacterial growth, process control, product quality, food and beverage processing, automotive, and meteorological industries [1,2]. The measurement of relative humidity (RH) has shown to be of significant importance in a large range of applications, such as bacterial growth, process control, product quality, food and beverage processing, automotive, and meteorological industries [1,2].

Regarding sensing methods of RH, the optical fiber sensors, in comparison to their electronics counterparts, are preferred, considering their specific advantages, such as their minimal size and low weight, immunity to electromagnetic interference, corrosion resistance, and remote sensing capability [3]. There are basically two operating mechanisms for the fabrication of fiber optic RH sensors. One is based on using specific technologies to form porous sensing structures, such as sputtering [4], electro-spinning [5], electron evaporation [6], or layer-by-layer nano-assembly [7,8]. The other type of RH

fiber optic sensors involves using humidity sensitive coatings or gels (hydrophilic materials) on the surface or end face of the optical fiber, such as polyvinyl alcohol [9,10], polyethylene glycol [11], chitosan [12,13], polyethylene oxide [14], graphene oxide [15], metallic oxide film [15,16], agar [17–20] and indium tin oxide [21,22]. This kind of polymer coatings have advantages of good performance [19], reproducibility, and long-term stability [14]. The hydrophilic materials normally swell physically and experience a refractive index change in response to change in RH.

Different fiber sensing structures have been combined with polymer coatings. For instance, the use of fiber Bragg gratings [23], bended fibers [24], side-polished fibers [25,26], photonic crystal fibers [20,27], tapered fibers [13,15,16], Fabry-Perot cavities [28], Sagnac interferometers [29], hollow core fibers [15], and single-mode hetero-core fibers [14,30] have been proposed to detect environmental RH variations.

Agarose is considered a biopolymer, originated from a marine alga (Gracilaria Verrucosa), whose use is commonly extended in the field of biochemistry for separation of DNA chains [31,32]. The agarose gel is considered a material with desirable humid sensitivity, able to readily absorb and desorb water, and also to restore a fast equilibrium with atmospheric humidity. Besides that, it is extremely stable, not soluble in water and can be easily handled for device manufacture [23,31].

In this work, a multimode interferometer based on a coreless fiber coated with agarose gel is proposed for the detection of RH. The sensor is easy to produce, presents good resolution, particularly for environments with values of RH higher than 60.0%RH.

2. Sensor fabrication and operation principle

The fabrication of the coated sensor, whose scheme is shown in Figure VII.1, involved two steps. The first step consisted on splicing a short section of coreless silica fiber (CSF, supplied by Thorlabs, Newton, NJ, USA) to single mode fiber (SMF 28e, supplied by Thorlabs, Newton, NJ, USA), using the manual mode program of the splicing machine

(Fujikura 40 S, Tokyo, Japan). The second step consisted in functionalizing the sensor with agarose gel, through dip coating technique.

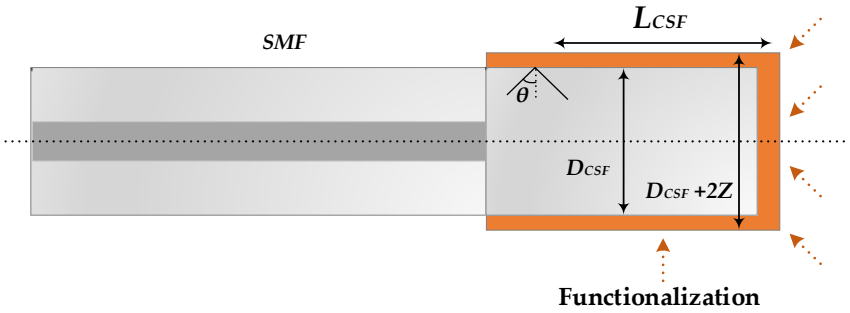

Figure VII.1. Schematic diagram of the sensor structure.

When the incident light comes from the SMF to the CSF, the high-order modes are excited and propagate within the CSF. These excited modes interfere with one another as they propagate along whole CSF length, giving rise to a multimode interference (MMI). According to Eq. 1, the interference wavelength, λ_0, can be expressed by [33]:

$$\lambda_0 = \frac{n_1 D_{CSF}^2}{2L_{CSF}} p, \tag{1}$$

where D_{CSF}, L_{CSF}, n_1 and p are the CSF diameter, length, refractive index, and interference number, respectively. The length and diameter of the CSF used in this work were ~30 mm and 125 μm, respectively. Considering the refractive index to be 1.444 and the operation wavelength in air of ~1530 nm, p was estimated to be 4.

Taking into account Eq. 1, there is no apparent dependence of the wavelength with the external medium. However, if one considers the evanescent field produced at the CSF/external medium interface, the diameter can be considered as an effective value of $D_{CSF} + 2Z$, where Z is the penetration depth. This parameter can be calculated through Eq. 2 [34]:

$$Z = \frac{\lambda_0}{2\pi n_1 \sqrt{\sin^2\theta - (n_s / n_1)^2}}, \tag{2}$$

where n_s is the surrounding medium refractive index and θ is the incident angle at the CSF/surrounding medium interface, as shown in Figure VII.1. Since the effective

refractive index of the agarose gel changes with the ambient relative humidity, as the environmental refractive index changes, the propagation constants for each guided mode within the CSF will change too, which leads to shifts in the output spectra [32, 35].

2.1. Agarose gel coating

The agarose solution was prepared by dissolving 0.9 g of agarose (Fisher Scientific, BP160-100) in 60 mL of distilled water, corresponding to a proportion of 1.5 wt.%. The solution was then heated up to 65 °C and a magnetic stirrer was used to dissolve the agarose in distilled water.

The sensing head was inserted in a silica capillary to ensure that the fiber was straight and stable (Figure VII.2). The sensor was dipped into the hot agarose solution and pulled out very fast, by moving the horizontal platform downwards. When the agarose solution cools down and reaches room temperature, it polymerizes to form hydrogel and will not assume a liquid form again unless it is heated above the melting point. The coated sensor was left to dry for 48 h at room temperature.

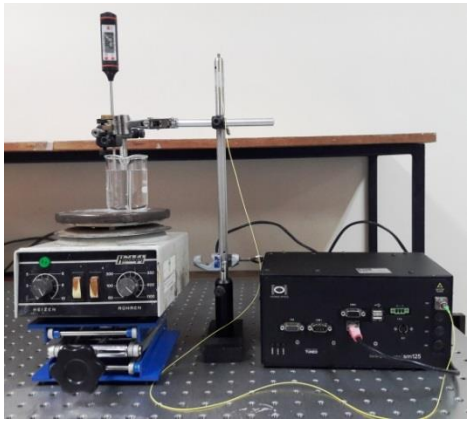

Figure VII.2. Photograph of the experimental setup for agarose deposition.

The agarose curing process was monitored with an optical interrogator (sm125, Micron Optics Inc., Atlanta, GA, USA, operating at 2.0 Hz). The response was obtained in a spectral range between 1530 and 1570 nm, immediately after removing the sensor from the agarose solution. This experiment was carried out in a controlled environment, with a room temperature of 25 °C. As shown in the Figure VII.3, there is a higher wavelength

shift in the first five minutes. From that moment on until 30 minutes, there is a smaller wavelength variation, which tends to stabilize after that time.

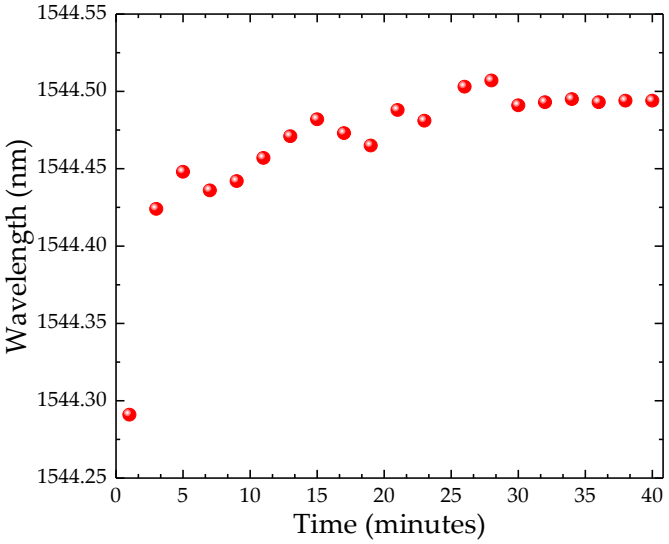

Figure VII.3. Peak wavelength dependence with time during the agarose curing process.

Figure VII.4 shows the spectra for the sensor with agarose coating (black solid line) and without coating (red dashed line). A spectral red shift was observed in the reflection spectrum of the device compared with its initial spectrum as shown in Figure VII.4. The shift in wavelength peak after coating is about 3.59 nm.

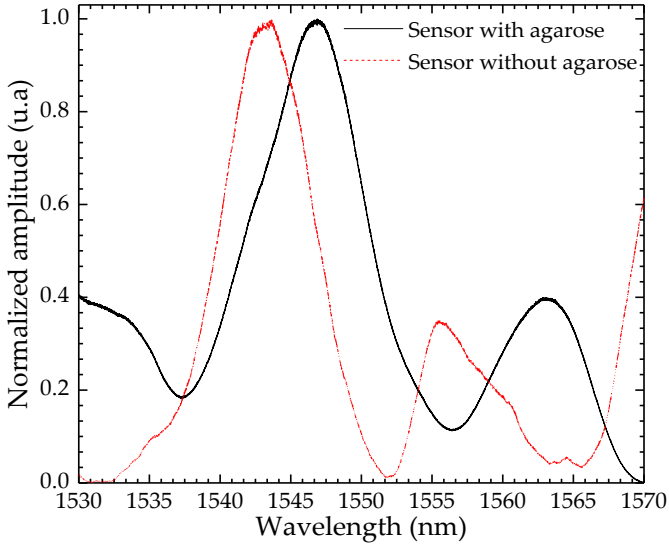

Figure VII.4. The wavelength peak before and after coating.

3. Experimental setup

Two sensing heads, one uncoated and the other coated with agarose gel, with similar lengths (28.8 mm), were introduced in a thermal chamber (model Challenge 340, from Angelantoni Industrie, Cimacolle, Italy), and subjected to variations of relative humidity and temperature. The experiments in the thermal chamber were carried out simultaneously, to ensure that the sensors were exposed to the same environmental changes. This thermal chamber is equipped with a humidification–dehumidification system and a cooling–heating system that can change both RH and temperature in a controlled way. The optical fiber connector was preserved outside the thermal chamber and the reflection spectra were monitored using the interrogator sm125-500, Micron Optics Inc., operating at 2.0 Hz and wavelength accuracy of 1.0 pm.

The RH experiments were carried out by keeping the temperature constant at 25 °C and by varying the RH between 20.0% and 98.5%RH, while the temperature measurements were done with a constant RH of 60.0%RH and a temperature variation between 10 and 70 °C. After each change in the parameters, a period of 30 min was allowed for the thermal chamber to stabilize. Figure VII.5 shows the scheme of the experimental setup for the characterization of the sensors.

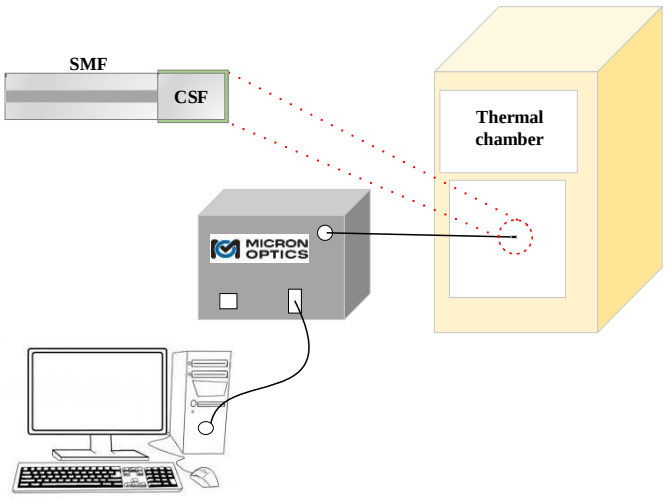

Figure VII.5. Experimental setup for the characterization of the sensors.

4. Discussion

Figure VII.6 shows the wavelength shift dependence on the relative humidity for both sensors. As expected, the uncoated sensing head revealed to be insensitive to the RH variations. Although the refractive index of air depends on the RH [36], the variation is lower than the resolution of the proposed sensor, compromising its response. A linear fitting was adjusted to the experimental data, and a sensitivity of 0.9 pm/%RH was attained. On the other hand, the coated sensor presented a non-linear wavelength shift towards longer wavelengths (red shift) with the external RH variations, which is more prominent for higher values of RH. This non-linear behavior has already been observed for this type of multimode interferometer sensors when subjected to refractive index variations [35], being related to the increase of the agarose gel refractive index with RH.

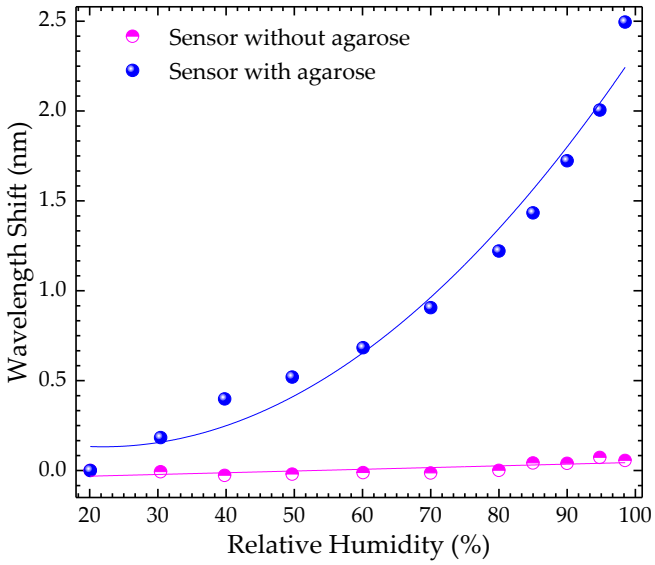

Figure VII.6. Measured wavelength shift dependence with relative humidity (RH), considering both sensors.

Two different linear regions were considered to estimate the coated sensor sensitivity. The first region, for lower RH variations, ranges from 20.0% to 50.0%RH, whereas the second region, for higher RH variations ranges from 60.0% up to 98.5%RH. The sensitivities attained were of 18.6 pm/%RH (r^2 = 0.988) and 44.2 pm/%RH (r^2 = 0.922), for the first and second regions, respectively.

The temperature responses of the sensors without and with agarose were measured using the same interrogation scheme as shown in Figure VII.5. The temperature was raised in steps of 10 °C, from 10 up to 70 °C and RH was fixed to 60.0%RH. The response, shown in Figure VII.7, was linear in both cases. However, there was a drop in the sensitivity, from 13.6 pm/°C (uncoated sensor) to 7.8 pm/°C for the coated sensor. The sensor with agarose became approximately 2× less sensitive than the sensor without agarose. The cross-sensitivity between RH and temperature, for the coated sensor, was determined to be 0.2 RH/°C.

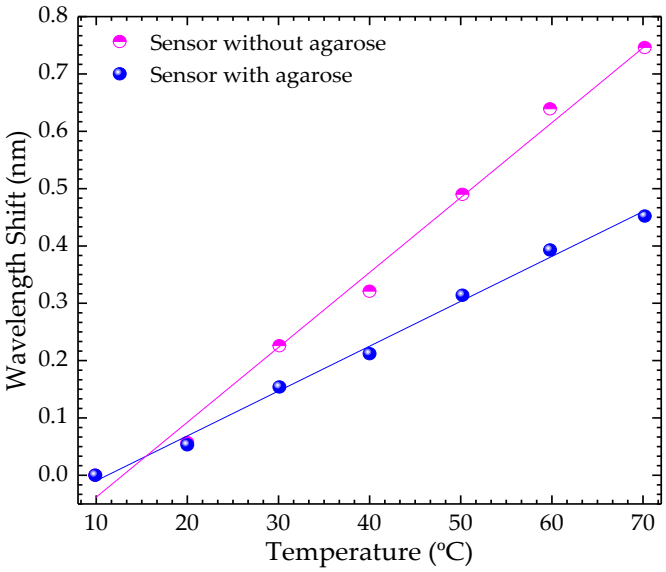

Figure VII.7. Response of the uncoated and coated sensors to the temperature variations.

The coated sensor response time was evaluated through monitoring, in real time, the response when the RH of the thermal chamber was changed from 60% to 80% (Figure VII.8). Although the response time of the sensor is of ~1 min, it is prudent to wait at least for 5 min for the signal stabilization. This period is also related to the stabilization of the thermal chamber.

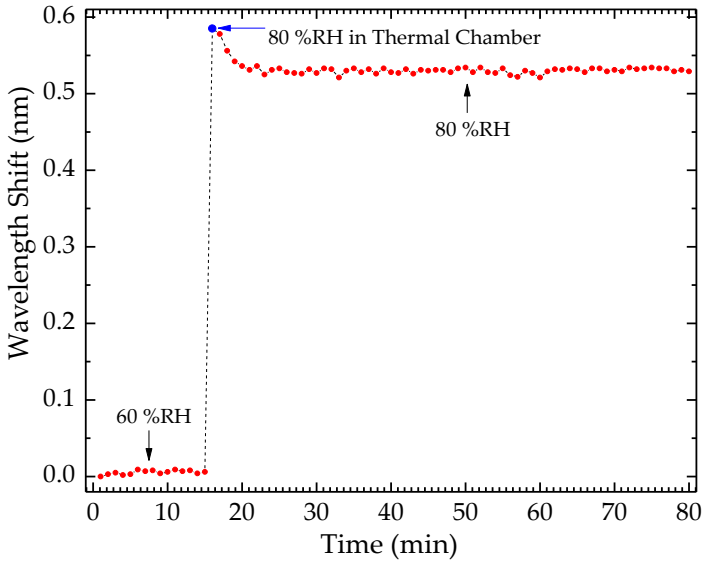

Figure VII.8. Response time of the sensor when subjected to a step humidity change from 60% to 80%.

With reference to the stability of the projected sensor, preliminary tests were also carried out. In the future, long-term and repeatability experiments will be performed to investigate the sensor stability. The coated sensor was placed in the thermal chamber at a constant RH and temperature of 60.0%RH and 25 °C, respectively. The peak wavelength was monitored during 120 min and the spectra were acquired once per 2 min. The same procedure was followed for a RH of 70.0%RH and 90%RH. The results are shown in Figure VII.9. For the first step, a mean wavelength of 1545.08 nm was determined, with a standard deviation of 4.7 pm. Regarding the second and third steps, the mean wavelength were of 1545.29 nm and 1546.11 nm, with a standard deviation of 5.1 pm and 4.1 pm, respectively. It should be highlighted that during the experiment, a temperature oscillation of 0.2 °C occurred in the thermal chamber, which might have also influenced the sensor response.

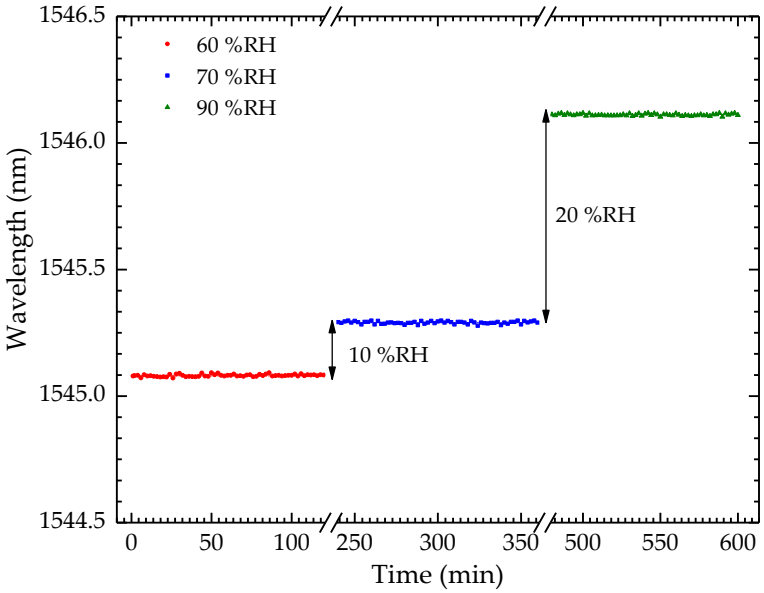

Figure VII.9. Step technique to estimate the resolution of the humidity sensor.

The minimum value of humidity, δ_{RH} that the sensor is able to discriminate is given by Equation (3) [37]:

$$\delta_{RH} = 2\frac{\sigma_{\lambda}\Delta RH}{\Delta\lambda} \quad (1)$$

where σ_{λ} is the maximum standard deviation of λ for both values of RH, and ΔRH and $\Delta\lambda$ are the variation of RH and the mean wavelength shift between the two steps, respectively. By applying Equation (3), a resolution of 0.5%RH was obtained, considering the sensor operation in the higher RH region. It is important to note that this value is also influenced by the spectral resolution of the equipment used for data acquisition (in this case, of 1.0 pm).

5. Conclusions

A relative humidity (RH) sensor based on multimode interference fiber structure, coated with hydrophilic agarose gel was proposed. For comparison purposes, both an uncoated sensing structure and a coated one were subjected to the same experiments. As expected, the uncoated sensor was insensitive to the environmental RH changes. On the other hand, the sensor with agarose gel exhibited a maximum sensitivity of 44.2 pm/%RH

with a resolution of 0.5%RH. The proposed sensor has a great potential in real time RH monitoring, particularly in environments with high percentages of relative humidity. One example of such applications are the lodges where Madeira wine is stored for ageing, where the RH is usually in the range between 65.0%RH–75.0%RH. However, the environment should be carefully controlled to ensure the desired quality of the product. The proposed sensor presented low manufacturing cost and easy fabrication, being an alternative to other sensors.

Author Contributions: Conceptualization, S.N. and M.S.F.; Methodology, S.N. and M.S.F.; Software, S.N.; Validation, S.N.; Formal Analysis, S.N.; Investigation, S.N. and M.S.F.; Data Curation, S.N.; Writing-Original Draft Preparation, S.N.; Writing-Review & Editing, S.N., M.S.F. and J.L.P.; Visualization S.N., M.S.F. and J.L.P.; Supervision, M.S.F and J.L.P.; Project Administration, J.L.P.; Funding Acquisition, J.L.P.

Funding: This research was funded by ERDF funds through the Regional Operational Program of the Center and National Funds through FCT (Fundação para a Ciência e Tecnologia) under the AROMA project (CENTRO-01-0145-FEDER-031568) and by Project POCI-01-0145-FEDER-016414 PAC, cofinanced by Programa Operacional Competitividade e Internacionalização and Programa Operacional Regional de Lisboa, through the COMPETE 2020 Programme and National Funds through FCT, grant numbers BI/UI96/6643/2018 and SFRH/BPD/124549/2016.

Conflicts of Interest: The authors declare no conflict of interest.

References

1. Zhang, Z. F., Zhang, Y. Humidity sensor based on optical fiber attached with hydrogel spheres. Opt. Laser Technol 2015, Volume 74, pp. 16–19, DOI:10.1016/j.optlastec.2015.05.006.
2. Torres, D. L.; Elousa, C.; Villatoro, J.; Zubiac, J.; Rothhardt, M.; Schuster, K.; Arregui, F. J. Enhancing sensitivity of photonic crystal fiber interferometric humidity sensor by the thickness of SnO2 thin films, Sens. Actuators B: Chem 2017, Volume 251, pp. 1059–1067, DOI:10.1016/j.snb.2017.05.125.
3. Zhao, Z.; Duan, Y. A low cost fiber-optic humidity sensor based on silica sol–gel film, Sens. Actuators B: Chem 2011, Volume 160, pp. 1340–1345, DOI: 10.1016/j.snb.2011.09.072.

4. Sigmund, P. Elements of sputtering theory, in nanofabrication by ion-beam sputtering: Fundamentals and applications. Singapore: Pan Stanford 2012, pp. 1–40, DOI: 10.4032/9789814303767, ISBN: 9789814303750.

5. Urrutia, A.; Goicoechea, J.; Rivero, P. J.; Matías, I. R.; Arregui, F. J. Electrospun nanofiber mats for evanescent optical fiber sensors, Sens. Actuators B: Chem 2013, Volume 176, pp. 569–576. DOI:10.1016/j.snb.2012.10.009.

6. Yang, M.; Xie, W.; Dai, Y.; Lee, D.; Dai, J.; Zhang, Y.; Zhuang, Z. Dielectric multilayer-based fiber optic sensor enabling simultaneous measurement of humidity and temperature, Opt. Exp., 2014, Volume 22, no.10, pp. 11892–11899, DOI: 10.1364/OE.22.011892.

7. Consales, M.; Berruti, G.; Borriello, A.; Giordano, M.; Buontempo, S.; Breglio, G.; Makovec, A.; Petagna, P.; Cusano, A. Nanoscale TiO2-coated LPGs as radiation-tolerant humidity sensors for high-energy physics applications, Opt. Lett 2014, Volume 39, no. 14, pp. 4128–4131, DOI: 10.1364/OL.39.004128.

8. Urrutia, A.; Goicoechea, J.; Ricchiuti, A. L.; Barrera, D.; Sals, S.; Arregui, F. J. Simultaneous measurement of humidity and temperature based on a partially coated optical fiber long period grating, Sens. Actuators B: Chem 2016, Volume 227, pp. 135–141, DOI: 10.1016/j.snb.2015.12.031.

9. Yan, G.; Liang, Y.; Lee, E. H.; He, S. Novel knob-integrated fiber Bragg grating sensor with polyvinyl alcohol coating for simultaneous relative humidity and temperature measurement, Opt. Exp 2015, Volume 23, no. 12, pp. 15624–15634, DOI: 10.1364/OE.23.015624.

10. Sun, H.; Yang, Z.; Zhou, L.; Liu, N.; Gang, T.; Qiao, X.; Hu, M. A relative humidity sensing probe based on etched thin-core fiber coated with polyvinyl alcohol, Opt. Commun 2015, Volume 356, no. 8, pp. 556-559, DOI: 10.1016/j.optcom.2015.08.058.

11. Acikgoz, S.; Bilen, B.; Demir, M. M.; Menceloglu, Y. Z.; Skarlatos, Y.; Aktas, G.; Inci, M. N. Use of polyethylene glycol coatings for optical fiber humidity sensing, Opt. Rev. 2008, Volume 15, pp. 84–90, DOI: 10.1007/s10043-008-0012-1.

12. Voznesenskiy, S. S.; Sergeev, A. A.; Mironenko, A. Y.; Bratskaya, S. Y.; Kulchin, Y. N. Integrated-optical sensors based on chitosan waveguide films for relative humidity measurements, Sens. Actuators B: Chem 2013, Volume 188, no. 11, pp. 482–487, DOI: 10.1016/j.snb.2013.07.043.

13. Chen, L. H.; Chan, C. C.; Menos, R.; Balamurali, P.; Shailender, M.; Neu, B.; Ang, X. M.; Zu, P.; Wong, W. C.; Leong, K. C. Fabry–Perot humidity sensor, Sens. Actuators B: Chem 2012, Volume 169, no. 8, pp. 167–172, DOI: 10.1016/j.snb.2012.04.052.

14. Wu, Q.; Semennova, Y.; Mathew, J.; Wang, P.; Farrell, G. Humidity sensor based on a single mode hetero-core fiber structure. Opt. Lett. 2011, Volume 36, pp. 1752–1754, DOI: 10.1364/OL.36.001752.

15. Gao, R.; Lu, D.; Cheng, J.; Jiang, Y.; Jiang, L.; Qi, Z. Humidity sensor based on power leakage at resonance wavelengths of a hollow core fiber coated with reduced graphene oxide. Sens. Actuators B: Chem 2016, Volume 222, pp. 618–624, DOI: 10.1016/j.snb.2015.08.108.

16. Liu, H.; Miao, Y.; Liu, B.; Lin, W.; Zhang, H.; Song, B.; Huang, M.; Lin, L. Relative Humidity Sensor Based on S-Taper Fiber Coated with SiO2 Nanoparticles. IEEE Sens. J. 2015, Volume 15, pp. 3424–3428, DOI: 10.1109/JSEN.2015.2389519.

17. Huang, C.; Xie, W.; Yang, M.; Dai, J.; Zhang, B. Optical Fiber Fabry-Perot Humidity Sensor Based on Porous Al2O3 Film. IEEE Photonics Technol. Lett. 2015, Volume 27, pp. 2127–2130, DOI:10.1109/LPT.2015.2454271.

18. Mathew, J.; Semenova, Y.; Farrell, G. Effect of coating thickness on the sensitivity of a humidity sensor based on an Agarose coated photonic crystal fiber interferometer, Opt. Exp. 2013, Volume 21, no. 5, pp. 6313–6320, DOI: 10.1364/OE.21.006313.

19. Bariáin, C.; Matías, I. R.; Arregui, F. J.; López-Amo, M. Optical fiber humidity sensor based on a tapered fiber coated with agarose gel, Sens. Actuators B: Chem 2000, Volume 69, no. 1-2, pp. 127–131, DOI: 10.1016/S0925-4005(00)00524-4.

20. Mathew, J.; Semenova, Y.; Farrell, G. Relative humidity sensor based on an agarose-infiltrated photonic crystal fiber interferometer, IEEE J. Sel. Topics Quantum Electron, 2012, Volume 18, no. 5, pp. 1553–1559, DOI: 10.1109/JSTQE.2011.2182337.

21. Del Villar, I., Socorro, A. B.; Corres, J. M.; Arregui, F. J.; Matias, I. R. Refractometric sensors based on multimode interference in a thin-film coated singlemode–multimode–single-mode structure with reflection configuration, Applied Optics, 2014, Volume 53, no. 18, pp. 3913–3919, DOI: 10.1364/AO.53.003913.

22. Cardona-Maya, Y. C.; Del Villar, I.; Socorro, A. B.; Corres, J. M.; Matias, I. R.; Botero-Cadavid, J. F. Wavelength and phase detection based SMS fiber sensors optimized with etching and nanodeposition, J. Lightwave Techn, 2017, Volume 35, no. 17, pp. 3743–3749, DOI: 10.1109/JLT.2017.2719923.

23. Lee, C. L.; You, Y. W.; Dai, J. H.; Hsu, J. M.; Horng, J. S. Hygroscopic polymer microcavity fiber Fizeau interferometer incorporating a fiber Bragg grating for simultaneously sensing humidity and temperature, Sens. Actuators B: Chem 2016, Volume 222, pp. 339–346, DOI: 10.1016/j.snb.2015.08.086.

24. Mathew, J.; Semenova, Y.; Rajan, G.; Wang, P.; Farrell, G. Improving the sensitivity of a humidity sensor based on fiber bend coated with a hygroscopic coating, Opt. Laser Technol. 2011, Volume 43, no. 7, pp. 1301–1305, DOI: 10.1016/j.optlastec.2011.03.028.

25. Wang, X. F.; Farrell, G.; Lewis, E.; Tian, K.; Yuan, L. B.; Wang, P. F. A humidity sensor based on a singlemode-side polished multimode–singlemode optical fibre structure coated with gelatin. J. Lightwave Technol. 2017, Volume 35, pp. 4087–4094, DOI: 10.1109/JLT.2017.2730484.

26. Alvarez-Herrero, A.; Guerrero, H.; Levy, D. High-sensitivity sensor of low relative humidity based on overlay on side-polished fibers, IEEE Sens J. 2004, Volume 4, no. 1, pp. 52–56, DOI: 10.1109/JSEN.2003.822214.

27. Mathew, J.; Semenova, Y.; Farrell, G. Experimental demonstration of a high-sensitivity humidity sensor based on an Agarose-coated transmission-type photonic crystal fiber interferometer. Appl. Opt. 2013, Volume 52, pp. 3884–3890, DOI:10.1364/AO.52.003884.

28. Consales, M.; Buosciolo, A.; Breglio, G.; Irace, A.; Buontempo, S.; Petagna, P.; Giordano, M.; Cusano, A. Fiber optic humidity sensors for high energy physics applications at CERN, Sens. Actuators B: Chem 2011, Volume 159, no. 1, pp. 66–74, DOI: 10.1016/j.snb.2011.06.042.

29. Chen, L. H.; Chan, C. C.; Li, T.; Shaillender, M.; Neu, B.; Balamurali, P.; Menon, R.; Zu, P.; Ang, X.; Wong, W. C.; Poh, L. C.; Leong, C. K. Chitosan-coated polarization maintaining fiber based Sagnac interferometer for relative humidity measurement, IEEE J. Sel. Topics Quantum Electron, 2012, Volume 18, no. 5, pp. 1597–1604, DOI: 10.1109/JSTQE.2012.2194729.

30. Akita, S.; Sasaki, H.; Watanabe, K.; Seki, A. A humidity sensor based on a hetero-core optical fiber. Sens. Actuators B: Chem 2010, Volume 147, pp. 385–391, DOI:10.1016/j.snb.2010.03.049.

31. Xu, W.; Shi, J.; Yang, X.; Xu, D.; Rong, F.; Zhao, J.; Yao, J. Relative humidity sensor based on no-core fiber coated by agarose-gel film, Sensors 2017, Volume 17, pp. 2353; DOI:10.3390/s17102353.

32. Gounaridis, L.; Groumas, P.; Schreuder, E.; Heideman, R.; Avramopoulos, H.; Kouloumentas, C. New set of design rules for resonant refractive index sensors enabled by FFT based processing of the measurement data, Opt. Exp. 2016, Volume 24, no. 7, pp. 7611–7632, DOI: 10.1364/OE.24.007611.

33. Lopez, J. E.; Guzman, A.; Arrioja, D. A.; Aguilar, R.; LiKamWa, P. Tunable multimode interference bandpass fiber filter, Opt. Lett. 2010, Volume 35, pp. 324–326, DOI: 10.1364/OL.35.000324.

34. Fukano, H.; Kushida, Y.; Taue, S. Sensitivity improvement of optical-fiber temperature sensor with solid cladding material based on multimode interference, Jap. J. Appl. Phys. 2015, Volume 54, DOI: 10.7567/JJAP.54.032502.

35. Novais, S.; Ferreira, M. S.; Pinto, J. L. Optical fiber tip sensor for the measurement of glucose aqueous solutions, Photonics Journal, 2018, Volume 10, no. 5, DOI: 10.1109/JPHOT.2018.2869944.

36. Ciddor, P. E. Refractive index of air: new equations for the visible and near infrared, Appl. Optics, 1998, Volume 35, no. 9, DOI: 10.1364/AO.35.001566.

37. Romero, R., Frazão, O., Pereira, D. A., Salgado, H. M., Araujo, F. M.; Ferreira, L. A. Intensity-referenced and temperature-independent curvature-sensing concept based on chirped fiber Bragg gratings, Appl. Optics, 2005, Volume 44 (18), pp. 3821–3826, DOI: 10.1364/AO.44.003821.

VIIA - Additional Information

In parallel with the above work, a new RH sensor based on a Fabry-Perot (FP) interferometer and coated with agarose was developed and experimentally demonstrated. The preliminary results here presented will be completed in the near future and a Journal paper is expected to be published.

The sensor is fabricated by producing an air bubble in multimode fiber and reshaping the tip in order to produce a thin silica diaphragm (Figure VII.10), following the procedures described in Chapter IV. The proposed sensor contains three reflection mirrors, M_1, M_2, M_3, that will create a 3-wave interferometer. The first cavity results from the reflections occurring between M_1 and M_2. The second cavity corresponds to the diaphragm formed between M_2 and the MMF end face with agarose, M_3. The third cavity results from the combination between two previous cavities.

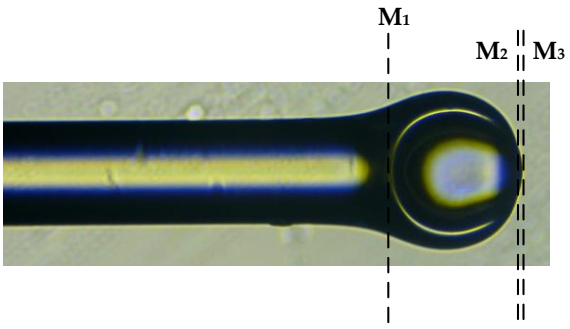

Figure VII.10. Scheme of the fiber tip FP sensor, where M_1, M_2, M_3 correspond to the sensor mirrors.

With this structure, the swelling effect of agarose can be fully utilized for RH detection. The refractive index of agarose exhibits a linear increase with the increase of ambient RH level [38]. The thickness of agar film, expands when environmental RH increases, exhibiting a good linearity based on [18-20]. This will cause a change in the second cavity length, translating in a wavelength shift. As the layer becomes thicker, the RH sensitivity can be greatly enhanced. The interference spectrum of the FPI with different coating layers is shown in Figure VII.11.

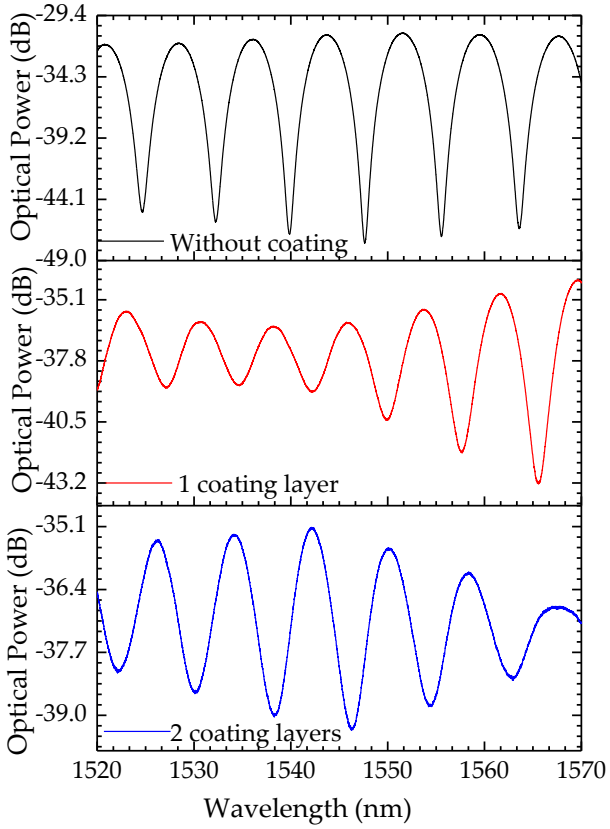

Figure VII.11. The interference spectrum of the FP interferometer with different coating layers.

The sensor head with an air cavity length of the 155.6 μm, was introduced in a thermal chamber, and subjected to variations of relative humidity and temperature. The experimental setup used was similar to the one described in Section 3. To investigate the effect of coating layers, the same sensor was coated 2 times. The RH was varied between 20-80%, keeping the temperature constant at 25 °C, and the spectral changes were evaluated for each step. The experiments were repeated using the sensor with no coating, with one layer, and with two layers of agarose. Figure VII.12 shows the wavelength shift dependence on the RH. As expected, the uncoated sensing head revealed to be insensitive to the RH variations. On the other hand, the coated sensor presents a linear response towards longer wavelengths (red shift). Furthermore, as the number of agarose layers increases, the sensitivity of the sensor also increases. The sensitivity attained for the sensor with one coating layer was of 11.15 pm/%RH ($r^2 = 0.985$), and for the two coating layers, was of 33.45 pm/%RH ($r^2 = 0.997$), i.e. the sensitivity has doubled.

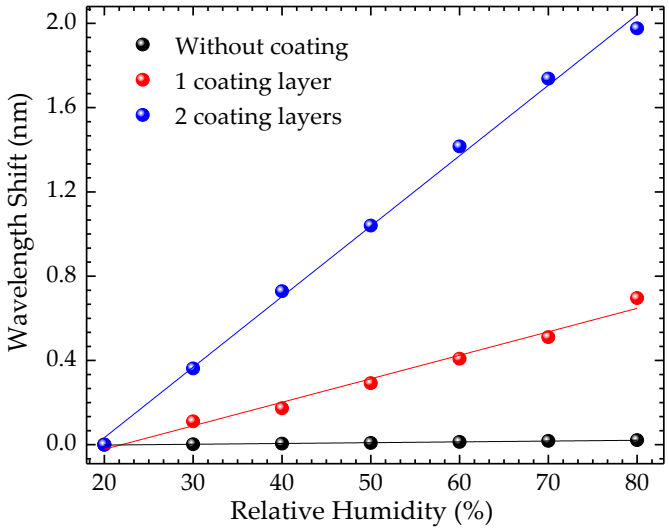

Figure VII.12. RH response of the sensor with a different number of agarose gel layers.

The temperature response of the sensor was evaluated in the range between 10 °C and 70 °C, and is depicted in Figure VII.13. The response was linear in all cases, and it did not change significantly after coating. The reason behind the different response, when compared to the previous sensing head, is still not fully understood, and more experiments need to be performed. Nevertheless, sensitivities of 3.71 pm/°C (r^2=0.981), 3.86 pm/°C (r^2=0.956) and 3.27 pm/°C (r^2=0.9725), were obtained for the uncoated sensor, with one, and two coating layers, respectively.

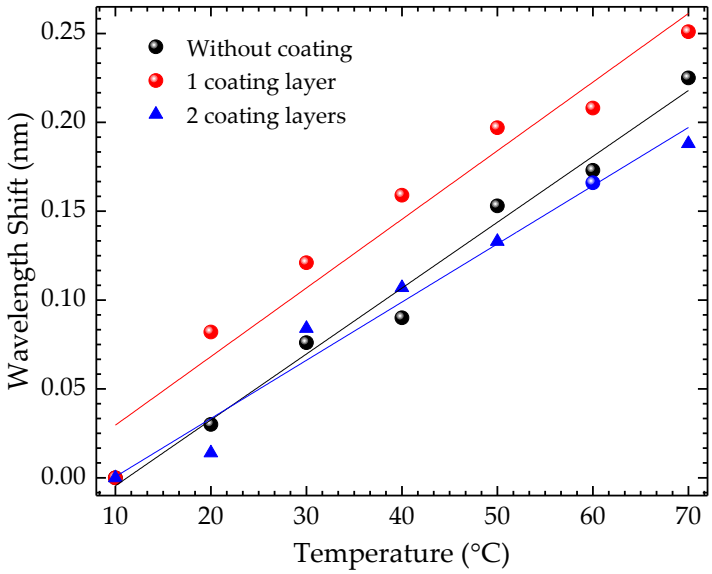

Figure VII.13. Response of the sensor with a different number of agarose gel layers to the temperature variations.

The stability of the sensor was also explored, under the same conditions as in the previous work, and the results are shown in Figure VII.14.

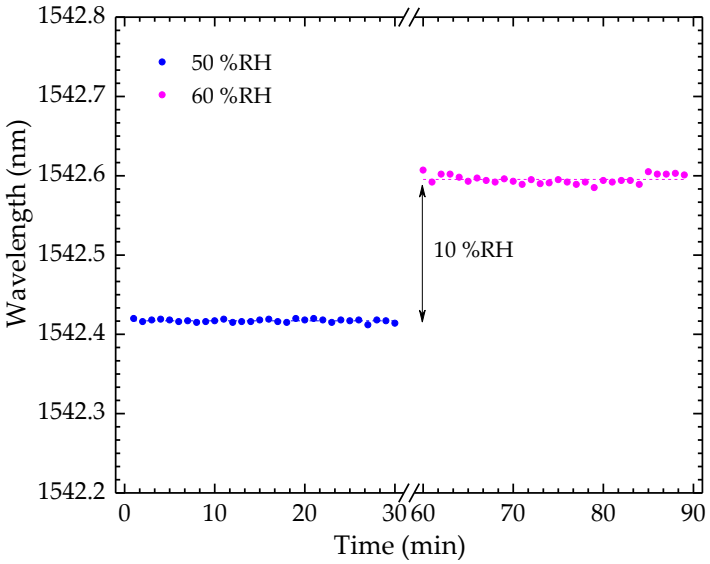

Figure VII.14. Step technique to estimate the resolution of the humidity sensor.

By applying the Eq. 3 of Chapter VII, a resolution of 6.06%RH is obtained, considering that the sensor is operating in whole RH region. More experiments with increasing number of layers need be done and further studies are still required to fully understand the influence of the number of layers in the spectra as well as in the sensors response.

References

38. Gao, R., Jiang, Y., Ding, W. *Agarose gel filled temperature insensitive photonic crystal fibers humidity sensor based on the tunable coupling ratio*, Sens. Actuators B, Chem., Volume 195, pp. 313-319, 2014, DOI: 10.1016/j.snb.2014.01.061.

VIII

Final remarks and future work

Final remarks and future work

The work developed in the context of this PhD programme had the aim of developing new optical fiber sensors for challenging media. This Thesis, structured in 8 Chapters, started by revising the general concepts that set the basis for the work carried out over the PhD programme, as well as a contextualization of the work developed, comparing the configurations here proposed with the ones found in the literature.

Considering an overall perspective, the work developed in this PhD was broadband, both on the number of sensing configurations and applications. New optical fiber sensors designs were explored in different contexts. Some were post-processed, either by producing microspheres with the aid of a fusion splicer, by developing new configurations by chemical etching or even by depositing specific materials in the sensing area.

Regarding the second Chapter, it should be highlighted that, typically, the monitoring of lithium ion batteries is done externally, by measuring current, voltage, temperature, and resistance. Taking into account the complex and harsh chemical environment of batteries, the optical fiber sensors, due to its characteristics seem to be the best option to be embedded between the separators. For this reason, in the context of the European Project SIRBATT the first work was developed. FBGs were successfully embedded in pouch cells and a comparison between the external and internal temperature variations was performed. From this work it can be concluded that the permanent and immediate control of the internal temperature was feasible with the FBG sensor technology presented, offering the possibility of safe operation of Li-ion batteries by early detection of heat generation. However, a better understanding of the temperature and pressure variations in Li-ion cells under heavy-duty cycling is key for the improvement of cell components as well as battery management systems. Therefore, to complement the work done in this Chapter, the long-term study of embedded sensors could be done, i.e. after constant charge, discharge cycles, for a long period (1 year or more). It would also be interesting to dismantle the pouch cells after that time and observe whether the fibers were damaged or if they were still in good operating conditions. Still in this context, new

optical fiber sensors should be developed to detect other internal parameters, to guarantee favorable operating conditions and to allow a stable electrolyte interface.

As part of the sensors presented in this Thesis were based on the Fabry-Perot (FP) interferometer, therefore it was essential to have an overview of what was published in the field. The state-of-the-art was done in the first Chapter, focusing in the configurations, the applications and the sensitivities obtained over the last four years. The FP configurations developed in the third Chapter were based on microcavities fabricated between a section of single mode fiber and multimode fiber. The results and the way of manufacturing the sensors were quite interesting, since only commercial fibers and a fusion splicer were needed. No liquids, oils or etching solutions were involved, emerging as an alternative to the previously developed air bubble sensors.

These sensors have the potential to be applied in other fields. For example, by using them as non-destructive testing technique, in structural monitoring and in the detection of defects in different materials. The monitoring of additive manufacturing based hybrid processes for long or continuous fiber reinforced polymeric matrix composites is of vital importance in many industries. In the case of embedding these sensors in polymeric matrix composites, different encasing geometry can be explored. By combining these sensing devices with other configurations, such as the FBGs, simultaneous measurement of different parameters can be achieved.

Furthermore, the geometry of the microspheres could still be improved in order to minimize losses and maximize the sensitivity. Using the same fabrication principles, these sensors could be fabricated at the tip of the fiber, and the sensor sensitivity to lateral loading could be further enhanced. The fabrication of the microsphere sensors with capillary tubes is other interesting matter of study. Different diameters of the hollow core fiber could give rise to different results, improving the sensitivity of the sensors.

The microcavities developed in fourth Chapter were fabricated by producing an air bubble near the end face of a multimode fiber section and by reshaping the tip in order to produce a thin silica diaphragm. This Chapter was focused on measurement water-glycerin mixtures. Taking these measurements into account, the sensor stability should be

evaluated by placing it in one solution, at a constant temperature, during a long period. The development of this sensor can be an added value, since this type of mixtures measurements are so important, for both for industry and medicine, since one of the most important parameters in the glycerin characterization process is the purity degree, especially when it is used in the pharmaceutical and cosmetic area. However this configuration has the possibility to expand to a wide variety of possible applications. For example, we could try to fabricate a micro-hole in the sensor tip using a focused ion beam, in order to develop a gas pressure sensor. In many industries, it is vital to monitor different gases, such as methane, carbon monoxide and dioxide, hydrogen, or even hydrogen sulfide. If, instead of a single micro-hole, the sensing structure had two micro-holes, the sensor could potentially be used for refractive index sensing, both of gases or liquids. These new configurations will be taken into account in future work.

The sensors developed in Chapters five, six, and seven are based on multimode interference for different applications. All these sensors are fabricated by splicing a short section of coreless silica fiber (CSF) to a standard single mode fiber and operate in reflection, which can represent a great advantage in practical applications. The influence on the CSF dimensions was the object of study in Chapter 5. The sensor was, in this case, applied for the measurement of refractive index variations in different glucose aqueous solutions. It was concluded that, although the CSF length does not play an important role in the sensor sensitivity, the reduction of diameter leads to a significant enhancement of the sensor response.

The sixth Chapter was focused in determination of the thermo-optic coefficient (TOC) of ethanol-water mixtures, through refractive index and temperature measurements using an etched CSF tip. The measurement of TOC has attracted a lot of attention, due to its importance in chemical and bio-chemical analysis. To my knowledge, this was the first time that this coefficient was determined for solutions with different concentrations of ethanol in water using a fiber sensor.

In Chapter seven, two relative humidity (RH) sensors were proposed and experimentally demonstrated. The first sensor also is based on multimode interference by

splicing a coreless fiber section to a single mode fiber, and by dip coating it with a hydrophilic agarose gel. A comparison between an uncoated and a coated sensor was made, and as expected, the uncoated sensor was insensitive to the environmental RH changes, whereas the sensor with agarose proved to be sensitive. As additional information, also presented in Chapter VII, a new moisture sensor based on a Fabry-Perot interferometer coated with agarose gel is proposed. These sensors have a great potential for real time RH monitoring, particularly in environments with high percentages of moisture, such as the lodges where Madeira wine is stored for ageing.

The sensors developed in the last three Chapters have attractive advantages, such as simple structure, fast response and stability. However, there is still a lot of work to be done with these types of sensors. For instance, in a future work, it could be interesting to compare different techniques to manufacture tapers with this kind of MMI structures. Tapered fibers can be manufactured using a splicing machine, a CO_2 laser or by chemical etching. As the fiber becomes thinner, the evanescent field becomes more exposed to the environment, enhancing the sensor response to external media. One can also transform these MMI structures to measure different parameters such as flow or magnetic fluids with adequate post-processing through chemical etching or focused ion beam.

In future developments it is also intended to address the challenge of detecting aroma compounds using purpose-designed optical fiber sensors. The detection of aroma compounds has been a subject of extensive study by the scientific community. The aroma can be constituted by a single chemical volatile organic compound (VOC) or by complex mixtures that, when present in air above a given concentration, can be detected by animals through the sense of olfaction [1]. The relevance of these compounds is undeniable in many industries, like food, beverages, and cosmetics. However, some VOCs can be extremely toxic for humans. Therefore, it is fundamental to detect the presence of VOCs with systems that present high sensitivity/resolution, fast response and are reliable [2]. The sensors here developed, together with new configurations based on evanescent field interaction will be further investigated for this application, particularly for the detection of specific aroma compounds that act as ageing markers in Madeira wine.

References

1. A. D. Wilson, M. Baietto, *Applications and advances in electronic-nose technologies*, Sensors, Vol. 9, pp. 5099-5148, 2009.

2. J. Tao, X. Wang, T. Sun, H. Cai, Y. Wang, T. Lin, D. Fu, L. L. Y. Ting, Y. Gu, D. Zhao, *Hybrid photonic cavity with metal-organic framework coatings for the ultra-sensitive detection of volatile organic compounds with high immunity to humidity*, Scientific Reports, Vol. 7, pp. 41640, 2017.